SNE SIMULATION NOTES EUROPE

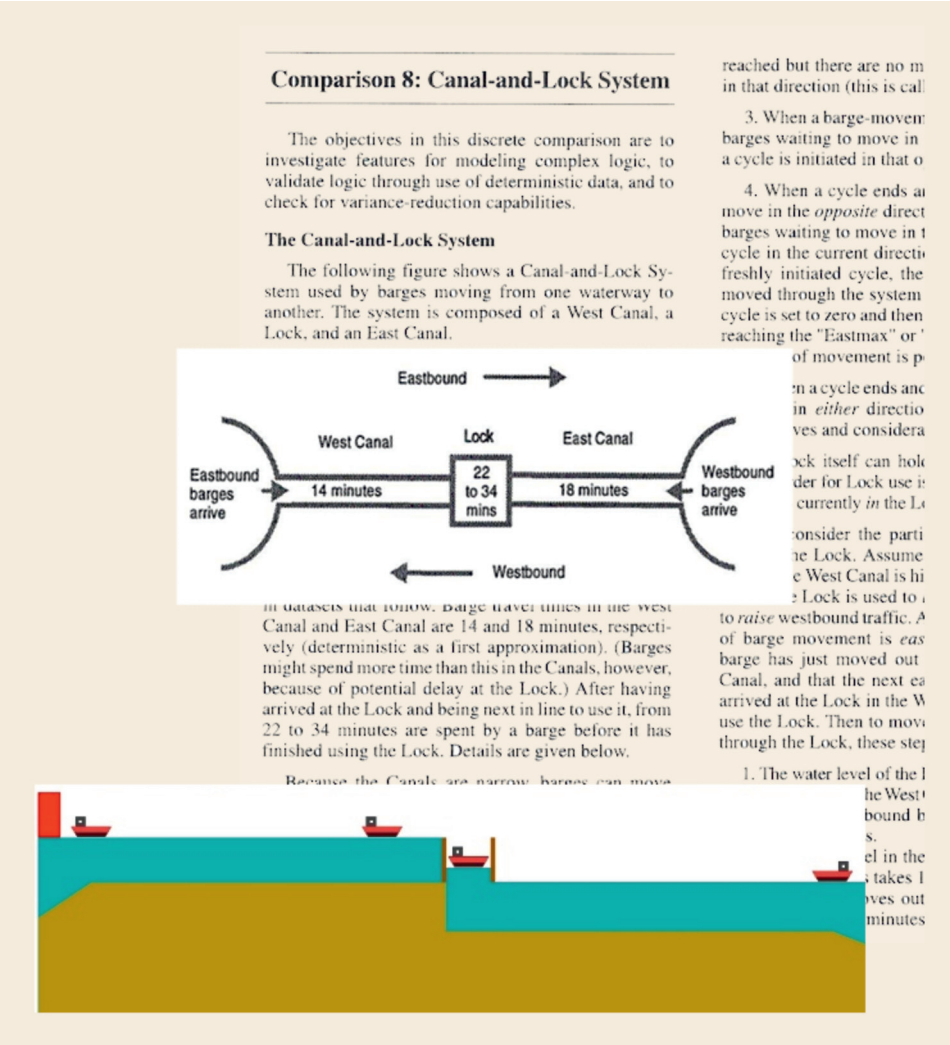

Comparison 8: Canal-and-Lock System

The objectives in this discrete comparison are to investigate features for modeling complex logic, to validate logic through use of deterministic data, and to check for variance-reduction capabilities.

The Canal-and-Lock System

The following figure shows a Canal-and-Lock System used by barges moving from one waterway to another. The system is composed of a West Canal, a Lock, and an East Canal.

Canal and East Canal are 14 and 18 minutes, respectively (deterministic as a first approximation). (Barges might spend more time than this in the Canals, however, because of potential delay at the Lock.) After having arrived at the Lock and being next in line to use it, from 22 to 34 minutes are spent by a barge before it has finished using the Lock. Details are given below.

Journal on Developments and Trends in Modelling and Simulation
EUROSIM Scientific Membership Journal
Vol. 35 No.3, September 2025 ISSN Online 2306-0271 DOI 10.11128/sne.35.3.1074

I3M 2025

International Multidisciplinary Modeling & Simulation Multiconference

September 17-19, 2025, Fes, Morocco
www.msc-les.org/i3m2025/

SIMS Scandinavian Simulation Society

SIMS 2025

September 23-24, 2025, Stavanger, Norway
www.scansims.org

Simulation in Produktion und Logistik 2025

September 24-26, 2025, Dresden, Germany
www.asim-gi.org/spl2025

Winter Simulation Conference 2025

December 7-10, 2025, Seattle, WA, USA
meetings.informs.org/wordpress/wsc2025/

EUROSIM Congress 2026

2026, Italy
date to be announced
www.eurosim.info

SIMS Scandinavian Simulation Society

SIMS 2026

September 16-17, 2026, Eskilstuna, Sweden
www.scansims.org

Editorial

***Dear Readers**, this third issue continues the post-conference publications from ASIM's Symposium Simulation Technique in Munich, September 2024, with improved English versions of the German version in the conference proceedings publications from ASIM's Symposium Simulation Technique in Munich, September 2024: J. Wittmann et al. discuss in a Short Note 'Will AI Make Simulation Superfluous ?' and report in a technical paper on 'Ultrafine Particles and the Occurrence of Heavy Rain: Model-Based Search for a Causal Relationship', and J. Stromberger et al. show the 'Implementation of a Smart Grid in an Operation -independent Simulation Model, and M. Göllner et al. present a (new) 'Methodology for the Identification of Systems with Non-linear Dynamic Behaviour'.*

But this issue also publishes two ARGESIM Benchmark solutions: P. G. Ioannou and V. Likhitruangsilp with a a STROBOSCOPE Solution to ARGESIM Benchmark C8 'Canal and Lock System', in full detail, with modelling and statistical evaluation, very suitable for educational purposes; and as result of a student simulation project at TU Wien a try for EXCEL as simulation tool for ARGESIM Benchmark C21'State Events and Structural Dynamic Systems', case study 'RLC with diode, again with modelling and implementation details, for educational purposes. We are happy to publish again solutions for the benchmarks, now in full detail with modelling and implementation. SNE supports this development of benchmark solutions from 1-page and 2-page contributions via Short Note– type solutions up to publication in length of Technical Notes.

I would like to thank all authors for their contributions, and many thanks to the SNE Editorial Office for layout, typesetting, preparations for printing, electronic publishing, and much more. And have a look at the info on EUROSIM-related simulation events: ASIM Conference on Simulation in Production and Logistics in Dresden, I3M 2025 conference in Fes, Morocco, WinterSim 2025 in Seattle, and further conferences and workshops of the EUROSIM societies.

Felix Breitenecker, SNE Editor-in-Chief, eic@sne-journal.org; felix.breitenecker@tuwien.ac.at

Contents SNE 35(3)

e-SNE 35(3), DOI 10.11128/sne.35.3.1074

www.sne-journal.org/sne-volumes/volume-35

SNE Basic e-Version with Open Access, CC BY 4.0

SNE Full e-Version for Members of publication-active EUROSIM Societies: ASIM, CEA-SMSG, CSSS, DBSS, KA-SIM, LIOPHANT, NSSM, PTSK, SIMS, SLOSIM, UKSIM

print-SNE for members on demand (printer INTU TU Wien)

SNE Contact & Info

SNE Online ISSN 2306-0271, SNE Print ISSN 2305-9974

→ *www.sne-journal.org*

office@sne-journal.org, eic@sne-journal.org

SNE Editorial Office
Felix Breitenecker (Organisation, Author Mentoring)
Irmgard Husinsky (Web, Electronic Publishing),
ARGESIM/Math. Modelling & Simulation Group,
Inst. of Analysis and Scientific Computing, TU Wien
Wiedner Hauptstrasse 8-10, 1040 Vienna, Austria

SNE SIMULATION NOTES EUROPE

WEB: → *www.sne-journal.org*, DOI prefix 10.11128/sne

Scope: Developments and trends in modelling and simulation in various areas and in application and theory; comparative studies and benchmarks (documentation of ARGESIM Benchmarks on modelling approaches and simulation implementations); modelling and simulation in and for education, simulation-based e-learning; society information and membership information for EUROSIM members (Federation of European Simulation Societies and Groups).

Editor-in-Chief: Felix Breitenecker, TU Wien, Math. Modelling Group
Felix.Breitenecker@tuwien.ac.at, eic@sne-journal.org

Print SNE: INTU (TU Wien), Wiedner Hauptstrasse 8-10, 1040, Vienna, Austria – *www.intu.at*

ARGESIM Publisher: ARBEITSGEMEINSCHAFT SIMULATION NEWS
c/o Math. Modelling and Simulation Group, TU Wien / 101, Wiedner Hauptstrasse 8-10, 1040 Vienna, Austria;
www.argesim.org, info@argesim.org on behalf of ASIM *www.asim-gi.org* and EUROSIM → *www.eurosim.info*

© 2025 SNE is licensed under CC BY 4.0 by ARGESIM Vienna - ASIM/GI - EUROSIM

SNE - Aims and Scope

Simulation Notes Europe (SNE) provides an international, high-quality forum for presentation of new ideas and approaches in simulation - from modelling to experiment analysis, from implementation to verification, from validation to identification, from numerics to visualisation (www.sne-journal.org).

SNE seeks to serve scientists, researchers, developers and users of the simulation process across a variety of theoretical and applied fields in pursuit of novel ideas in simulation. **SNE** follows the recent developments and trends of modelling and simulation in new and/or joining areas, as complex systems and big data. **SNE** puts special emphasis on the overall view in simulation, and on comparative investigations, as benchmarks and comparisons in methodology and application. For this purpose, **SNE** documents the **ARGESIM Benchmarks** on *Modelling Approaches and Simulation Implementations* with publication of definitions, solutions and discussions. **SNE** welcomes also contributions in education in/for/with simulation.

SNE is the scientific membership journal of **EUROSIM**, the *Federation of European Simulation Societies and Simulation Groups* (www.eurosim.info), also providing Postconference publication for events of the member societies. **SNE**, primarily an electronic journal **e-SNE** (ISSN 2306-0271), follows an open access strategy, with free download in basic version (B/W, low resolution graphics). Members of most **EUROSIM** societies are entitled to download **e-SNE** in an elaborate full version (colour, high resolution graphics), and to access additional sources of benchmark publications, model sources, etc. (via group login of the society), **print-SNE** (ISSN 2305-9974) is available for specific groups of **EUROSIM** societies.

SNE is published by **ARGESIM** (www.argesim.org) on mandate of **EUROSIM** and **ASIM** (www.asim-gi.org), the German simulation society. **SNE** is DOI indexed with prefix 10.11128.

Author's Info. Individual submissions of scientific papers are welcome, as well as post-conference publications of contributions from conferences of **EUROSIM** societies. **SNE** welcomes special issues, either dedicated to special areas and/or new developments, or on occasion of events as conferences and workshops with special emphasis.

Authors are invited to submit contributions which have not been published and have not being considered for publication elsewhere to the **SNE** Editorial Office.

SNE distinguishes different types of contributions (*Notes*), i.e.

- **TN** Technical Note, 6–10 p.
- **SN** Short Note, max. 5 p.
- **SW** Software Note , 4–6 p.
- **BN** Benchmark Note, 2–10 p.
- **ON** Overview Note – only upon invitation, up to 14 p.
- **EN** Education Note, 6–8 p.
- **PN** Project Note 6–8 p.
- **STN** Student Note, 4-6 p., on supervisor's recommendation
- **EBN** Educational Benchmark Note, 4–10 p.

Further info and templates (doc, tex) at **SNE**'s website, or from the Editor-in-Chief

www.sne-journal.org

office@sne-journal.org, *eic@sne-journal.org*

SNE Editorial Board

SNE - Simulation Notes Europe is advised and supervised by an international scientific editorial board. This board is taking care on peer reviewing of submission to SNE (and extended for special issues and Postconference publication):

Felix Breitenecker, *Felix.Breitenecker@tuwien.ac.at*
TU Wien, Math. Modelling, Austria, Editor-in-chief
David Al-Dabass, *david.al-dabass@ntu.ac.uk,*
Nottingham Trent University, UK
Maja Atanasijevic-Kunc*, maja.atanasijevic@fe.uni-lj.si*
Univ. of Ljubljana, Lab. Modelling & Control, Slovenia
Aleš Belič*, ales.belic@sandoz.com, Sandoz*
Peter Breedveld, *P.C.Breedveld@el.utwente.nl*
University of Twente, Netherlands
Agostino Bruzzone, *agostino@itim.unige.it*
Universita degli Studi di Genova, Italy
Vlatko Čerić, *vceric@efzg.hr*, Univ. Zagreb, Croatia
Russell Cheng, *rchc@maths.soton.ac.uk*
University of Southampton, UK
Roberto Cianci, *cianci@dime.unige.it*,
Math. Eng. and Simulation, Univ. Genova, Italy
Eric Dahlquist, *erik.dahlquist@mdh.se*, Mälardalen Univ., Sweden
Umut Durak, *umut.durak@dlr.de*
German Aerospace Center (DLR)Braunschweig , Germany
Horst Ecker, *Horst.Ecker@tuwien.ac.at*
TU Wien, Inst. f. Mechanics, Austria
Vadim Engelson, *vadime@mathcore.com*
MathCore Engineering, Linköping, Sweden
Peter Groumpos, *groumpos@ece.upatras.gr,* Univ. of Patras, Greece
Edmond Hajrizi, *ehajrizi@ubt-uni.net*
University for Business and Technology, Pristina, Kosovo
Glenn Jenkins, *GLJenkins@cardiffmet.ac.uk*
Cardiff Metropolitan Univ., UK
Emilio Jiménez, *emilio.jimenez@unirioja.es*
University of La Rioja, Spain
Peter Junglas, *peter@peter-junglas.de*
Univ. PHTW Vechta, Mechatronics, Germany
Esko Juuso, *esko.juuso@oulu.fi*
Univ. Oulu, Dept. Process/Environmental Eng., Finland
Kaj Juslin*, kaj.juslin@enbuscon.com*, Enbuscon Ltd, Finland
Andreas Körner, *andreas.koerner@tuwien.ac.at*
TU Wien, Math. E-Learning Dept., Vienna, Austria
Claudia Krull, *claudia@isg.cs.uni-magdeburg.de*, Institut für
Simulation und Graphik (ISG), Univ. Magdeburg, Germany
Francesco Longo, *f.longo@unical.it*
Univ. of Calabria, Mechanical Department, Italy
Yuri Merkuryev, *merkur@itl.rtu.lv,* Riga Technical Univ.
David Murray-Smith, *d.murray-smith@elec.gla.ac.uk*
University of Glasgow, Fac. Electrical Engineering, UK
Gasper Music, *gasper.music@fe.uni-lj.si*
Univ. of Ljubljana, Fac. Electrical Engineering, Slovenia
Thorsten Pawletta, *thorsten.pawletta@hs-wismar.de*
Univ. Wismar, Dept. Comp. Engineering, Wismar, Germany
Niki Popper, *niki.popper@dwh.at,* dwh Simulation Services, Austria
Kozeta Sevrani, *kozeta.sevrani@unitir.edu.al*
Univ. Tirana, Inst.f. Statistics, Albania
Yuri Senichenkov, *sneyb@dcn.infos.ru*
St. Petersburg Technical University, Russia
Michal Štepanovský, *stepami9@fit.cvut.cz*
Technical Univ. Prague, Czech Republic
Oliver Ullrich, *oliver.ullrich@iais.fraunhofer.de*
Fraunhofer IAIS, Germany
Siegfried Wassertheurer, *Siegfried.Wassertheurer@ait.ac.at*
AIT Austrian Inst. of Technology, Vienna, Austria
Sigrid Wenzel, *S.Wenzel@uni-kassel.de*
Univ. Kassel, Inst. f. Production Technique, Germany
Grégory Zacharewicz, *gregory.zacharewicz@mines-ales.fr*
IMT École des Mines d'Alès, France

STROBOSCOPE Solution to ARGESIM Benchmark C8 'Canal and Lock System'

Photios G. Ioannou[1*], Veerasak Likhitruangsilp[2]

[1]Dept. of Civil and Environmental Engineering, University of Michigan, Ann Arbor, MI, USA, *photios@umich.edu
[2]Center of Digital Asset Management for Sustainable Development (CDAM), Dept of Civil Engineering, Faculty of Engineering, Chulalongkorn University, Bangkok, Thailand

SNE 35(3), 2025, 125-132, DOI: 10.11128/sne.35.bn08.10741
Submitted: 2025-06-23
Received Improved: 2025-07-28; Accepted: 2025-08-01
SNE - Simulation Notes Europe, ARGESIM Publisher Vienna
ISSN Print 2305-9974, Online 2306-0271, www.sne-journal.org

Abstract. A STROBOSCOPE simulation model for a canal and lock system illustrates how to model barge traffic logic to estimate the average pooled barge transit time. Investigated are the impact of traffic density and of the number of barges allowed to pass in each cycle. Antithetic sampling and common random numbers illustrate variance reduction techniques.

Introduction

A canal and lock system is described in ARGESIM Comparison C8 [1]. A model of this system was developed in STROBOSCOPE [2], a general-purpose discrete event simulation system, as an example of modelling complex logic. A PROOF Animation model provided verification. Parametric analysis involving the traffic density of arriving barges and the controls for switching traffic direction provides additional insights into system behaviour.

1 Canal and Lock System

A canal and lock system consists of the west canal, the east canal, and the lock, as shown in Figure 1. Water level in the west canal is higher than in the east canal. The times between barge arrivals at the east and west canal entrances are exponential with mean β. The impact of traffic density as measured by β on the average barge transit time is investigated through sensitivity analysis.

A barge can go through the west canal in 14 minutes and the east canal in 18 minutes. The time to pass through the lock itself can be anywhere from 22 to 34 minutes. Thus, the total transit time can be from 54 to 66 minutes.

Safety considerations permit only one direction of traffic and only one barge in each canal at the same time. The direction of traffic alternates in cycles between eastbound and westbound barges. Within each cycle, barges enter the system on a first-come, first-served basis.

1.1 Traffic direction

The direction of barge traffic changes in cycles that can be full or partial. A full cycle ends when the number of eastbound barges reaches the limit *Emx* or the limit *Wmx* for westbound barges.

A partial cycle ends when there are not enough barges traveling in the same direction to reach *Emx* or *Wmx*, but there are barges waiting to cross in the opposite direction. In such cases, the following traffic rules apply:

1. If at the end of a cycle, no barges are waiting to cross in either direction, the system remains idle until a barge arrives and starts a new cycle in its direction.
2. If at the end of a full cycle, there are barges queued in the opposite direction, then a new cycle is initiated in the other direction.

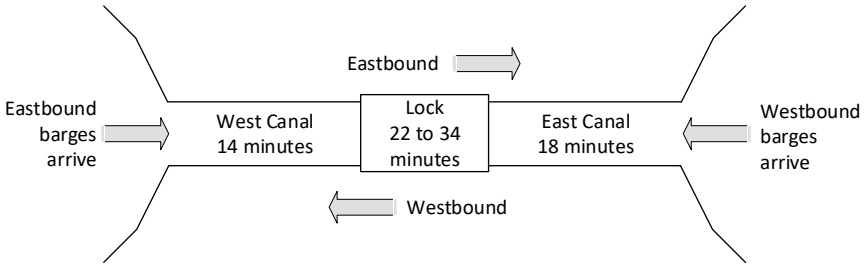

Figure 1: Canal and Lock System Layout.

3. If no barges are queued in the opposite direction, but there are barges waiting to cross in the current direction, then a new cycle is initiated in the current direction. The barge count for the new cycle is reset to zero and can reach the corresponding limit *Emx* or *Wmx*.

1.2 Lock operations and times

The lock can lower one eastbound barge and raise one westbound barge at a time. Lock operations and times during an eastbound cycle are as follows (lock operations and times for a westbound cycle are the same).

- **Case A**: Lock passage time = 34 min (= maximum).
  Setting: An eastbound barge has just exited the lock into the east canal and another eastbound barge is already waiting at the lock entrance.
  1. Water in lock raised to west canal level, 12 min.
  2. Waiting barge enters lock, 5 min.
  3. Barge lowered to east canal level, 12 min.
  4. Barge exits into the east canal, 5 min.

  Total time = 12+5+12+5 = 34 min.
- **Case B**: Lock passage time = 22 min (= minimum).
  Setting: The next eastbound barge arrives at the lock 12 or more minutes after the previous barge has exited. Only steps 2–4 are needed.
  Total time = 5+12+5 = 22 min.
- **Case C**: Lock passage time = from 22 to 34 min.
  Setting: The next eastbound barge arrives *t* minutes after the lock has started refilling ($0 < t < 12$ min).
  Total time = (12-*t*) min (wait time to refill lock) + 22 min (steps 2–4) = (34-*t*) min.

2 Simulation Model

The network for the STROBOSCOPE simulation model of the canal and lock system is shown in Figure 2. The blue nodes (queues and activities) model the movement of eastbound barges. The green nodes model the symmetrical movement of westbound barges.

Three types of resources are defined: *Sequence, Lock*, and *Barge*. Queues *EBSeq*, *WBSeq*, *Set2EBSeq*, and *Set2WBSeq* are initialized with 1 unit of the generic resource *Sequence* to start loops that create serial instances of the succeeding combi activities. Queue *LockWithRsdWL* is initialized with 1 unit of the compound type *LockSystem* to start the loop of activities *LowerWL* and *RaiseWL* that change the lock water level when no barge is in the lock.

Barges are modelled as characterized resources of type *Barge* with two subtypes, *EBBarge* and *WBBarge*. Barges are generated dynamically while the simulation runs. The current direction of travel is stored in savevalue *Direction*, whose values can be *EB* or *WB*.

The time between eastbound arrivals is modelled by combi activity *EBBargesArrive* whose duration is exponential with mean *β*. When each instance of *EBBargesArrive* ends, a new arriving *EBBarge* is created dynamically by a *GENERATE* statement. The arriving *EBBarge* then enters queue *EBBWait2Enter*, where it waits until the semaphore of activity *EBBEnterSystem* allows it to start.

```
SEMAPHORE EBBEnterSystem 'Direction==EB
  & EBBCount<Emx & !EBBTraverseWC.CurInst
  & !EBWt2EntrLock.CurCount';
BEFOREEND EBBEnterSystem ASSIGN
       EBBCount EBBCount+1;
```

The above semaphore allows *EBBEnterSystem* to start and draw *EBBarge* out of queue *EBBWait2Enter* when

(a) savevalue *Direction* equals *EB*,
(b) the count of eastbound barges allowed to cross in the current cycle is less than *Emx*,
(c) there are no current instances of *EBBTraverseWC* (i.e., the west canal does not contain another eastbound barge), and
(d) there are no barges in queue *EBWt2EntrLock* waiting to enter the lock.

Activity *EBBEnterSystem* has a duration of zero. Before it ends it increments by one the count of eastbound barges *EBBCount* that have crossed in the current cycle. It then releases *EBBarge* to activity *EBBTraverseWC*, where it spends 14 minutes to traverse the west canal. *EBBarge* then enters queue *EBWt2EntrLock* where it waits for the water in the lock to be fully raised (i.e., for queue *LockWithRsdWL* not to be empty) so it can enter the lock. Activity *EBBEnterLock* can then start, draw *EBBarge* and *LockSystem* from the preceding queues, and keep them for the 5 minutes to enter the lock. At its end, both resources are released to activity *LowerWaterLevel* where they remain for 12 minutes for the lock to lower the barge to the east canal. Activity *EBBExitLock* is the 5 minutes it takes for the barge to exit the lock.

At that point, *LockSystem* is released to queue *LockWithLwdWL* and *EBBarge* is released to an instance of activity *EBBTraverseEC* for the 18 minutes needed to traverse the east canal. At the end of *EBBTraverseEC*, the resource *EBBarge* is destroyed, and statistics are kept about its life span, which equals its total transit time.

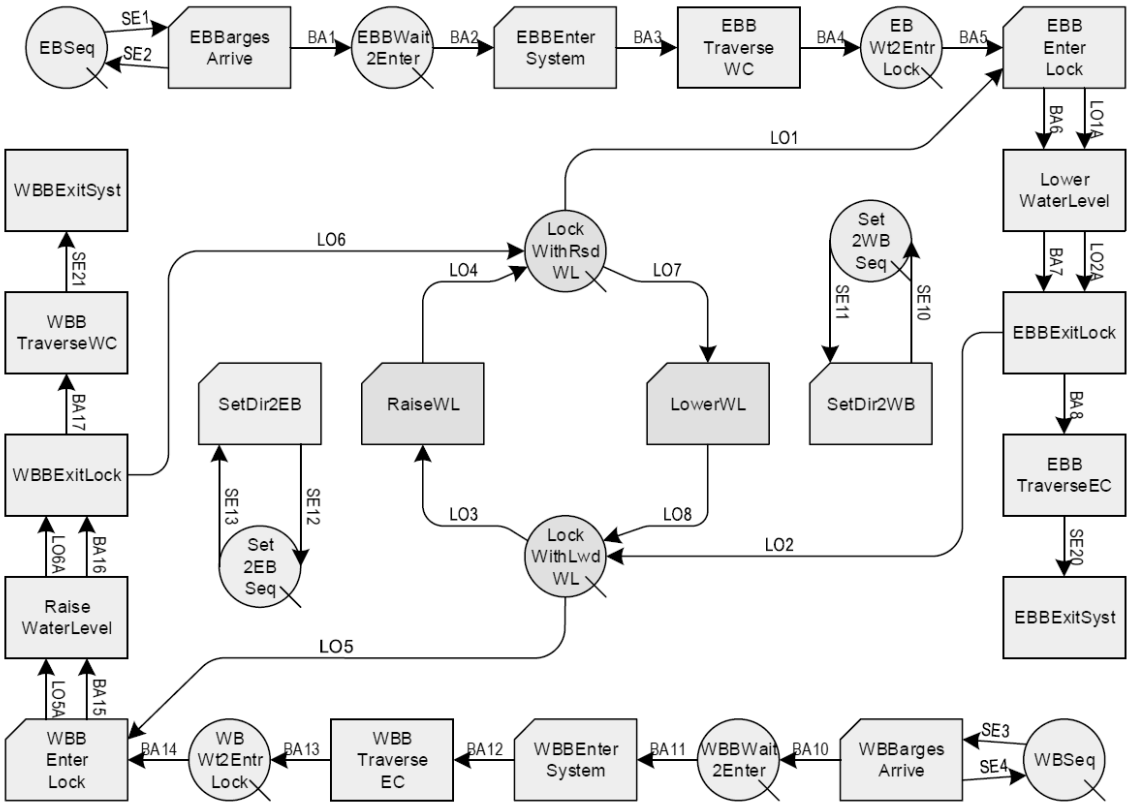

Figure 2: STROBOSCOPE Simulation Network.

The green-shaded queues and activities for the westbound barges are similar to the blue-shaded nodes.

The red activities *RaiseWL* and *LowerWL* model the 12 min to raise or lower the water level in the lock when it does not contain a barge. They start when their semaphores allow as follows.

```
SEMAPHORE RaiseWL 'EBBTraverseWC.CurInst
                | EBWt2EntrLock.CurCount';
SEMAPHORE LowerWL 'WBBTraverseEC.CurInst
                | WBWt2EntrLock.CurCount';
```

The semaphore for combi activity *RaiseWL* allows the activity to start when an *EBBarge* is approaching through the west canal (i.e., when there is a current instance of activity *EBBTraverseWC*), or when an *EBBarge* is waiting at the lock for the water to rise (i.e., when queue *EBWt2EntrLock* is not empty). The semaphore for combi activity *LowerWL* is similar.

From the perspective of traffic logic, the key activities are *SetDir2EB* and *SetDir2WB* — they set the direction of barge traffic to *EB* or to *WB* and reset to zero the count of barges that traversed in a cycle.

Both activities have a duration of zero and are preceded by queues that are initialized with 1 unit of *Sequence*. Thus, these two activities are in constant readiness to start and perform actions whenever their semaphores allow. As an example, the following statements illustrate the semaphore logic and actions for combi activity *SetDir2WB*.

```
SEMAPHORE SetDir2WB
'(EBBExitSyst.TotInst==EBBEnterSystem.TotInst)
& ((EBBCount==Emx) |
   (Direction==EB & !EBBWait2Enter.CurCount
                  & WBBWait2Enter.CurCount))';
ONEND SetDir2WB ASSIGN EBBCount 0;
ONEND SetDir2WB ASSIGN Direction WB;
```

The above semaphore allows activity *SetDir2WB* to start under one of two logical conditions that correspond to the end of a full cycle or the end of a partial cycle.

- Both cycles require that all eastbound barges that have entered have also exited the system (red code).
- A full cycle ends when, in addition, the number of eastbound barges has reached *Emx* (green code).

- A partial cycle ends when, in addition, (a) the current *Direction* is *EB*, (b) there are no eastbound barges waiting to enter, and (c) there are westbound barges waiting to enter (blue code).

Whenever one of the above conditions is satisfied, combi activity *SetDir2WB* starts and ends immediately. Before it ends, it performs the following two important actions:

- It resets the barge count *EBBCount* to zero .
- It sets *Direction* to *WB*.

The semaphore and actions for combi activity *SetDir2EB* are similar.

It should be noted that at the end of a full eastbound cycle, activity *SetDir2WB* may switch *Direction* to *WB* only for an instant.

If at that point there are no westbound barges ready to cross, but there are more eastbound barges waiting, then activity *SetDir2EB* will immediately complete a partial cycle and start a new eastbound cycle by setting *Direction* to *EB*. Thus, activities *SetDir2WB* and *SetDir2EB* may start and reset *Direction* at the same simulation time, as needed.

2.1 Model validation

The initial validation of the model was done by using the deterministic datasets described in [1] and produced the required results.

2.2 PROOF Animation

A PROOF Animation model driven by STROBOSCOPE was also developed as an effective way to verify the simulation model logic.

Figure 3 is a snapshot of the animation and shows static data — such as *Emx*=5, *Wmx*=5, and the mean time between barge arrivals, β=75 min—as well as dynamic data—such as *SimTime*=66.7 hrs, the current values of *Te*=292.66 min and *Tw*=216.04 min, the number of barges processed in each cycle (*En*=4, *Wn*=5), and the number of barges waiting to enter the west and the east canals (*Eq*=3, *Wq*=9). The snapshot also shows the lock while lowering an eastbound barge, another eastbound barge currently waiting to enter the lock, three more eastbound barges waiting in line to enter the west canal (red column), and nine westbound barges waiting in line to enter the east canal (blue column).

3 Sensitivity Analysis

The STROBOSCOPE simulation model produces three basic performance metrics as output:

- *Te* = Average Eastbound Barge Transit Time.
- *Tw* = Average Westbound Barge Transit Time.
- *Tp* = Average Pooled Barge Transit Time for all barges irrespective of direction of travel.

Of these, the average pooled barge transit time *Tp* is the most indicative measure of overall system performance and is discussed in the following sections.

The model also includes control statements for performing sensitivity analysis and comparing alternatives:

- The traffic control parameters *Emx* and *Wmx* can vary over a range of values (e.g., 1 to 50).
- The mean time between barge arrivals, β, can also vary over a range (e.g., 70 to 85 min).

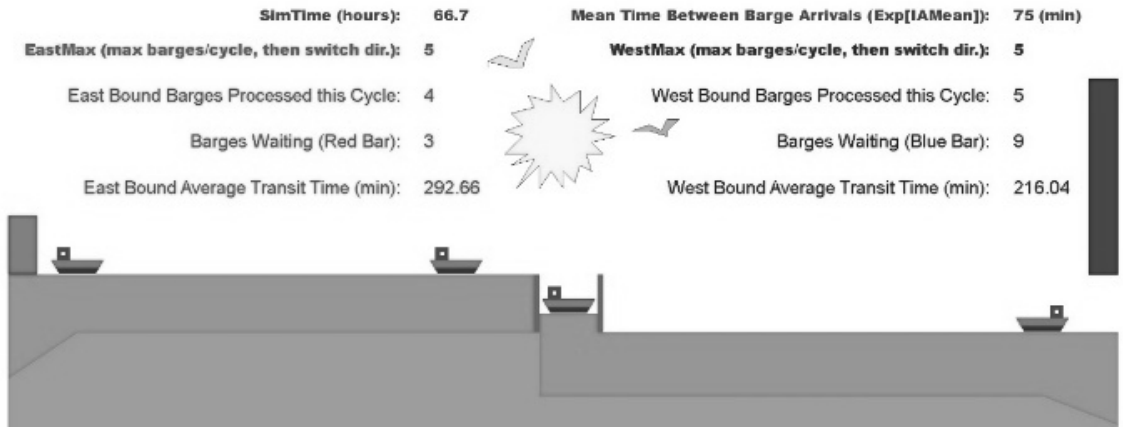

Figure 3: Animation Screen Shot, *Emx* = 5, *Wmx* = 5, and β = 75 min.

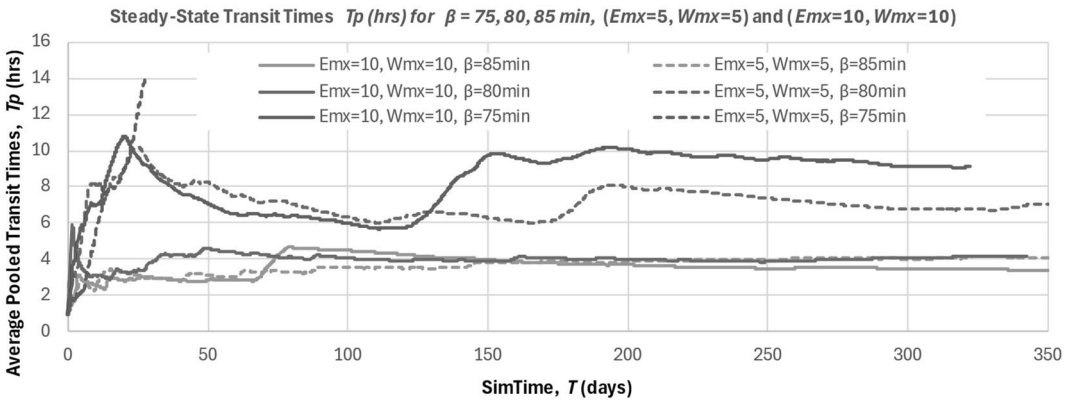

Figure 4: Steady-State Avg Pooled Transit Times, *Tp* (hrs).

- Multiple replications can be performed for all sets of values of the above parameters *Emx*, *Wmx*, and β, to increase output statistical accuracy (e.g., 100 reps).

Figure 4 shows the average pooled barge transit times *Tp* for (*Emx*=5, *Wmx*=5), (*Emx*=10, *Wmx*=10), and mean values β = 75, 80, 85 min. As shown, when the system is simulated for *T* = 1 year, most transit time curves *Tp* go through a transient phase and then approach steady-state values. Only the dashed red *Tp* curve for *Emx*=5, *Wmx*=5, and β=75 min (which unfortunately are the values suggested in [1]) continues to rise to infinity, indicating that the limits *Emx*=5 and *Wmx*=5 are too small for the large traffic volume caused by β=75 min. (This is also observed in [3], which switched to β=85 min as a better mean value.)

For the same mean β=75 min, the solid red *Tp* curve for the larger values *Emx*=10 and *Wmx*=10 does approach steady state values close to 9-10 hours. This shows that larger (but balanced) values of *Emx* and *Wmx* decrease the average pooled transit times *Tp*.

Figure 4 also shows that as β increases from 75 to 80 to 85 minutes, demand for the use of the lock decreases, and consequently, the average pooled transit times *Tp* also decrease from about 9 hrs to about 3 hrs.

Figure 5 shows the steady state (*T*=1 yr) average pooled barge transit times *Tp* over 10 replications, for β=85 min and for *Emx* and *Wmx* values from 3 to 10. Clearly, the average pooled transit times *Tp* decrease to about 3 hours as both limits *Emx* and *Wmx* increase to 10. Simulations for even larger values of *Emx* and *Wmx* (as high as 50) show that average transit times *Tp* continue to decrease asymptotically (but only by a little) to 2.8 hours.

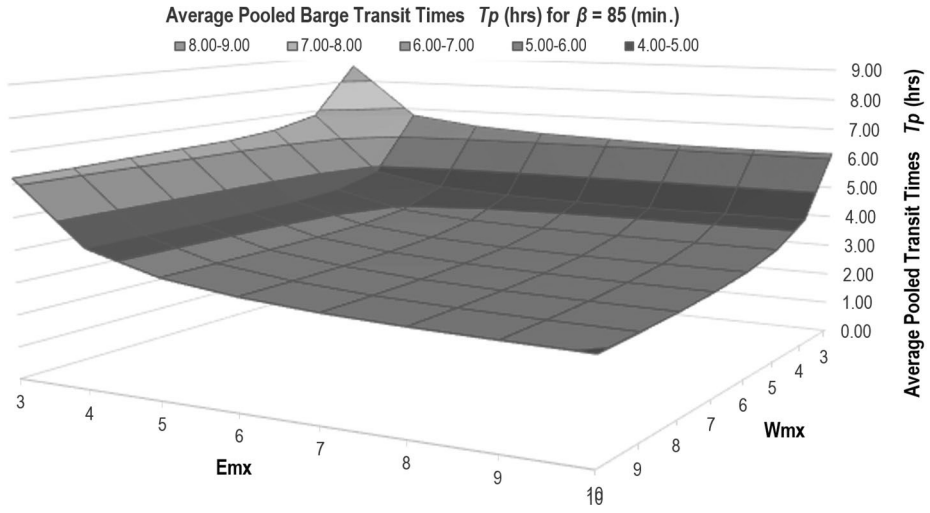

Figure 5: Average Pooled Transit Times *Tp* (hrs) vs. *Emx* and *Wmx* for β = 85 min.

4 Variance Reduction

4.1 Antithetic Random Variates (ARV)

An investigation of variance reduction using antithetic variates for the estimation of 90% confidence intervals for the average pooled transit times *Tp* (min) was conducted for the values suggested in [1], *Emx*=5, *Wmx*=5, *β*=75 min, and *T*=10 days (14400 min). The results are shown in Table 1 and are very close to those in [4].

		100 Independent Replications		50 Replications using Antithetic Variates	
Run	**Avg Tp**	**90% CI**	**σ**	**90% CI**	**σ**
1	494.9	37.7	227.10	25.8	108.91
2	520.0	37.1	223.46	24.7	104.23
3	489.5	41.2	247.87	25.2	106.32

Table 1: Antithetic variates-Average pooled transit times *Tp* (min), *Emx*=5, *Wmx*=5, *β*=75 min, T=10 days.

A total of 100 replications were divided into two groups, 50 using independent samples and 50 using the corresponding antithetic variates. The sample for the independent statistics used all 100 average pooled transit time *Tp* values. For antithetic sampling, each pair of *Tp* values (standard and its antithetic) was added and divided by two to give a sample of 50 averages.

Table 1 shows the independent and antithetic statistics for the average pooled transit times *Tp* (min) from three separate runs for comparison.

Clearly, antithetic random variates are an effective variance reduction technique and reduce the half-width of the confidence intervals and the standard deviation σ significantly in all three runs.

4.2 Common Random Numbers (CRN)

Variance reduction using common random numbers was used to compare the pooled transit times *Tp* between two alternative policies: policy *Mx*5 = (*Emx*=5, *Wmx*=5) and *Mx*6 = (*Emx*=6, *Wmx*=6). The null hypothesis was that "*Tp*5 is less than *Tp*6" (i.e., that the *Tp* for *Mx*5 is less than the *Tp* for *Mx*6).

Table 2 shows the results from 50 replications for *β*=75 min and *T*=10 days (14400 min). For comparison, three separate runs are shown. The confidence intervals for the difference *Tp*5-*Tp*6 from *independent* simulations contain negative values, and thus the null hypothesis cannot be rejected. When using CRN, however, the confidence intervals for the difference *Tp*5-*Tp*6 contain only positive values and thus the null hypothesis can be rejected at the 10% level of significance.

	Average	**Ind: *Tp*5-*Tp*6**		**CRN: *Tp*5-*Tp*6**	
Run	***Tp*5-*Tp*6**	**90%CI**	**σ**	**90%CI**	**σ**
1	57.3	79.1	333.6	9.0	37.9
2	69.8	78.2	330.0	8.2	34.6
3	59.6	63.6	268.4	7.5	31.6

Table 2: CRN- *Tp*5-*Tp*6 (min) for *Mx*5=(*Emx*=5,*Wmx*=5) vs. *Mx*6=(*Emx*=6,*Wmx*=6), for *β*=75 min, *T*=10 days

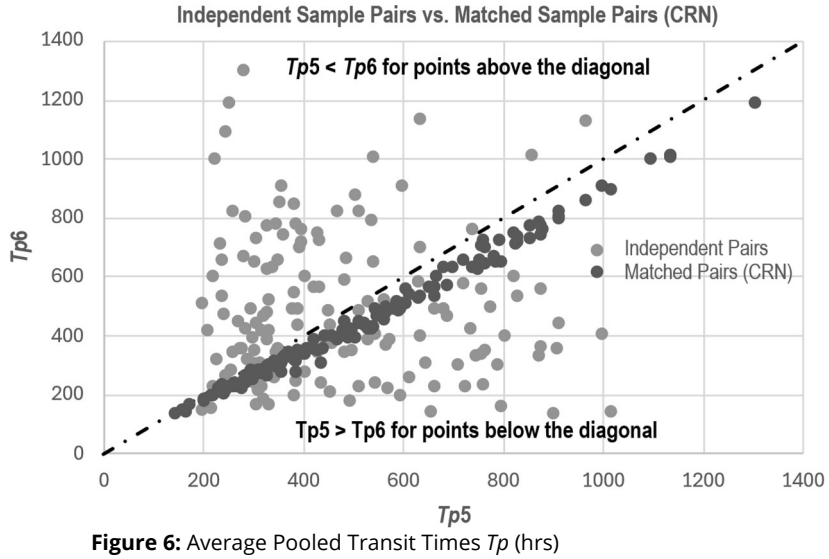

Figure 6: Average Pooled Transit Times *Tp* (hrs) vs *β* for (*Emx*=5, *Wmx*=5) vs. (*Emx*=6, *Wmx*=6).

The 150 pairs of values (*Tp5*, *Tp6*) from successive independent and matched pairs (CRN) for all three runs are shown in Figure 6. The 150 orange pairs of independent values (*Tp5*, *Tp6*) are scattered and cannot be used to discern whether "*Tp5* is less than *Tp6*" or vice versa.

In contrast, the 150 blue matched pairs (*Tp5*, *Tp6*) produced by CRN lie below the diagonal and show a strong positive correlation. This indicates clearly that the null hypothesis that "*Tp5* is less than *Tp6*" can safely be rejected. For the same stream of barge arrivals, the operating policy *Mx*6 produces shorter and thus better average pooled barge transit times *Tp6*<*Tp5* and should be preferred.

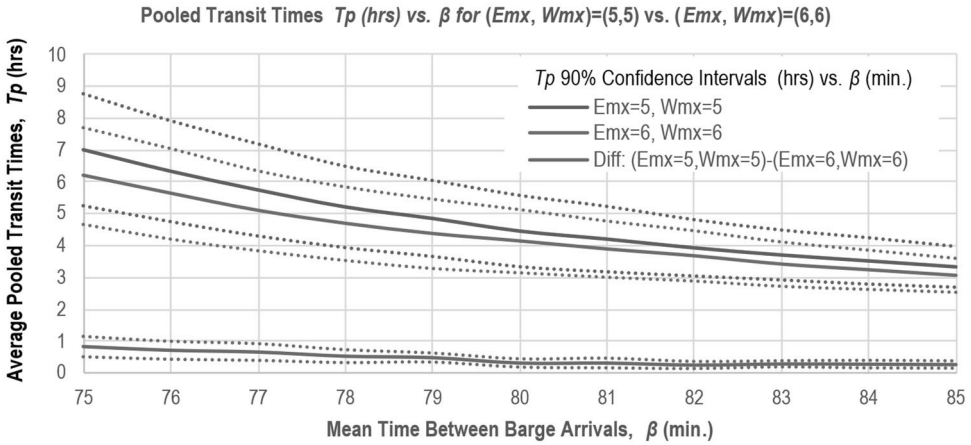

Figure 7: Average Pooled Transit Times *Tp* (hrs) vs β for (*Emx*=5, *Wmx*=5) vs. (*Emx*=6, *Wmx*=6).

Figure 7 shows a comparison of *Tp*5 vs *Tp*6 for values of the mean barge interarrival time β from 75 to 85 min. The solid red curve shows the average *Tp*5 from 10 replications and the dotted red curves show the 90% confidence intervals around the average for the true mean barge transit time for *Mx*5. The solid and dotted green curves are similar but for *Tp*6 and *Mx*6.

For each value of β, 10 replications were performed using CRN (i.e., the same stream of random barge arrivals) to produce one matched pair (*Tp*5, *Tp*6). These 10 pairs were then averaged to produce the red and green pairs (*Tp*5, *Tp*6) for that value of β. However, because the number of replications, 10, is small, the 90% confidence intervals for *Tp*5 and *Tp*6 shown in Figure 7 overlap, and thus it is not possible to discern whether the mean *Tp*5 is strictly greater and thus worse than the mean *Tp*6. To make this determination, each of the 10 replications also calculated one sample for the difference *Tp*5-*Tp*6 from the matched pair (*Tp*5, *Tp*6) for that value of β. These 10 samples of the difference *Tp*5-*Tp*6 gave the average and the 90% confidence intervals for the difference *Tp*5-*Tp*6, shown by the solid and dotted blue curves.

The important point is that the blue curve values for *Tp*5-*Tp*6 are due mainly to differences in performance between policy *Mx*5 and *Mx*6 and are not due to chance. The blue curves for the 90% confidence intervals for *Tp*5-*Tp*6 in Figure 7 are positive for all β. Thus, the null hypothesis that the mean *Tp*5 is less than the mean *Tp*6 can be rejected at the 10% level of significance for all values of the mean interarrival time β. As a result, policy *Mx*6 results in shorter average transit times than *Mx*5 for all β.

The remarkable reductions in the width of the 90% confidence intervals and the standard deviation σ shown in Table 2 and Figure 7 illustrate the effectiveness of matched pairs and common random numbers as a variance reduction technique for the comparison of alternative policies.

5 Comments

The canal and lock system is an interesting transportation problem that is similar to an earthmoving project for the construction of a dam in California that used heavy trucks to haul fill material [5]. In that project, most of the rural road from the borrow area to the dam could handle two-way traffic (similar to the east and west waterways) except for a narrow segment at the side of a cliff, which could accommodate only one-way traffic (similar to the canal and lock system). The narrow segment was divided into two parts of about the same length (similar to the east and west canals) by a temporary bridge (similar to the lock) that could support only one heavy truck at a time.

A STROBOSCOPE simulation model for this earthmoving project for the construction of a dam used engineering calculations to determine the optimum mix of trucks, to evaluate traffic policies, and to investigate the construction of two bridges to streamline traffic to save time [5].

As also noted in [3], the original assumptions of a mean time of β=75 min for the exponentially distributed barge interarrival times, together with the limits of *Emx*=5 and *Wmx*=5 barges, result in queues at the canal entrances that grow to infinity. A better choice would have been β=85 min as was assumed in [3].

The complete data for Figure 5 for a long simulation run, T=1 year, that reaches steady state, show that the average pooled barge transit times Tp for a system with a mean time of β=85 min continue to decrease as the values of Emx and Wmx increase from 1 to 50. Values of Emx=Wmx=14 give Tp=173 min. Values as high as Emx=Wmx=50 continue to decrease Tp, but only by a little to 169.3 min.

The corresponding figure for β=75 min and values of Emx and Wmx from 1 to 50 is similar in shape to Figure 5 but has higher Tp values. For a simulation run T=10 days, the minimum value is Tp=255 min, while for T=1 year, the minimum value is Tp=317 min. Both occur at large values of Emx and $Wmx \geq 40$.

The fact that higher values for Emx and Wmx result in lower average pooled barge transit times Tp indicates that the best traffic policy for the canal and lock system might be to abolish the Emx and Wmx limits and allow all queued barges that travel in the same direction to cross without an upper limit. The direction of traffic would then switch whenever there are no more barges that travel in the current direction (i.e., similar to the end of a partial cycle with infinite limits). For β=85 min, this would give a minimum average pooled transit time of $Tp \approx 169.3$ min.

The canal and lock system described in [1] (with minor changes) is well suited to education and the teaching of simulation. The authors have used it as an assignment in a graduate course on simulation with success.

STROBOSCOPE [2] (an acronym for State and Resource-Based Simulation of Construction Processes) is a general-purpose discrete-event simulation system and language co-developed by the first author. Its simulation models use a graphical network-based representation similar to activity cycle diagrams. Its design is based on three-phase activity scanning that can model the complex resource interactions that characterize cyclic operations without the need to make a distinction between the resources that serve (servers or scarce resources) and those served (customers or moving entities). The late Thomas J. Schriber [1] was a member of the doctoral committee that oversaw the development of STROBOSCOPE.

References

[1] Schriber TJ. Comparison 8: Canal-and-Lock System. *SNE*. 1996; 6(1): 29-31.

[2] STROBOSCOPE Simulation System Software. Retrieved from www.stroboscope.org. March 17, 2025.

[3] Schmidt B, Toussaint A. Comparison 8- Simplex II. *SNE*. 1997; 07(20), 28-29.

[4] Brunmeir D, Rößler M. A SimEvents/Simulink-based Solution to ARGESIM Benchmark C8 'Canal and Lock System'. *SNE*. 2015; 25(1), 55-58.

[5] Ioannou PG. Simulation of Earthmoving for a Dam using Engineering Calculations. In Corlu CG, Hunter SR, Lam H, Onggo BS, Shortle J, Biller B, editors. Proceedings, 2023 Winter Simulation Conference. *WSC '23.* 2023 Dec; San Antonio, Texas, Piscataway, New Jersey: IEEE. 2756–2767.
DOI 10.1109/WSC60868.2023.10407315

Will AI Make Simulation Superfluous? - A Subjective Stocktaking –

Jochen Wittmann[1*], Thomas Clemen[2]

[1]Univ. of Applied Sciences HTW Berlin, Environmental Informatics, Wilhelminenhofstraße 75A, 12459 Berlin, Germany; **jochen.wittmann@HTW-Berlin.de*

[2]Univ. of Applied Sciences Hamburg, Berliner Tor 7, 20099 Hamburg

SNE 35(3), 2025, 133-136, DOI: 10.11128/sne.35.sn.10742
Selected ASIM SST 2024 Postconf. Publication: 2024-12-10
Rec. Impr. English version: 2025-06-27; Accepted: 2025-07-15
SNE - Simulation Notes Europe, ARGESIM Publisher Vienna
ISSN Print 2305-9974, Online 2306-0271, www.sne-journal.org

Abstract. Based on current success stories using AI methods, this paper examines the relationship between the problem-solving methods AI and system simulation. An analysis of the process steps of the two approaches highlights the fundamental difference between the black-box approach of learning methods and the glass-box approach of structure-explaining simulation models. The mutual benefits of the two approaches can then be explained using four use cases. A further result of the analysis is the question of the extent to which simulation and AI methods can lead to the same or different results. To this end, the concept for a structural analysis is presented, which is based on the idea of analysing the intersection between the results of AI and the simulation method.

AI in Competition with Classic Simulation Methods ?

Forecasts on the development of demand and the content of engineering professions show, on the one hand, that human intelligence will probably continue to be irreplaceable, especially for creative tasks, but on the other hand, around 50 per cent of working time could be replaced or at least significantly supported by artificial intelligence methods. ([1],[2],[3],[4]).

These forecasts will be analysed in more detail here with regard to the method of dynamic system simulation. In this area, too, there are initial approaches to generating simulation models automatically or at least with AI support, although the limits of AI are still evident at present [5].

On the other hand, there are many examples of applications in which the use of AI and classic simulation have been successfully combined. We will look at these examples in detail in the section on possible use cases.

However, in order to be able to work out the mutual advantages, we will first compare the way the simulation method works with the general approach of data-driven machine learning (ML) (as a sub-area of AI). The potential efficiency gains of combining the methods will then be presented in more detail. Following these fields of application of coupling and/or combining AI and simulation, which are already established in practice, an approach will be presented at the end that uses experiments on a structural, set-theoretical basis to determine whether the two approaches actually (only) produce the same results or whether they (can) find qualitatively different solutions.

1 Analysing the Process Steps oft the Isolated Methods

1.1 Simulation Method

The aim of using the simulation method is always to develop a model in a formalism that enables the algorithmic processing of time progress within the scope of a simulation run. The trajectories of the model variables over time derived from the model description allow statements to be made about the modelled system within the previously agreed validity range of the model. The decisive step in this procedure is the establishment of the formalism or the rules according to which the temporal dynamics of the modelled system unfold. (Figure 1).

There are two different approaches: In the general case, experiments must be carried out on the real system and their results then analysed for dependencies and rules using human intelligence alone.

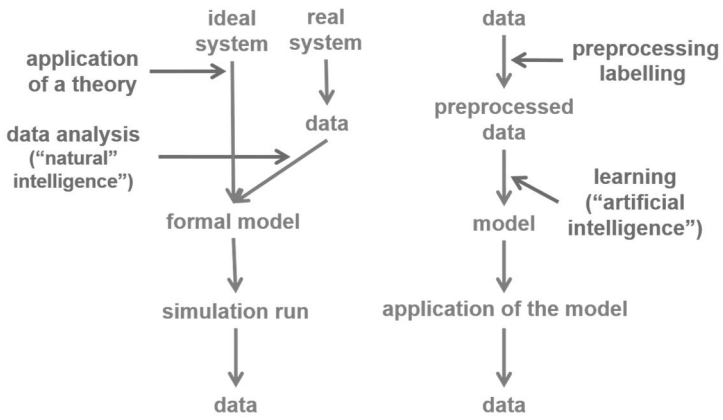

Figure 1: Comparison of the work steps between modelling and data-driven learning processes.

The totality of these rules represents the formal model, which can then be further processed algorithmically - usually in a simulation environment. If there is already prior knowledge about the system to be modelled in that a general theory (e.g. conservation of energy, network theory, etc.) can be used, no explicit system experiments are necessary.

Instead, the laws of the theory are applied, from which the formal model can be derived. In both cases, however, the end result is a set of rules that can be used to transform the input data (consisting of initial state and parameter assignment) into a set of output data (results of the simulation run). If this approach is viewed in the form of an input-output box, this box is transparent and the modelled system is represented by an explanatory structural model in the glass box.

1.2 Machine Learning Method

In contrast to the simulation method, many AI learning methods work with a black-box approach: the essential starting point for this is system data that has already been collected. This data must first be carefully pre-processed. Pre-processing usually involves homogenisation and - in the case of supervised learning methods - classification (labelling) of the input according to the expected, correct system response. This classification of the input data sets using human intelligence introduces system knowledge into the process so that a model can then be developed in an automated learning phase without further intervention. In the work phase (model application), this model responds to any input with an output that - again only within the agreed validity range - corresponds to the learnt classification.

1.3 Comparison of Approaches

A significant difference in the resulting model lies in the already explained black-box view of the learning methods on the one hand and the glass-box view of the explanatory simulation models on the other. Accordingly, the learning methods require a statement about the corresponding correct output for each individual input, but no information about the causal relationships. How the output is derived from the respective input does not have to be introduced as rule knowledge. Accordingly, when interpreting the results of learning models, the question of why cannot be systematically clarified because iso-morphic relationships are not necessarily formed between the system and the model that replicate the causal chain of the system.

Another difference lies in the amount of system data required: Not only must the learning data contain all possible classes of result data, it must also be available in such large numbers that the statistical approaches used in automatic learning can assume a sufficiently large population. In contrast, the rules of the glass-box model can also be found or derived from a small amount of data, even without any system data at all when using the theory approach.

However, uncertainties often arise when setting up the rule set for simulation models, which an algorithmic model specification does not allow due to the requirement of unambiguousness. In these cases, the introduction of randomised parameters that obey defined distributions helps. However, this approach practically always and necessarily entails a complex statistical treatment of the simulation results. Thus, the savings in terms of the amount of input or learning data are relativised in the end by a higher effort on the output side, because the results of a simulation run alone are not meaningful and must be statistically validated by a large number of simulation runs in the sense of a random experiment.

With these general considerations in mind, constructive synergies between the two different approaches will now be presented in the form of five use cases.

2 Combined AI and Simulation Methods: Use-Cases

The use cases described below highlight approaches to the combined use of AI methods and simulation that have actually been realised and are not just available in the form of research results or pilot studies.

For this purpose, a Google search was carried out on the web using the search terms "AI and Simulation".

The pages listed here deal directly and intensively with this topic:

- Simplan [6]
- Siemens "Simultelligence" [7]
- Anylogic [8]
- Mathworks [9]
- Fraunhofer IISB Erlangen [10]
- Merkle CAE Solutions GmbH [11]

Although each of these providers has a slightly different focus, there are strong similarities and overlaps that can be summarised in the typical use cases presented here. Although one source did not contribute directly to the development of the use cases, it should be noted here as an aside: If a coupling of AI and simulation succeeds conceptually and in terms of software technology, the LRZ Munich points out that the fundamentally different hardware concepts required for efficient calculation must then also be combined and optimised. [12]

2.1 Using ChatBot for Knowledge Engineering and System Analysis

The first use case supports a process step in the development of simulation models that was not explicitly mentioned in the description in Section 1, but nevertheless constitutes an important part of the work on the way to a correct, complete and consistent model: system analysis and knowledge engineering, which is often carried out in the form of interviews with experts from the target domain of the model to be developed during the analysis phase. These tie up the time of experts with system knowledge. Many questions relating to model development could be clarified with the help of a chatbot that accesses the existing database of the application domain.

It will certainly not be possible to answer all questions, but such an application should significantly reduce the time other-wise required for expert interviews. On the research side, a similar approach was investigated by Freydenlund et al [5].

2.2 Analysing Online Sensor Data using Pre-trained Learning Models

A second use case is the coupling of an AI-based, pre-trained model with online sensor data under real-time conditions. However, this naturally requires the AI model to have been trained with all potential states of the system beforehand.

In addition, the question arises as to whether simply recognising the irregularity is sufficient or whether the system's set of rules must also be transparent in order to take countermeasures.

2.3 Generating Learning Data for AI using Simulation Models

It is often problematic to obtain consistent learning data for the learning phase of the AI. Such data could be generated artificially through classic simulation. The advantage: it is structured, classified and can be generated in any quantity, subject to computing time. However, the double modelling effort is immediately apparent: both a simulation model and an AI model are used.

Glass-box system understanding must be available in order to be able to generate learning data in a meaningful way. The real-time speed of the AI approach therefore comes at the cost of considerable additional effort in the design phase. In addition, the problem of "rare events" becomes relevant: Even if these have been explicitly generated as learning data through prior simulation, it must be ensured that they are correctly recognised and learned as such by the AI and not ignored as outliers.

2.4 Testing the AI Model in a Virtual Simulation Environment

Conversely, a simulation model can be used to test the AI model: The AI model is coupled with a digital twin in the form of a simulation model of the target environment and so its subsequent use in the real system can be safely tested in this virtual environment. Again two models, the simulation model and the AI model must be developed for this scenario.

A similar scenario arises when AI-supported simulation models are coupled uni- or bidirectionally with IoT sensors, drones or other physical entities. [13] This coupling enables the continuous adaptation of the simulation state to the real system state.

2.5 'Hybrid' Simulation Models

The last use case deals with the situation where the system knowledge in a complex, modular-hierarchical model is not sufficient to describe the behaviour of individual components based on rules. If the interface is known, these components could be replaced by an AI model previously trained on a black box basis.

In this case, no causal relationships need to be specified at this point of detail, although the interpretation of the results of the overall model becomes more complicated with this type of model design because the causal chain is interrupted by the affected model component.

3 Are the Approaches Equivalent in Terms of their Results?

As the sources cited in each case show, the use cases presented in Section 2 are state of the art and can be pragmatically adapted to the task and evaluated in terms of costs and benefits. However, the question arises as to whether there is further potential that is not yet covered by these use cases. One point of reference is the frequently described experience that automatic data analysis reveals system relationships that were previously unknown.

With this in mind, one might ask whether the results obtained from classical simulation on the one hand and those generated by AI approaches on the other are or can be equivalent. Or is it conceivable that AI-based methods produce results that could not be achieved through classical simulation? The same applies, of course, in the opposite direction: are there results from the simulation approach that cannot be explored using AI methods?

The following setup is intended to provide an outlook on future research activities. A complex, possibly adaptive input-output system is given, which is modelled once by a rule-based simulation model and alternatively by an AI/ML model.

If we now consider the quantity of results that the two approaches deliver, three different cases arise in the general case: The sets of results of the approaches completely overlap (a), they are disjoint (b), or there is the case of a true intersection (c). It can be assumed that cases b) and c) are more realistic, as both approaches are already used in practice and at least comparable results are obtained. However, the question then arises whether complete equivalence (case c) can actually be observed, or whether there are system states that only become visible when one of the both approaches is used.

The authors' subjective and preliminary recommendation is therefore to "think together" simulation and AI. This combined exploration of the state space of a complex system promises interesting and possibly new insights into the dynamics of the system modelled.

Publication Remark

This contribution is the revised English version of the (German) conference version published in
Tagungsband Kurzbeiträge ASIM SST 2024,
ARGESIM Report AR 46, DOI 10.11128/arep.46,
ISBN ebook: 978-3-903347-64-9, pp 17-20

References

[1] Nordas HK, Klügl F. Drivers of Automation and Consequences for Jobs in Engineering Services: An Agent-Based Modelling Approach. *Front. Robot. AI,* Bd. 1 of 2,Volume 8 - 2021, 10 05 2021.

[2] Daugherty P, Ghosh B, Narain K. A new era of generative AI for everyone. 01 06 2024. [Online]. Available: https://www.accenture.com/content/dam/accenture/final/accenture-com/document/Accenture-A-New-Era-of-Generative-AI-for-Everyone.pdf.

[3] Strack R, Carrasco M, Kolo P. The Future of Jobs in the Era of AI. 01 06 2024. [Online]. Available: https://www.bcg.com/publications/2021/impact-of-new-technologies-on-jobs.

[4] Pultarova T. Will artificial intelligence replace engineers? 01 06 2024. [Online]. Available: https://www.imeche.org/news/news-article/feature-will-artificial-intelligence-replace-engineers.

[5] Frydenlund E, Martinez J, Padilla JJ, Palacio K, Shuttleworth D. Modeler in a box: how can large language models aid in the simulation modelling process?. *Simulation: Transactions of the Society for Modeling an d Simulation International,* pp. 1-23, 2024.

[6] Simplan. Künstliche Intelligenz. [Online]. Available: https://www.simplan.de/services/kuenstliche-intelligenz/. [Accessed 01 06 2024].

[7] SIEMENS AG. Simultelligenz. [Online]. Available: https://www.siemens.com/de/de/unternehmen/stories/forschung-technologien/kuenstliche-intelligenz/simultelligence.html. [Accessed 01 06 2024].

[8] Anylogic. [Online]. Available: https://www.anylogic.com/features/artificial-intelligence/?utm_source=youtube&utm_medium=social-organic. [Accessed 01 06 2024].

[9] Mathworks. 4-proven-applications-for-your-ai-algorithms. [Online]. Available: https://de.mathworks.com/company/technical-articles/4-proven-applications-for-your-ai-algorithms.html. [Accessed 01 06 2024].

[10] Fraunhofer IISB Erlangen. Augmented Simulation. [Online]. Available: https://www.iisb.fraunhofer.de /en/research_areas/simulation/ai-augmented-simulation.html. [Accessed 01 06 2024].

[11] Merkle CAE Solutions. Künstliche Intelligenz. [Online]. Available: https://www.merkle-partner.de/leistungen/kuenstliche-intelligenz. [Accessed 01 06 2024].

[12] Leibniz Supercomuting Centre München. [Online]. Available: https://www.lrz.de/presse/ereignisse/2021-05-04-SuperMUC-NG-Phase-2_DE/. [Accessed 01 06 2024].

[13] Clemen T, Ahmady-Moghaddam N, Lenfers U. Multi-Agent Systems and Digital Twins for Smarter Cities. *Proceedings of the 2021 ACM SIGSIM Conference on Principles of Advanced Discrete Simulation, 1(1), 45–55.,* pp. 45-55, 2021.

Ultrafine Particles and the Occurrence of Heavy Rain: Model-Based Search for a Causal Relationship on Base of Open Data

Franziska Raabe, Stefanie Steinbichl, Jochen Wittmann*

Univ. of Applied Sciences HTW Berlin, Environmental Informatics, Wilhelminenhofstraße 75A, 12459 Berlin, Germany; **jochen.wittmann@HTW-Berlin.de*

SNE 35(3), 2025, 137-142, DOI: 10.11128/sne.35.tn.10743
Selected ASIM SST 2024 Postconf. Publication: 2024-12-10
Rec. Impr. English version: 2025-06-27; Accepted: 2025-07-15
SNE - Simulation Notes Europe, ARGESIM Publisher Vienna
ISSN Print 2305-9974, Online 2306-0271, www.sne-journal.org

Abstract. Investigating the influence of ultrafine particles (UFP) on heavy rainfall events reveals a nuanced relationship between atmospheric composition and weather phenomena. This paper analyzes heavy rainfall events around the region of Frankfurt Airport and UFP data acquired by the Hessian Agency for Nature Conservation, Environment and Geology, and discusses what influence UFP may have on the hydrologic cycle. While a direct correlation remains inconclusive, daily average analysis suggests a potential link between elevated UFP counts and impending heavy rainfall, affecting the hydrologic cycle. Further in-depth analysis is required to validate this supposition and better understand the effects of UFP´s influence on the hydrologic cycle.

Introduction

Extreme weather events, including heavy rainfall and prolonged drought periods, are on the rise globally. A pioneering study conducted by researchers from the Karlsruhe Institute of Technology and the independent institute Airborne Research Australia explores the connection between ultrafine dust or particles (UFP) in the atmosphere and their disruptive impact on the hydrologic cycle - particularly cloud physics and rainfall formation.

The study underscores that anthropogenic UFP emissions alter precipitation patterns and contribute to heavy rainfall events by serving as cloud condensation nuclei [1]. Moreover, it has already been established that the quantity of UFP has notably increased in recent decades [2].

Particulate matter refers to airborne aerosol particles, including dust particles or droplets of specific sizes, capable of remaining suspended in the atmosphere for several days before settling to the ground [3]. These particles are typically classified based on their aerodynamic diameter into PM10 (particulate matter with a diameter less than 10 μm) and PM2.5 (with a diameter less than 2.5 μm). UFP, measuring up to 100 nm in diameter, are considerably smaller than PM10 particles. They are primarily produced by the combustion of fossil fuels in exhaust gas purification systems, large combustion plants, as well as from air and maritime traffic. Due to their small size, UFP can deeply penetrate into the human body, reaching lung tissue and the bloodstream, where they have been shown to cause respiratory and cardiovascular diseases along with neurodegenerative diseases such as dementia, Alzheimer's and Parkinson's [2][4][5].

Heavy rain, a weather phenomenon characterized by substantial amounts of precipitation in a short period of time and small geographical area, typically originates from convective clouds like cumulonimbus clouds.

This precipitation can lead to floods, landslides, or flash floods, causing significant harm to the environment, buildings and infrastructure. Therefore, the German Meteorological Service (Deutscher Wetterdienst, DWD) issues severe weather warnings when expected rainfall reaches 15 liters per square meter within an hour or 20 liters within six hours [6].

The impacts of climate change are significantly shaping the frequency and intensity of these extreme precipitation events. Research from the World Weather Attribution indicates that heavy rainfall occurrences in Germany and some neighboring countries have seen a surge, with probabilities increasing by 1.2 to 9 times due to human-induced global warming.

Additionally, the studied areas have shown that heavy rainfall intensity has risen by 3 to 19% [7]. Carbon dioxide drives warming and increases water vapor capacity of the atmosphere. However, due to its long lifespan and uniform atmospheric distribution, carbon dioxide cannot solely account for the observed uptick and high variability in frequency and distribution of heavy rainfall occurrences. An understanding of the hydrologic cycle´s dynamics is therefore essential to comprehending these changes [8].

1 Problem Statement

Due to their impact on both the quantity and size of water droplets in cloud formation in the atmosphere, UFP can disrupt the hydrologic cycle by impeding precipitation. Typically, water droplets ranging from approximately 0.01 to 0.25 mm in diameter coalesce around a cloud condensation nucleus (CCN) measuring roughly 0.0002 mm. Once the combined total size of droplets and CCN has reached 1 to 2 mm, they can descend to the earth as raindrops, surpassing the updraft speed within a cloud.

Due to their diminutive size and highly curved surface, which hastens water evaporation, UFP are poor CCN. As a result, the droplets which accumulate around an UFP remain too small to overcome air resistance for an extended period of time. This process generates an additional energy reservoir in the mid-troposphere, promoting extreme rainfall. When these highly enriched clouds eventually precipitate, the resulting rainfall events are notably more intense and moisture-laden. Regions exhibiting significantly heightened UFP levels increasingly experience extreme heavy rainfall and decreasing overall precipitation [1][2][9].

For this investigation an analysis was conducted, using a specific example to explore the potential link between elevated UFP concentrations in the atmosphere and the occurrence of particularly intense heavy rainfall events in a chosen region.

The Frankfurt Airport region served as the study area, because turbine exhaust emissions from aircrafts have been identified as a major source of UFP emissions when operating on the ground [10]. Furthermore, this region stands out as one of the few in Germany where continuous monitoring of UFP concentration is carried out. This lack of data collection is primarily attributed to the absence of legal regulations concerning UFP emissions [11].

The objective of this study is to investigate the connection between UFP and heavy rainfall occurrences using freely accessible data, with the aim of implementing automated analysis and visualization techniques through a GIS dashboard in the near future. This approach could facilitate more extensive analyses of relationships and enhance the presentation of results in a visually engaging manner.

2 Data Material

Measuring UFP values requires special techniques, as the particles, owing to their diminutive size, contribute minimally to the particle masses of coarser fine dust categories such as PM2.5 and PM10 [12]. Instead of mass determination, devices for particle counting are employed [13].

This study sourced UFP data from the Measuring Data Portal of the Hessian Agency for Nature Conservation, Environment and Geology (HLNUG), which has been collecting UFP data at varying numbers of air monitoring stations in and around Frankfurt Airport since 2015 [14]. Categorization is based on particle size ranging from 10 to 500 nm. For this study, particle sizes ranging from 10 to 100 nm were considered, aligning with the common definition of UFP. Aircraft emissions are primarily associated with the release of UFP sized between 10 and 30 nm [13].

The heavy rainfall data used in this study is sourced from the DWD's catalog of radar-based heavy rainfall events (CatRaRE) [15]. This comprehensive catalog encompasses all heavy rainfall events in Germany dating back to 2001. Unlike large-scale, prolonged precipitation, locally and temporally limited heavy rainfall events pose a challenge for measurement. To acquire reliable data, the DWD employs weather radars capable of extensively scanning the areas surrounding the radar device, effectively capturing duration and intensity of precipitation, even beyond regular measuring stations. Thereafter, the collected datasets undergo a multi-stage quality control process, to ensure their suitability for climatological analysis [16].

3 Combined Methods

Initially, the heavy rainfall data was imported into ArcGIS and filtered based on the chosen observation period. To ensure data consistency, the period from May 1, 2020, to December 23, 2022, was selected for investigation.

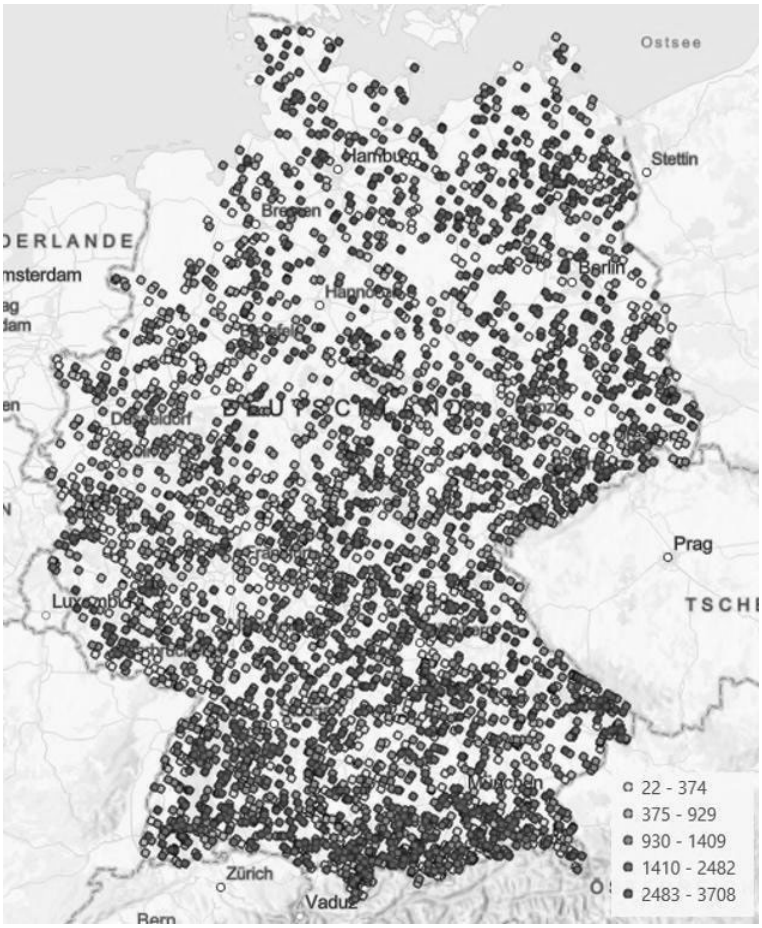

Figure 1: Number of most intense heavy rainfall events in Germany from May 1, 2020, to December 23, 2022.

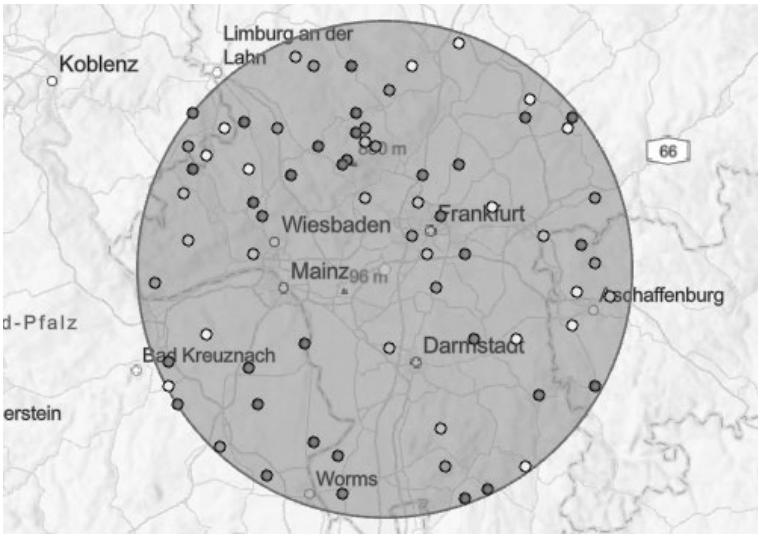

Figure 2: Intersect of buffer layer (50 km around Frankfurt Airport) and heavy rainfall events.

Furthermore, the most intense heavy rainfall events were identified and selected using criteria such as the maximum precipitation within the event zone (RRmax), the maximum heavy rainfall index (SRImax), and duration stage of the event (Duration) (see Figure 1).

A 50 km buffer was then centered on Frankfurt Airport, creating a polygon layer that was pairwise intersected with the point layer representing the selected heavy rainfall events (see Figure 2).

From the most intense heavy rainfall events identified in the studied region, two events per year from 2020, 2021, and 2022 were selected for sample analysis. The UFP data from the seven days preceding each heavy rainfall event was imported, with the heavy rainfall event occurring on the last day (Day 0). For each particle size category, the upper and lower quartiles along with the respective daily mean value, were determined for each measurement period. This analysis enabled insights into the distribution of higher and lower UFP measurements in the days leading up to the heavy rainfall event (see Figure 3 to Figure 6).

4 Results

In the exemplary illustrated measuring periods from May 28, 2021, to June 3, 2021 (see Figures 3 and 4), and from September 8, 2022, to September 14, 2022 (see Figure 5 and 6), the UFP values across all particle size categories indeed exhibited a distribution pattern. Lower concentrations were predominantly observed at the beginning of the period, indicated by a left-skewed chart in the lower quartile, while higher concentrations tended to occur towards the end of the period, as indicated by the right-skewed chart in the upper quartile.

This phenomenon was also noted in some of the other analyzed samples, albeit not consistently enough to establish a clear trend or regularity. The behavior of quartile captures appeared rather unpredictable, given the varied distribution of data captures in each dataset.

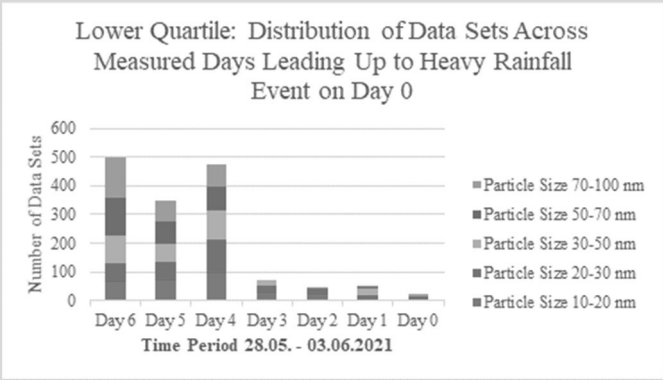

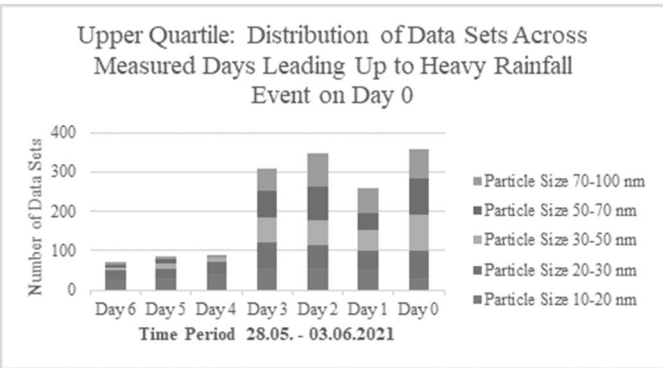

Figure 3: Charts depicting the distribution of data sets per measurement day in the lower quartile (proportion of measurements with lowest UFP values) and in the upper quartile (proportion of measurements with highest UFP values) for the measurement period from May 28, 2021, to June 3, 2021, for each particle size category.

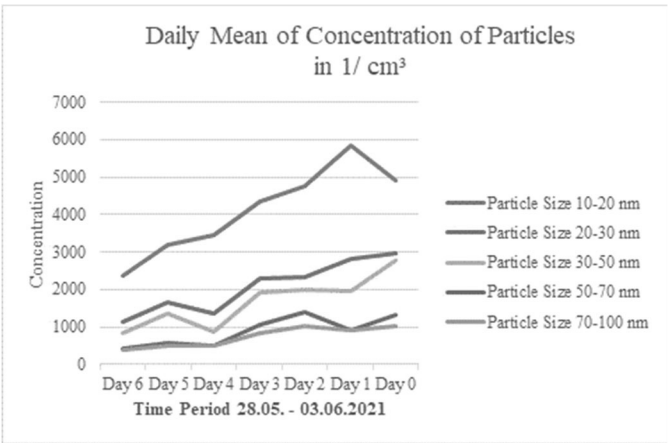

Figure 4: Time series plot of daily mean values per particle size category for the measurement period from May 28, 2021, to June 3, 2021.

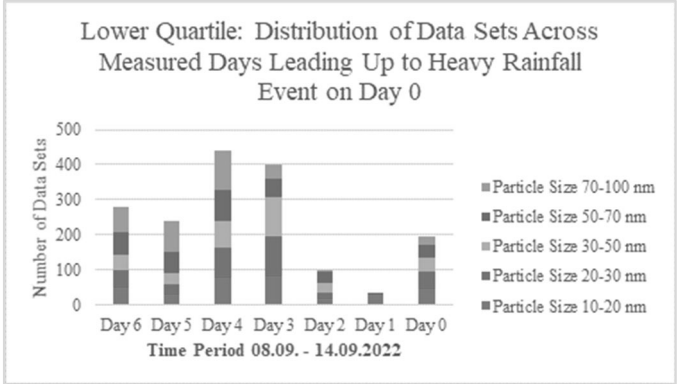

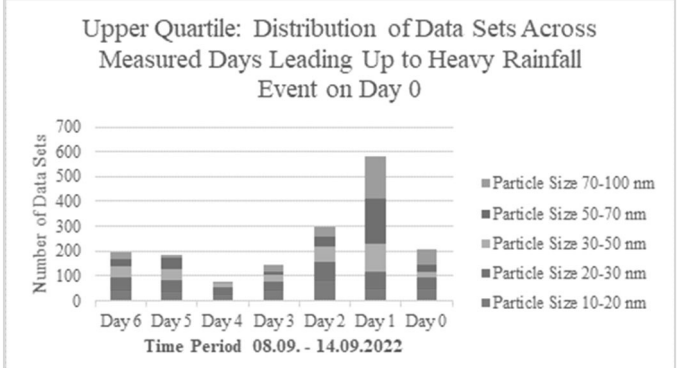

Figure 5: Charts depicting the distribution of data sets per measurement day in the lower quartile (proportion of measurements with lowest UFP values) and in the upper quartile (proportion of measurements with highest UFP values) for the measurement period from Sept. 8, 2022, to Sept. 14, 2022, for each particle size category.

In analyzing the daily mean values of the UFP concentrations, it was noted that 20 out of 30 generated curves exhibited an increase in values in temporal proximity to the heavy rainfall event.

However, the curves displayed varying patterns. For instance, some curves showed peaks at the beginning of the observed period and then a dip in the middle of the period. Others displayed a continuous increase, only to decrease again towards the end of the period.

Nonetheless, a common observation was that the majority of curves featured the highest daily mean value within the measurement period one to two days before the occurrence of the heavy rainfall event.

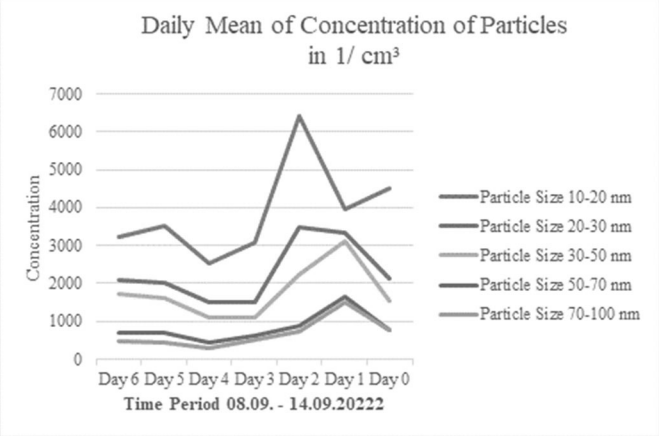

Figure 6: Time series plot of daily mean values per particle size category for the measurement period from September 8, 2022, to September 14, 2022.

5 Conclusions

The present study did not find sufficient evidence to establish a direct correlation between increased UFP pollution in the atmosphere and the occurrence of heavy rainfall events. Given the complexity of weather and climate phenomena, more extensive analysis is necessary. This analysis should encompass influencing factors such as altitude data, terrain profiles, temperature, general precipitation, air pressure and wind movements. For instance, wind and precipitation can impact local UFP concentrations. Clouds can disperse depending on wind strength and velocity, moving the potentially correlated heavy rainfall event to an area away from the region with increased UFP concentrations [We22].

The analysis of daily mean value did indeed provide suggestive evidence of a potential increase in determined UFP emissions leading up to a heavy rainfall event. However, to solidify this assumption, a study of significantly larger scope would be required. Additionally, analyses at various locations are essential for a more precise investigation. This would not only facilitate local comparisons but also enable the correlation of results from different regions with similar geographical conditions.

In order to facilitate a comprehensive analysis of the relationship between UFP pollution and heavy rainfall events, the implementation of an automated system for evaluating and visualizing freely available data via a GIS dashboard could be highly beneficial. This approach would not only enable the examination of individual data points but also facilitate the identification of complex patterns and trends within the data.

Moreover, it would allow for the adoption of various spatial and temporal scales for modeling, thus enhancing the understanding of relationships and providing a more robust foundation for further research and decision-making. Furthermore, such a system could foster communication and information exchange among different interest groups, which is vital for developing measures to mitigate the potential impact of UFP on the hydrologic cycle and the environment as a whole.

In conclusion, as UFP pollution continues to rise steadily over time, this study endeavors to establish an initial foundation and impetus for further analysis. The ultimate goal is to ascertain the potentially significant impact of UFP on the hydrologic cycle and subsequently implement measures to mitigate them. This could include the establishment of an official UFP limit to regulate emissions.

Publication Remark

This contribution is the revised English version of the (German) conference version published in
Tagungsband Langbeiträge ASIM SST 2024,
ARGESIM Report AR 47, vol. DOI 10.11128/arep.47,
ISBN ebook: 978-3-903347-65-6
article DOI 10.11128/arep.47.a4712, p 67-72.

References

[1] Junkermann W, Hacker J. Unprecedented levels of ultrafine particles, major sources, and the hydrological cycle. Sci Rep 12, 7410, 2022.
DOI 10.1038/s41598-022-11500-5

[2] Freund A. Ultrafeinstaub für Wetterextreme mitverantwortlich. Deutsche Welle.
https://www.dw.com/de/ultrafeinstaub-f%C3%BCr-wetterextreme-mitverantwortlich/a-61903127,
Accessed: 06.09.2023, 2022.

[3] Kinne S, Quaas J. Einfluss der Luftverschmutzung auf den Klimawandel – neue Erkenntnisse aus Satelliten daten und Klimamodellen.
https://www.mpg.de/405815/forschungsSchwerpunkt,
Accessed: 06.09.2023, 2007.

[4] Initiative Klima-, Umwelt- und Lärmschutz e.V.: Feinstaub und noch feinerer Staub – Ultrafeinstaub.
https://www.klima-umwelt-luftverkehr.de/umwelt/ultrafeinstaub/
Accessed: 22.08.2023.

[5] Umweltbundesamt: Feinstaub.
https://www.umweltbundesamt.de/themen/luft/luftschadstoffe-im-ueberblick/feinstaub#undefined,
Accessed: 22.08.2023, 2022.

[6] Deutscher Wetterdienst: Wetter und Klimalexikon. Starkregen. https://www.dwd.de/DE/service/lexikon/Functions/glossar.html?nn=103346&lv2=102248&lv3=102572, Accessed: 04.09.2023.

[7] Kreienkamp F, et al. Rapid attribution of heavy rainfall events leading to the severe flooding in Western Europe during July 2021. https://www.worldweatherattribution.org/wp-content/uploads/Scientific-report-Western-Europe-floods-2021-attribution.pdf, Accessed: 04.09.2023, 2021.

[8] Karlsruher Institut für Technologie. Klimaforschung: Ultrafeinstaub könnte Wetterextreme verursachen. https://www.kit.edu/kit/pi_2022_044_klimaforschung-ultrafeinstaub-konnte-wetterextreme-verursachen.php, Accessed: 06.09.2023, 2022.

[9] Weishaupt M. Dürre und Starkregen: Fossile Brennstoffe verändern Wasserkreislauf. https://www.nationalgeographic.de/umwelt/2022/05/duerre-und-starkregen-fossile-brennstoffe-veraendern-wasserkreislauf, Accessed: 06.09.2023, 2022.

[10] Umweltbundesamt. Einfluss eines Großflughafens auf zeitliche und räumliche Verteilungen der Außenluftkonzentrationen von Ultrafeinstaub < 100 nm, um die potentielle Belastung in der Nähe zu beschreiben - unter Einbeziehung weiterer Luftschadstoffe. https://www.umweltbundesamt.de/sites/default/files/medien/11850/publikationen/14_2021_texte_grossflughafen_.pdf, Accessed: 25.04.2024, 2021.

[11] Umweltbundesamt. Fragen und Antworten: Ultrafeine Partikel. https://www.umweltbundesamt.de/themen/luft/luftschadstoffe-im-ueberblick/feinstaub/fragen-antworten-ultrafeine-partikel, Accessed: 25.04.2024, 2018.

[12] Hessisches Landesamt für Naturschutz, Umwelt und Geologie. Ultrafeine Partikel. https://www.hlnug.de/themen/luft/luftqualitaet/sondermessprogramme/ultrafeine-partikel, Accessed: 06.09.2023.

[13] Peil K. Ultrafeine Partikel (UFP): Flugverkehr und Gesundheit. Fakten - kurz und bündig erstellt vom BUND AK Luft/Klima/Lärm Hessen. https://www.bund-hessen.de/fileadmin/hessen/Publikationen/Arbeitskreise/AK-Luft-Klima-Laerm/2021-02_BUND-Hessen_FactSheet_Ultrafeine-Partikel_final.pdf, Accessed: 06.09.2023, 2021.

[14] Hessisches Landesamt für Naturschutz, Umwelt und Geologie. Messdatenportal. https://www.hlnug.de/messwerte/datenportal/ufp, Accessed: 06.09.2023.

[15] Lengfeld K, Walawender E, Winterrath T, Weigl E, Becker A. Starkregenereignisse Version 2023.01 mit Überschreitung der DWD-Warnstufe 3 für Unwetter basierend auf RAD-KLIM-RW Version 2017.002 Parameter und Polygone der Starkregenereignisse in Deutschland version v2023.01. Deutscher Wetterdienst, 2023. DOI 10.5676/DWD/CatRaRE_W3_Eta_v2023.01.

[16] Winterrath T. Niederschlagsklimatologie: Daten und Produkte - Mit Radardaten in die nächste Dimension. Deutscher Wetterdienst. https://www.dwd.de/SharedDocs/broschueren/DE/klima/radklim_broschuere.pdf?__blob=publicationFile&v=2, Accessed: 06.09.2023, 2021.

Implementation of a Smart Grid in an Operation-independent Simulation Model

Julian Stromberger*, Johannes Dettelbacher, Alexander Buchele

Competence Centre for Industrial Energy Efficiency, University of Applied Sciences Ansbach, Residenzstraße 8, 91522 Ansbach, Germany; *j.stromberger@hs-ansbach.de*

SNE 35(3), 2025, 143-147, DOI: 10.11128/sne.35.sn.10744
Selected ASIM SST 2024 Postconf. Publication: 2024-12-10
Rec. Impr. English version: 2025-08-01; Accepted: 2025-08-15
SNE - Simulation Notes Europe, ARGESIM Publisher Vienna
ISSN Print 2305-9974, Online 2306-0271, www.sne-journal.org

Abstract. This study describes the development of an operation-independent simulation model for electrified die-casting foundries which use a smart grid system to cover their energy requirements. The model uses real weather and electricity price exchange data for the simulation period. It can be used to determine and compare electricity costs for production at specific times of day and year, as well as the economic efficiency of different photovoltaic (PV) system and electricity storage variants. It also enables the proportion of different energy sources for each configuration to be analysed. This can be carried out using the model for locations throughout Germany. Additionally, this paper presents exemplary simulation studies that demonstrate the model's wide range of applications. The results provide an initial overview of the potential savings and optimisation. In the future, the model will provide a basis for determining optimum plant layouts and production times using simulation-based optimisation.

Introduction

Against the backdrop of climate targets and the European Supply Chain Directive, reducing emissions during production is becoming increasingly important, particularly for energy-intensive companies. At the same time, companies are focusing on sourcing energy in the most cost-effective way possible. However, these aspects do not necessarily compete with each other. The volatility of renewable energies means that emission-free electricity can sometimes be sourced very cheaply, making CO_2-emissions and low-cost electricity procurement compatible.

Additionally, manufacturing companies with suitable sites can generate their own renewable electricity, although this initially incurs high investment costs and requires a certain degree of logistical flexibility, which is not always easy to implement. To be able to test and analyse the economic effects of corresponding adaptations in companies without having to intervene in real operations, which is always associated with economic risks, this study will develop a simulation model for this purpose. As part of this work, this functionality is implemented in an existing operating model of casting plants. To enable statements to be made about different company sizes and to allow for possible transferability to other sectors, the model is company-independent and geared towards flexibility.

1 Field of Application

With an average annual demand of 12.6 TWh between 2010 and 2021, the German foundry industry is one of the most energy-intensive sectors of the economy. In 2021, more than half of this demand was still covered by fossil fuels [1]. In order to reduce the resulting emissions, it is unavoidable that these fossil fuels must be substituted. The most important approach is to electrify the melting process. However, the effectiveness of this measure depends heavily on the composition of the electricity mix used. Additionally, this conversion alters the operating process [2]. This study analyses a simulation model of a converted plant. The model aims to determine the energy costs of production for any configuration of such an operation using a smart grid system that considers weather data, electricity storage, and electricity exchange prices. In this application, the smart grid system is limited to the site in question. Its task is to monitor electricity demand during production and cover it as cost-effectively as possible using the currently available electricity supply, which is also recorded.

2 Previous Work

The simulation model developed in this study is based on previous work, in which two models were developed: an operation-independent model for a conventional die casting operation [3], and a specific model for an electrified operation [2]. This study focuses on implementing a smart grid approach using real-time data and variable electricity costs resulting from production. The use of flexible energy prices and smart grids to optimise costs in the manufacturing industry is a widely discussed topic in the literature. Literature analyses such as [4] can be consulted for an overview.

Table 1 provides an overview of the focal points of studies in this area, compared to this study. This study is the first to analyse operational smart grids in a foundry context alongside real weather and electricity price data.

Contents	[5]	[6]	[7]	[8]	This study
Simulation study	*	*	*	*	*
Felxible energy prices	*		*	*	*
On-site power generation				*	*
Electricity storage				*	*
Real weather data					*

Table 1: Comparison of the focus of different studies.

3 Simulation Model

The simulation model is based on the conservation laws of energy and mass, and has been developed using the MATLAB/Simulink programming environment. It has an object-oriented structure and can be individually parameterised via a configuration file before a simulation is started. The simulation uses real start and end times to retrieve weather and electricity price data. The model comprises three sub-models. Figure 1 shows the interaction of the sub-models within a simulation step. One simulation step corresponds to one second of simulated operating time.

Combining a detailed simulation model of a die-casting foundry with real weather data and electricity prices allows for insights into energy costs and the energy mix in various simulation scenarios.

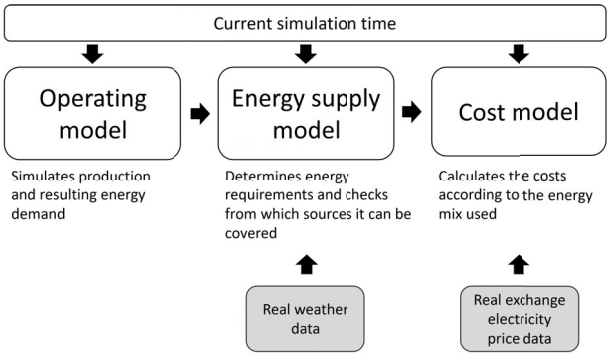

Figure 1: Procedure of the simulation model in each simulation step.

Thus, the model can support and evaluate strategic decisions. More detailed explanations of the individual sub-models can be found below.

3.1 Operating model

The model is based on the principles of energy and mass conservation and maps the entire production process from melting to casting in an object-oriented manner. It considers energy and material flows together, while a control module regulates the overall process. Energy flows are simulated continuously and material flows are simulated discretely. Calculations in the energy model are based on the internal energy of the processed metal. This is shown schematically in Figure 2. Using these calculations, the model determines the current temperature and solves the differential equations for the mass of the liquid and solid metal. In the discrete part of the model, each simulation step checks for the occurrence of certain events. If necessary, processes are triggered accordingly.

$$E_{in} \Rightarrow \boxed{\frac{dU}{dt} = E_{in} - E_{out} \quad U = U_{start} + \int \frac{dU}{dt}\,\mathrm{dt}} \Rightarrow E_{out}$$

U = internal energy of the metal
U_{start} = internal energy at the start time
$E_{in/out}$ = incoming and outgoing flow of energy $flow$

Figure 2: Internal energy of the processed metal.

The model consists of various simulation objects whose properties change during the simulation according to the parameters of the simulated operation.

3.2 Energy supply model

In the simulation, only the electricity required to operate the melting furnaces is taken into account. This electrictiy is determined by adding the energy required by each furnace and the heat losses that occur in each simulation step. The electrical energy required for operation can be provided in the simulation model in three ways (more detail on the various sources is provided below):

1. Electrical energy from the PV system
2. Electrical energy from the battery storage system
3. Electrical energy from the power exchange

Figure 3 shows the sequence of utilisation of these energy sources schematically:

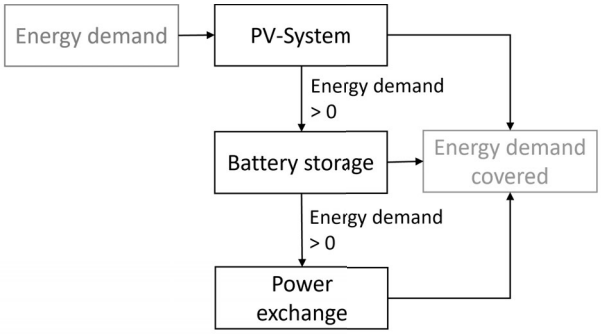

Figure 3: Order of electricity usage.

Electrical energy from the PV system. The yield of the PV system is calculated using the weather data from the Duett project [9], which has been providing hourly data with a local resolution of 2x2 km for the whole of Germany since the beginning of 2024, depending on the specific system data and the stored operating location.

Electrical energy from the battery storage system. The battery storage system is charged when more PV electricity is produced than the site currently requires and discharged when more electricity is required than is currently being produced. A certain degree of efficiency is associated with electricity storage.

Electrical energy from the power exchange. If the energy demand cannot be met by the electricity currently being generated and stored, the difference is purchased on the European Power Exchange (EPEX SPOT) spot market.

3.3 Cost model

The costs of the PV system and battery storage are calculated using straight-line depreciation for both acquisition and operating costs. Electricity purchased from the spot market is included in the total costs at the current price and required quantity for each time step. Accordingly, the energy costs C in each simulation step consist of fixed and variable costs according to equation 1:

$$C = \frac{C_{\text{inv}} + C_{\text{op}}}{T} + C_{\text{spot}} \tag{1}$$

C_{inv} = Investment cost
C_{op} = Expected operating costs
C_{spot} = Electricity costs of exchange electricity
T = Expected life cycle

4 Simulation Study

To analyse the model's potential, the electricity mix and resulting costs of an operation with four casting units and an identical production plan are investigated by varying the battery storage sytem, the PV system and the geographical location. Each simulation considers an identical 24-hour operating day. The reference configuration for all studies is an operation with a 1 MWp PV system and 320 kWh storage capacity in Nuremberg. These simulation studies aim to demonstrate the possible applications of the developed model.

4.1 Variation of the storage capacity

The first sub-study analyses the influence of the battery storage system. To this end, the capacity is varied from 0 to 640 kWh, together with the corresponding power. Figure 4 shows the resulting energy mix and associated costs.

The study found that total costs decrease with increasing storage capacity, as a larger storage volume is associated with lower additional costs than purchasing electricity on the spot market. The extent of this effect depends on the storage system's investment costs, the PV system used and spot market prices during the relevant period.

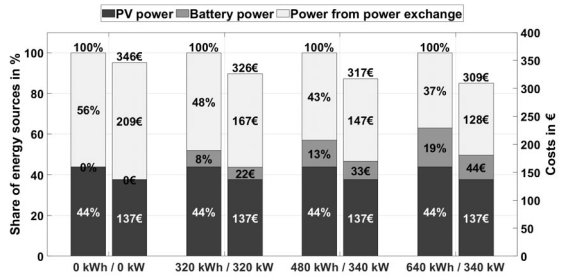

Figure 4: Electricity mix and costs for various batery storage systems.

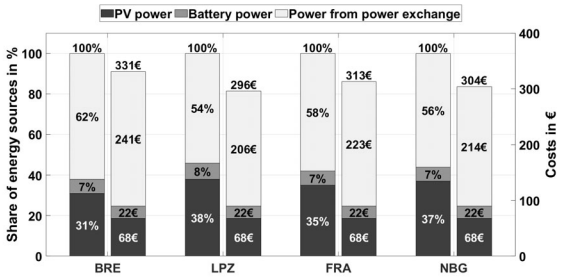

Figure 6: Electricity mix and costs for various production sites.

Accordingly, studies of this type can aid decision-making regarding the optimal size of a new or replacement battery storage system for an operation with existing PV system.

4.2 Variation of the PV system

This simulation study analyses the impact of the size of a PV system. It is varied in four stages, ranging from 100 kWp to 2 MWp. Figure 5 shows the resulting energy mix and associated costs.

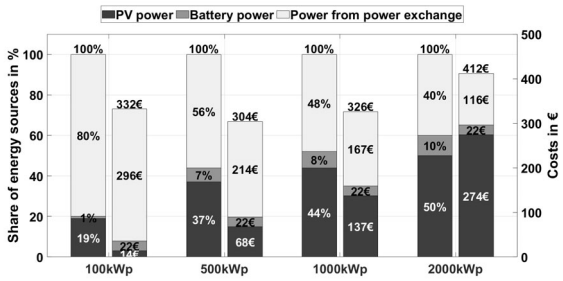

Figure 5: Electricity mix and costs for various PV system sizes.

Although the configuration with the largest PV system produces the most PV electricity, a smaller system (500 kWp) is more cost-effective. This is due to limited storage capacity and production at night.

4.3 Variation of the location

Finally, the factory's location varies between Bremen (BRE), Leipzig (LPZ), Frankfurt am Main (FRA) and Nuremberg (NBG). The simulation is based on the optimal configuration from simulation study 4.2: a 500 kWp PV system with 320 kWh of storage capacity. Figure 6 shows the resulting energy mix and associated costs.

The study shows that, for otherwise identical operations at different locations, the energy mix and energy costs can differ significantly in some cases. This is due to different levels of solar irradiation and the resulting variation in PV yields. Therefore, optimal system configurations depend on the location of the site, and this must be taken into account in the simulation model. Supporting site selection is another potential application of such models. However, a longer time period must be simulated to make an informed statement on site selection.

5 Discussion

The main advantages of the model described here are its flexible structure and the incorporation of real data. This makes the model suitable for a wide range of applications. As the model uses real data on weather and electricity prices, it can also take into account time- and location-specific influencing factors in the simulation. The test studies presented demonstrate the model's suitability for a wide range of applications. For instance, it can be used to determine the optimal size of a storage system for an existing PV system, and vice versa. It is also possible to optimise the design of both components.

Additionally, the model considers specific weather data, enabling its flexible use for different locations. The model can be used to aid strategic investment planning and the assessment of the profitability of changes to the production plan or location choice. As specific acquisition costs can be varied within the model, it can be used to determine the marginal costs above which an investment becomes worthwhile.

However, since a simulation model is always a simplified representation of reality, it is important to validate it using real data in order to confirm its validity.

Due to the lack of electrified foundries, this cannot currently be done for this model. Therefore, the current validation is based on energy balances and a comparison with a validated model of a conventional die casting foundry [3].

6 Outlook

In future, optimisation algorithms will be used to determine the best possible system configurations and production times for specific operations with the help of the model described here. Due to its flexible structure, the model can be extended in many directions. While it is primarily intended for operational production planning, further work will investigate its potential for strategic plant design in particular. Furthermore, the smart grid model can be easily transferred to other industrial application areas. All that is required is a load profile for the new application.

Publication Remark

This contribution is the revised English version of the (German) conference version published in
Tagungsband Langbeiträge ASIM SST 2024,
ARGESIM Report AR 47,
ISBN ebook: 978-3-903347-65-6,
volume DOI 10.11128/arep.47,
article DOI 10.11128/arep.47.a4734, p 61-65.

References

[1] Statistisches Bundesamt. *Statistischer Bericht - Umwelt-ökonomische Gesamtrechnungen (UGR) - Energiegesamtrechnung - 2010 bis 2021*. 2023. Accessed on 13 May 2024: https://www.destatis.de/DE/Themen/Gesellschaft-Umwelt/Umwelt/UGR/energiefluesse-emissionen/Publikationen/Downloads/statistischer-bericht-ugr-energiegesamtrechnung-5850014217005.html.

[2] Dettelbacher J, Schlüter W, Buchele A. *Simulative Analyse der nachhaltigen Transformation von Gussbetrieben*. In: Bergmann, Feldkamp, Souren und Straßburger, editors. *Simulation in Produktion und Logistik 2023*. Ilmenau, 2023. https://doi.org/10.22032/DBT.57476

[3] Schlüter W, Henninger M, Buswell A, Schmidt J. Schwachstellenanalyse und Prozessverbesserung in Nichteisen-Schmelz- und Druckgussbetrieben durch bidirektionale Kopplung eines Materialflussmodells mit einem Energiemodell. In: Wenzel und Peter, editors *Simulation in Produktion und Logistik 2017*, Kassel, 2017.

[4] Hiller T, Mayerhoff J, Nyhuis P. Energy Costs in Production Planning and Control: A Categorical Literature Review and Comparative Analysis. *Journal of Production Systems and Logistics 2021*. Hannover 2021. https://doi.org/10.15488/11126

[5] Ewering C, Siebert R, Wortmann F, Youssef A. Process control with volatile electricity prices. *2014 5th International Renewable Energy Congress (IREC)*; Hammamet, Tunisia, 2014, pp. 1-5, https://doi.org/10.1109/IREC.2014.6827005

[6] Schultz C, Braun S, Braunreuther S, Reinhart G. Integration of Load Management into an Energy-oriented Production Control. *Procedia Manufacturing*. 2017. https://doi.org/10.1016/j.promfg.2017.02.017

[7] Willeke S, Prinzhorn H, Stonis M, Nyhuis P. Preconditions for applying an energy price-oriented sequencing rule. *Prod. Eng. Res. Devel.* 12, 73–81 2018. https://doi.org/10.1007/s11740-017-0782-z

[8] Roesch M, Linder C, Zimmermann R, Rudolf A, Hohmann A, Reinhart G. Smart Grid for Industry Using Multi-Agent Reinforcement Learning. *Applied Sciences*. 2020; 10(19):6900. https://doi.org/10.3390/app10196900

[9] Deutscher Wetterdienst. 2024. Accessed on 13 May 2024: `https://opendata.dwd.de/climate_environment/CDC/grids_germany/hourly/duett/radiation_global/recent/`

Methodology for the Identification of Systems with Non-linear Dynamic Behaviour

Marian Göllner[1*], Sven Jacobitz[1], Xiaobo Liu-Henke[1], Ludger Frerichs[2]

[1]Institute for Mechatronics, Ostfalia University of Applied Sciences,
Salzdahlumer Str. 46/48, D-38302 Wolfenbüttel; *mar.goellner@ostfalia.de*

[2]Institute for Mobile Machines and Commercial Vehicles, Technical University Braunschweig,
Langer Kamp 19a, D-38106 Braunschweig

SNE 35(3), 2025, 149-157, DOI: 10.11128/sne.35.tn.10745
Selected ASIM SST 2024 Postconf. Publication: 2024-12-10
Rec. Impr. English version: 2025-08-01; Accepted: 2025-08-15
SNE - Simulation Notes Europe, ARGESIM Publisher Vienna
ISSN Print 2305-9974, Online 2306-0271, www.sne-journal.org

Abstract. This paper investigates the identification and control of unstable, under-actuated systems with non-linear dynamic behaviour. Due to their instability and non-linear responses to conventional control techniques, these systems pose a particular challenge for precise modelling and effective control. To address these problems, we developed a methodical, model-based approach using rapid control prototyping (RCP), which is based on physical models and integrates model-in-the-loop (MiL), software-in-the-loop (SiL) and hardware-in-the-loop (HiL) testing. The methodological framework includes the identification of system dynamics using measurement data-based approaches and the verification of the models to ensure their accuracy. By applying these models to the specific example of the S-Mobile, a highly dynamic intralogistics system with a spherical electric drive, we demonstrate the effectiveness of the approach. The results show improved model accuracy and robust control of the system, emphasising its potential applicability in similarly complex technical systems.

Introduction and Problem Definition

The modelling and control of intelligent dynamic systems is a fundamental aspect of modern engineering. This task becomes particularly challenging when dealing with unstable, under-actuated systems with non-linear behaviour [1]. Such systems can be found in a variety of applications, from robotics to energy transmission systems, and require precise and reliable models for effective system design. In modern control engineering, the models used are of crucial importance. They are not only used for system design, but are an integral part of the controller functions. Lack of accuracy in modelling can lead to sub-optimal performance and even system failure. Therefore, the identification of system dynamics, especially in non-linear and under-actuated systems, is a key challenge. These systems are characterised by their tendency to respond to conventional control methods with unpredictable or unstable behaviour.

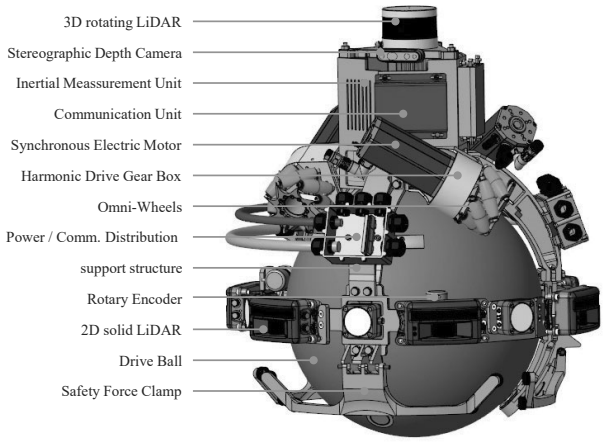

Figure 1: Function carrier S-Mobile as an exemplary non-linear, unstable system.

Figure 1 shows such a system, the S-Mobile function carrier, which is designed as a highly dynamic intralogistics system with a spherical electric drive. It consists of a structure that is balanced on a sphere via rotationally symmetrical actuators using omnidirectional wheels. The primary problem is the identification and validation of the control plant model as an integral part of the control concept (see [2]). The requirements for modelling quality are correspondingly high.

This paper presents the concept of a new methodology for the identification of unstable, underactuated systems taking into account there non-linear systems dynamic.

It is structured as follows. Section 1 introduces the methodology used for model-based development of mechatronic systems and the general model-based identification process.

Section 2 gives an overview over the state-of-the-art for identification of either non-linear or unstable systems. Subsequently, in section 3, the conception and design of the new method and in section 5, the results of the testing approach are laid out in detail. The paper closes in section 6 with a conclusion and an outlook for future work.

1 Methodology

A methodical, model-based approach is essential for the development of complex cyber-physical systems. Figure 2 illustrates the general data-based identification process used for this purpose, according to [3].

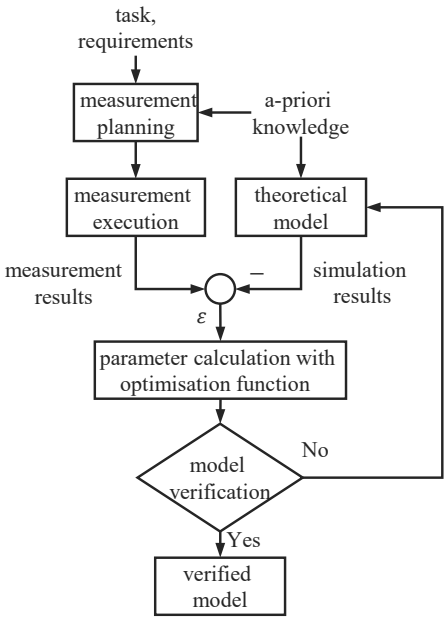

Figure 2: Measurement data-based model identification process.

Holistic, end-to-end, verification-orientated rapid control prototyping (RCP) has established itself as the defacto method in this area.

The core is a white-box model of the system to be controlled based on physical approaches as well as the processes model-in-the-loop (MiL), software-in-the-loop (SiL) and hardware-in-the-loop (HiL). The correctness of the model used is therefore an essential prerequisite for efficient development and valid design results. Model identification and verification are therefore core elements of the modelling process [4].

Based on the task, the requirements and the a-priori knowledge of the system, the measurement is first planned and the parameters of the theoretical model are initially estimated. The difference between the measurement and simulation results ε is used as input for an optimisation function to calculate the parameters. During model verification, an assessment is made as to whether the real behaviour is reproduced with sufficient accuracy. If this is the case, the final model is established. Otherwise, the theoretical model is adapted, for example by increasing the modelling depth.

2 State-of-the Art

Identification in control engineering refers to the experimental determination of the time behaviour of a process or system by analysing measured signals. The aim is to map the system behaviour as accurately as possible within a defined class of mathematical models, whereby the errors between the real process or system and its mathematical models should be minimised. The challenge is to keep the error between the actual system behaviour and its mathematical model as small as possible. Researchers and engineers use measured input and output signals to characterise and model the system dynamics. This process is crucial for the development of precise and efficient control systems, especially in technical fields such as robotics, aerospace and industrial automation, where accurate models are essential for optimal performance [5].

2.1 Classification of identification methods

Identification methods for dynamic systems can be fundamentally divided into two categories according to their basis of analysis: Time domain methods and frequency domain methods [6]. Time domain methods use time series data to characterise the dynamic behaviour of the system. These methods are particularly useful for modelling non-linear relationships between input and output signals [5].

In contrast, frequency domain methods analyse the system behaviour by examining the response of the system to sinusoidal input signals of different frequencies. These methods are effective in determining the system characteristics by analysing the frequency response. Frequency domain methods are particularly suitable for identifying linear systems as they provide a clear and descriptive representation of the system dynamics in the frequency spectrum [7].

In addition, there is a third category, the so-called mixed methods, which combine elements of both approaches in order to utilise the advantages of time and frequency domain analyses. These hybrid approaches are often able to provide a more comprehensive analysis by capturing both the direct time response and the frequency-dependent properties of the system [1].

The methods mentioned in the discussion above assume that the input/output behaviour of a system is measured directly. However, this approach is not practical for unstable systems. In such cases, the use of advanced techniques such as Closed Loop Identification is required [8]. When investigating under-actuated systems, it is also crucial to ensure that all system states are fully excited and analysed.

2.2 Approaches for the identification of non-linear, unstable systems

Current research in the field of system identification provides a wide range of perspectives on the challenges and methods for analysing dynamic systems, especially with the use of artificial intelligence and machine learning [8]. A common approach is to close the control loop to stabilise the system. A distinction is made here between direct (evaluation of the system input and output) and indirect (evaluation of the reference variable and the system output) identification methods. These methods make it possible both to create consistent models and to deal with non-modelled dynamics (approximate modelling) [9]. Xavier et al. [10] provide an in-depth overview.

In the specific application to underactuated systems, Chawla and Singla [11] apply adaptive neural-based fuzzy inference systems (ANFIS). Here, the model of an inverse pendulum is generated from input/output data of the dynamic system response. The accuracy of the ANFIS model is confirmed both by the mean square error and by experimental comparisons with real system models. However, this is a non-physics-based model, which is not suitable for treatment with typical control engineering methods.

Through Chen et al. [12] introduced dual input-output parameterisation (dual IOP), a new method for identifying linear time-invariant systems using closed-loop measurement data. The method represents an extension of previous approaches to closed-loop identification and simplifies the design of the stabilising controller in particular. The applicability for non-linear systems is not discussed.

Finally, González et al. [13] deal with the identification of unstable, continuous systems using refined instrumental variable methods, especially in closed-loop control. It is shown that existing approaches such as the Simplified Refined Instrumental Variable Method (SRIVC) in their conventional form are not reliable when it comes to modelling unstable systems.

As a solution, an adaptation of these methods is proposed, which includes the introduction of a specially adapted all-pass filter in the pre-filtering step. These modified methods allow the identification of unstable systems and minimise the error at convergence. However, the presented method is only intended to be applied to linear systems.

3 Designing the New Method

In order to be able to run through the established model-based design process and, in particular, to parameterise and use model-integrating control methods, an in-depth physical analysis of the system states and parameters is required. To do this, it is necessary to set up a physical model with fully defined parameters of the controlled system [14].

For this purpose, a modelling method based on balance equations taking into account conservation laws is to be favoured. According to Noether's theorem, every continuous symmetry of the effect results in a conservation law, and conversely, every conservation law has a continuous symmetry of the effect. This means that the underlying physics is fundamentally captured in the model and not obscured by approximation. This results in non-linear models with parameters that can be derived entirely from physics.

However, as mentioned at the beginning, the identification of these is non-trivial due to the non-linearity and possibly time variance. The method described below, which can in principle be carried out for any type of system in any domain, sequentially describes the targeted identification of system parameters using a mechanical system.

3.1 General model description

Based on the kinematics and dynamics of the respective mechanical system to be identified, the dynamics functions must first be derived in the form of coupled, non-linear differential equations. The following equation shows the generalised dynamics model [2] derived from this:

$$\underline{\underline{M}}\left(\underline{q}\right)\cdot\ddot{\underline{q}}+\underline{\underline{C}}\left(\underline{q},\dot{\underline{q}}\right)\cdot\dot{\underline{q}}+\underline{G}\left(\underline{q}\right)=\underline{\underline{F}}\left(\underline{q}\right)\cdot\underline{u} \qquad (1)$$

The symmetric mass matrix $\underline{\underline{M}}\in\mathbb{R}^{m\times m}$ depends on the individual masses of the systems' rigid bodies and the generalised coordinates $\underline{q}\in\mathbb{R}^m$. The vector $\underline{\underline{C}}\in\mathbb{R}^{m\times m}$ describes the generalised gyroscopic forces consisting of the centrifugal and Coriolis forces. The vector $\underline{G}\in\mathbb{R}^m$ describes the potential energy via gravity. The manipulated variables entered are calculated with the time-varying vector $\underline{u}\in\mathbb{R}^n$. Its multiplication with the functional matrix $\underline{\underline{F}}\in\mathbb{R}^{m\times n}$ leads to the torque matrix.

3.2 Linearisation of the model

Characteristics of the system dynamics from equation (1) can be analysed particularly well in the frequency range. To do this, a linear model is first required at different operating points. For example, a Taylor series expansion using Jacobian matrices can be used at different time steps i. The linearised model at the current operating point is corresponding:

$$\Delta\ddot{\underline{q}}=\underbrace{\left(-\underline{\underline{J}}_{\ddot{q}}(i)^{-1}\cdot\underline{\underline{J}}_{q}(i)\right)\cdot\Delta\underline{q}+\left(-\underline{\underline{J}}_{\ddot{q}}(i)^{-1}\cdot\underline{\underline{J}}_{\dot{q}}(i)\right)\cdot\Delta\dot{\underline{q}}}_{\text{for }\underline{\underline{A}}_i\cdot\underline{x}}$$
$$+\underbrace{\left(-\underline{\underline{J}}_{\ddot{q}}(i)^{-1}\cdot\underline{\underline{J}}_{u}(i)\right)\cdot\Delta\underline{u}}_{\text{for }\underline{\underline{B}}_i\cdot\underline{u}}+\underbrace{\left(-\underline{\underline{J}}_{\ddot{q}}(i)^{-1}\right)\cdot f\Big|_{AP_i}}_{\text{for }\underline{\underline{E}}_i\cdot\underline{z}_i}$$

The result is a linear state space model according to the following equation (2).

$$\begin{aligned}\dot{\underline{x}}&=\underline{\underline{A}}_i\cdot\underline{x}+\underline{\underline{B}}_i\cdot\underline{u}+\underline{\underline{E}}_i\cdot\underline{z}_i\\ \underline{y}&=\underline{\underline{C}}\cdot\underline{x}+\underline{\underline{D}}\cdot\underline{u}\end{aligned} \qquad (2)$$

3.3 Stabilisation of the system

Based on the state space representation valid for the operating point, the system should now be stabilised by at least a narrow validity range around the operating point i using state feedback.

A feedback gain $\underline{\underline{K}}$, which forms the control vector $\underline{u}$ via the simple control law $\underline{u}^T=-\left(\underline{\underline{K}}^T\cdot\underline{x}\right)^T=-\underline{x}^T\cdot\underline{\underline{K}}^T$ through the state feedback, results from various approaches to state control and does not have to be optimally designed but must be known and constant. The system gain is normalised and the control vector is transformed using a set-point-filter $\underline{\underline{N}}$. This results in the control law of the controller:

$$\underline{u}=-\underline{\underline{K}}_i\cdot\underline{x}+\underline{\underline{N}}_i\cdot\underline{w} \qquad (3)$$

From the point of view of the setpoint input $\underline{w}$, the closed control loop now reacts like a stable multivariable system within the physical limits defined mainly by manipulated variable limits. The system limits must be checked in the same way as the BIBO stability.

This is given by a consideration of the controllability; if $\left(\underline{\underline{A}},\underline{\underline{B}}\right)$ is completely controllable, the inherent dynamics can be set arbitrarily, ergo the system can also be stabilised.

3.4 Transfer-function and decoupling of the system

The system, which has now been stabilised by control, is to be decoupled for identification in the coordinate system of the rigid body (BCS) to be investigated and the independent transfer paths are to be represented as transfer-functions.

This provides access to the main diagonal of the transfer matrix of the overall system via the transfer functions $\frac{\vartheta_x}{\vartheta_{x\_set}}$, $\frac{\vartheta_y}{\vartheta_{y\_set}}$, $\frac{\vartheta_z}{\vartheta_{z\_set}}$ in the respective spatial directions (either rotatory or translatory).

The linear equivalent state space of the system has the manipulated variables τ_1,τ_2,τ_3 of the actuators as input vector $\underline{u}(t)$, since the effect of the manipulated variables in the system model is already taken into account in relation to the BCS.

The transfer-matrix $\underline{\underline{G}}_S(s)$ of the system can be obtained from the state space representation by transforming it into the Laplace-domain.

$$\underline{\underline{G}}_S(s)=\frac{\underline{X}(s)}{\underline{U}(s)}=\left(s\cdot\mathbb{I}-\underline{\underline{A}}\right)^{-1}\cdot\underline{\underline{B}} \qquad (4)$$

This system can now be divided into the system-representation in the BCS spatial direction $\underline{\underline{G}}_{S\_R}$ and a transformation of the manipulated variables using the transformation matrix $\underline{\underline{T}}$.

In the same way, the closed control loop can be utilised by applying the control law $\underline{u} = -\underline{\underline{K}} \cdot \underline{x} + \underline{\underline{N}} \cdot \underline{w}$ onto the state space representation.

$$\begin{aligned} \dot{\underline{x}}(t) &= \underline{\underline{A}} \cdot \underline{x}(t) + \underline{\underline{B}} \cdot \left(-\underline{\underline{K}} \cdot \underline{x}(t) + \underline{\underline{N}} \cdot \underline{w}(t) \right) \\ &\circ\!\!-\!\!\bullet \\ \underline{X}(s) \cdot \left(s \cdot \mathbb{I} - \underline{\underline{A}} + \underline{\underline{B}} \cdot \underline{\underline{K}} \right) &= \underline{\underline{B}} \cdot \underline{\underline{N}} \cdot \underline{W}(s) \end{aligned} \tag{5}$$

The Transfer matrix of the closed control loop in the reference case thus becomes:

$$\underline{\underline{G}}_W(s) = \frac{\underline{X}(s)}{\underline{W}(s)} = \left(s \cdot \mathbb{I} - \underline{\underline{A}} + \underline{\underline{B}} \cdot \underline{\underline{K}} \right)^{-1} \cdot \underline{\underline{B}} \cdot \underline{\underline{N}} \tag{6}$$

The state controller and the set-point-filter also consist of a component $\underline{\underline{K}}_R$ and $\underline{\underline{N}}_R$ acting in the spatial directions and the transformation of the manipulated variables to the actuator positions by the inverse transformation matrix $\underline{\underline{T}}^{-1}$.

In the Laplace-domain, this can be expressed by the transfer-matrices $\underline{\underline{K}}(s)$ and $\underline{\underline{N}}(s)$ or $\underline{\underline{K}}_R(s) = \underline{\underline{T}} \cdot \underline{\underline{K}}(s)$ and $\underline{\underline{N}}_R(s) = \underline{\underline{T}} \cdot \underline{\underline{N}}(s)$ of the controller and set-point-filter. The controlled system can be reshaped for observation in the spatial directions [15].

3.5 Identification of the system dynamics in the frequency domain

Since the system behaviour has so far only been derived theoretically from physical modelling, the transmission behaviour of the system is now to be identified by frequency response measurements on the real plant. Because the system to be identified is unstable, the reference transfer function of the system stabilised by a linear controller is first identified and the transfer behaviour of the uncontrolled system is calculated from this. As the calculation of a frequency response is only applicable to linear systems, the model linearised at a suitable operating point is used for identification.

This model should be adapted to the measured frequency response by varying the parameters. Only as few free parameters as possible should be used. The transfer behaviour of the controller and set-point-filter is known and results from the control parameters used in the measurement. The transfer function of the actuator should first be identified separately by a frequency response measurement so that it can be assumed to be known when identifying the reference transfer function.

The actuator-transfer-matrix then corresponds to the control-transfer-matrix of the manipulated-variable-control in the BCS (X- Y- and Z-direction):

$$\underline{\underline{G}}_{M\_R}(s) = \underline{\underline{T}} \cdot \begin{bmatrix} G_{m1}(s) & 0 & 0 \\ 0 & G_{m2}(s) & 0 \\ 0 & 0 & G_{m3}(s) \end{bmatrix} \cdot \underline{\underline{T}}^{-1} \tag{7}$$

This leads to a further possibility of representing the transfer-matrix in the referencing-case with the separated transfer-functions in relation to the BCS:

$$\begin{aligned} \underline{\underline{G}}_W(s) = \left(\mathbb{I} + \underline{\underline{G}}_{S\_R}(s) \cdot \underline{\underline{G}}_{M\_R}(s) \cdot \underline{\underline{K}}_R(s) \right)^{-1} \cdot \ldots \\ \cdot \underline{\underline{G}}_{S\_R}(s) \cdot \underline{\underline{G}}_M(s) \cdot \underline{\underline{N}}_R(s) \end{aligned} \tag{8}$$

This yields to the correspondig matrix form:

$$\underline{\underline{G}}_W(s) = \begin{bmatrix} \underline{\underline{G}}_{W_{\mathrm{Rot}}}(s) & \underline{\underline{G}}_{W_{\mathrm{Trans} \mapsto \mathrm{Rot}}}(s) \\ \underline{\underline{G}}_{W_{\mathrm{Rot} \mapsto \mathrm{Trans}}}(s) & \underline{\underline{G}}_{W_{\mathrm{Trans}}}(s) \end{bmatrix} \tag{9}$$

Here, the separated transfer matrices for the reference case describe the couplings of the rotational and translational degrees of freedom in the BCS, e.g. explicitly for the rotational degrees of freedom:

$$\underline{\underline{G}}_{W_{\mathrm{Rot}}}(s) = \begin{bmatrix} \frac{\Theta_x(s)}{\Theta_{x_{\mathrm{soll}}}(s)} & \frac{\Theta_x(s)}{\Theta_{y_{\mathrm{soll}}}(s)} & \frac{\Theta_x(s)}{\Theta_{z_{\mathrm{soll}}}(s)} \\ \frac{\Theta_y(s)}{\Theta_{x_{\mathrm{soll}}}(s)} & \frac{\Theta_y(s)}{\Theta_{y_{\mathrm{soll}}}(s)} & \frac{\Theta_y(s)}{\Theta_{z_{\mathrm{soll}}}(s)} \\ \frac{\Theta_z(s)}{\Theta_{x_{\mathrm{soll}}}(s)} & \frac{\Theta_z(s)}{\Theta_{y_{\mathrm{soll}}}(s)} & \frac{\Theta_z(s)}{\Theta_{z_{\mathrm{soll}}}(s)} \end{bmatrix} \tag{10}$$

If the two reference transfer matrices are equalised, the transfer matrix of the uncontrolled system can be deduced by identifying them and subtracting the known transfer matrices of the state controller and any prefilter as well as the previously measured and transformed transfer matrix of the actuator. By equating the eq. (6) with eq. (7), it is also possible to draw conclusions about the dynamics-matrix defined at the operating point and the input-matrix of the state space and to identify individual, unknown parameters of the system within the coefficients formed by the system parameters.

3.6 Pseudo-linear identification of the stabilised system plant

Since the uncontrolled and thus also the controlled system is non-linear, the amplitude of the excitation has an influence on the system behaviour, as these do not fundamentally fulfil the amplification and superposition principle [16].

Frequency response measurements are therefore carried out with different excitation amplitudes in order to investigate this influence.

Typical non-linearities of mechanical systems are e.g. friction in the form of Coulumb or Stribeck friction, force transmission breakdown, dependencies of system states e.g. on the gravity vector/velocity vector and variable coefficients [15]. Since these effects within the frequency spectrum are dependent on both the excitation amplitude and the excitation frequency, the measurement must be carried out in partial frequency bands and then combined into one measurement using the evaluation of coherence.

Basically, the structure of the physical model is used to simulate an expected frequency response using known parameters. The simulated curve of the amplitude and phase response $(A_{\mathrm{mod}}(\omega)_{dB}, \varphi_{\mathrm{mod}}(\omega))$ is compared with the curve of the measurement graph $(A_{\mathrm{meas}}(\omega)_{dB}, \varphi_{\mathrm{meas}}(\omega))$. The difference between simulation and measurement is represented as the Root Mean Square Error ε of both the amplitude difference $\Delta A(\omega)_{dB} = A_{\mathrm{meas}}(\omega)_{dB} - A_{\mathrm{mod}}(\omega)_{dB}$ and phase difference $\Delta\varphi(\omega) = \varphi_{\mathrm{meas}}(\omega) - \varphi_{\mathrm{mod}}(\omega)$ points and is calculated using the coherence-dependent weighting factor k_{eval}.

$$\varepsilon = \varepsilon_{mag} + \varepsilon_{phase}$$

$$\varepsilon_{mag} = \frac{1}{n}\left(\sum_{\omega=\omega_{\min}}^{\omega_{\max}} (\Delta A(\omega)_{dB})^2 \cdot k_{eval}(\omega)\right)$$

$$\varepsilon_{phase} = \frac{1}{n}\left(\sum_{\omega=\omega_{\min}}^{\omega_{\max}} (20 \cdot \log(1 + |\Delta\varphi(\omega)|))^2 \cdot k_{eval}(\omega)\right)$$

The actual identification of the unknown model parameters is carried out by optimising this error surface initialised via estimates, using a modified downhill simplex algorithm according to Nelder and Mead [5].

4 Used Test Bench Infrastructure

To validate the concept described, the test bench shown in Figure 3 was set up in which the S-Mobile function carrier introduced in section can be tested under safe and reproducible conditions.

In this test rig, the S-Mobile is restrained in a reconfigurable commissioning frame, which allows either blocking or limiting the degrees of freedom of the superstructure without inhibiting the degrees of freedom of the ball.

The test carrier is fixed by wire ropes of a defined length in such a way that a tilting movement up to a maximum angle is permitted. This allows the structure to be stabilised by a translational movement of the geometric centre of the sphere while at the same time preventing it from tilting.

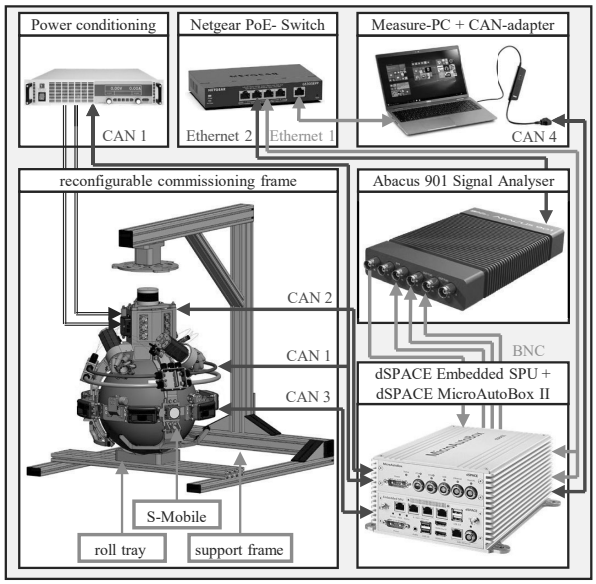

Figure 3: S-Mobile in test bench setup for identification.

The information technology linking of the measuring and control devices required for identification is also shown. The MicroAutoBox II as the RCP system of the S-Mobile is used to execute the linear stabilisation controller required for identification. The DP Abacus 901 signal analyser is coupled exclusively with this in order to specify the target variables for the stabilisation controller and to be able to calculate the delay time of the calculation duration of the control algorithm synchronously on all measurement channels.

Accordingly, all measurement signals required for identification are routed via the MicroAutoBox II. The signal measurement is not only carried out directly, but also by measurement data fusion algorithms that are mainly executed on the internally coupled embedded SPU. The actuators and sensors of the function carrier are connected via a real-time CAN network. Experiment preparation, remote ECU control and data recording are carried out on a measurement PC that communicates with both the MicroAutoBox II and the DP Abacus 901 via an Ethernet network.

5 Exemplary Application of the Method on the S-Mobile

Using the test bench presented in the previous chapter, frequency-dependent analyses were carried out on the S-Mobile function carrier. For this purpose, target states in the form of periodic excitations were given to the stabilisation controller as reference variables. The response of the closed control loop, consisting of the controller and system as well as the actuator and sensors, was then analysed.

The periodic excitations were selected on a system-specific basis in order to take specific non-linearities into account. For example, the amplitude of the excitation has an influence on the system behaviour. Frequency response measurements are therefore carried out with different excitation amplitudes in a fixed frequency range in order to investigate this influence. For excitation, amplitudes from $\hat{\vartheta}_{x\_\mathrm{set}} = 1.5^\circ$ to $\hat{\vartheta}_{x\_\mathrm{set}} = 5^\circ$ are fed in as chirp signals.

Figure 4 shows the recorded response spectra as a frequency response in the Bode diagram.

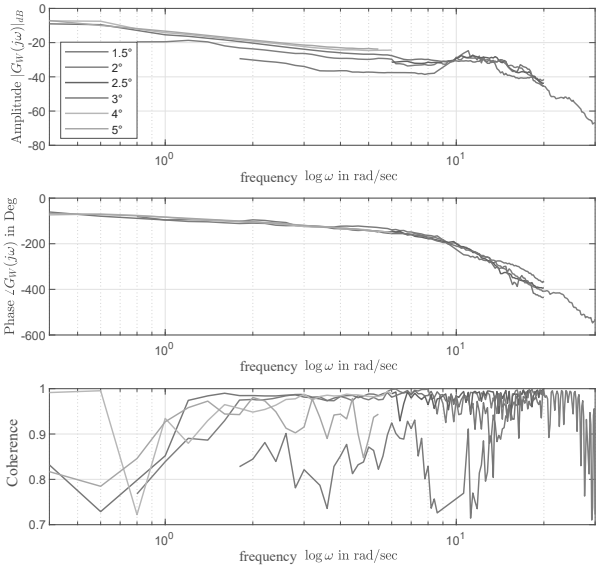

Figure 4: Measured frequency responses at different amplitude excitations, filtered by coherence.

Measurement series with a coherence of at least 0.7 across the entire spectrum have already been selected here. It can be seen that the coherence of the measurement starts to deteriorate significantly from approx. $20Hz$. This is due to the data transmission via CAN bus system from the RCP system to the actuators as well as from the sensors. The actual body angles were measured by an inertial measuring unit and transmitted via CAN with a cycle time of 10 ms. This corresponds to a sampling frequency of $100Hz$, whereby the Nyquist–Shannon sampling theorem [17] theoretically results in a maximum sampling frequency of 50Hz. In practice, however, the reconstructed signal is already distorted at lower frequencies, which results in a lower coherence of the signals. At higher amplitudes, the frequency response could only be determined for low frequencies, as excitation with a high frequency and high amplitude causes the wheels to slip due to the limited power distribution, thereby damaging the surface of the sphere.

The amplitude responses for large excitation amplitudes are close together, while the system for small excitations at low frequencies ($< 10Hz$) has a low gain and also poorer coherence. This is due to the large influence of static friction in the system at such low excitation amplitudes. The phase response, on the other hand, shows fewer deviations for all measurements.

The optimum parameters are identified by minimising the quadratic error between an assumed transfer-element as the reference-transfer-function of the separated transfer path within the transfer-matrix and the measured frequency response. Since both the transfer-function of the actuator and the transfer-functions of the controller (and set-point-filter) are known, the calculated reference model can be used to identify the structure of the transfer-element. This can also be estimated by observing the measured amplitude- and phase-drop.

To identify the parameters, the system transfer function $G_{sx}(s) = \frac{\theta_x(s)}{M_x(s)}$ must first be obtained by linearising the non-linear model with the mass moment of inertia as a free parameter. The model is to be linearised at the quasi-stable point $(\vartheta_x = 0, \vartheta_y = 0)$, as the system oscillates around this point during the frequency response measurement. However, the angular velocity is not assumed to be $\dot{\vartheta}_x = 0$ for the linearisation, but should correspond to the actual angular velocity during the measurement. However, this is not constant during the measurement, but depends on the frequency and amplitude of the oscillation. With a harmonic input oscillation $\vartheta_x(t)$ as the excitation signal, the angular velocity results from the following equation:

$$\vartheta_x(t) = A(\omega) \cdot \hat{\vartheta}_{x\_\mathrm{set}} \cdot \sin(\omega \cdot t + \varphi(\omega))$$

$$\dot{\vartheta}_x(t) = \frac{d\vartheta_x(t)}{dt} = A(\omega) \cdot \hat{\vartheta}_{x\_\mathrm{set}} \cdot \omega \cdot \cos(\omega \cdot t + \varphi(\omega))$$

For the zero crossing at the quasi-stable point around which the system oscillates ($\vartheta_x(t) = 0$), the maximum angular velocity results:

$$\dot{\vartheta}_x(\omega) = A(\omega) \cdot \hat{\vartheta}_{x\_\text{set}} \cdot \omega \tag{11}$$

The following figure 5 shows the maximum angular velocities associated with the measured frequency response.

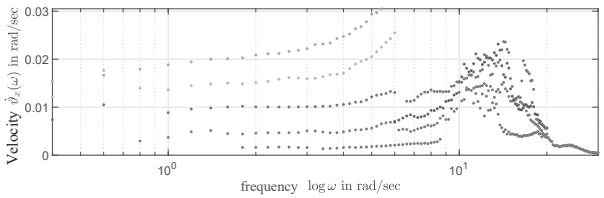

Figure 5: Angular velocity at zero crossing.

These are used for the linearisation of the reference model in order to derive the transfer-matrix using the method described in chapter 3. This in turn shows the structure and the parameter dependency, which can now be resolved according to an unknown parameter. By linearising the non-linear model at the operating point under consideration, for example, a system transfer function dependent on the moment of inertia θ_x can be derived in order to identify this as a free parameter via quadratic optimisation:

$$G_{sx}(s) = \frac{\vartheta_x(s)}{\tau_x(s)} = f(\sigma, \omega, \theta) \tag{12}$$

In combination with the known/identified actuator (-system) and the transfer-functions of the controller, the reference-transfer-function for the examined degree of freedom can be formed. The transfer-function of the state-feedback always results as a PDn-element, since the state controller always feeds back all minimum coordinates and at least their first derivative [18]. Furthermore, a dead time T_t is added to the transfer-element, which results from the data communication process.

$$G_w(s) = \frac{\vartheta_x(s)}{\vartheta_{x\_\text{set}}(s)} = \frac{N_{Rx} \cdot G_{sx}(s) \cdot G_m(s)}{1 + G_{sx}(s) \cdot G_m(s) \cdot K_{Rx}(s)} \cdot e^{-T_t \cdot s}$$

The frequency response of the applied transfer element with free initialised parameters is shown in green in the following figure 6. Quadratic optimisation results in the red curve after parameter adjustment. By minimising the error of the amplitude- and phase-response in relation to the measurement, unknown values for the free parameters of the example system were identified. A comparison with the design data of the system confirms the accuracy of the identified mass moment of inertia $\theta_x = 20.31$. This method can therefore be used to identify unknown parameters on under-actuated, unstable and non-linear systems.

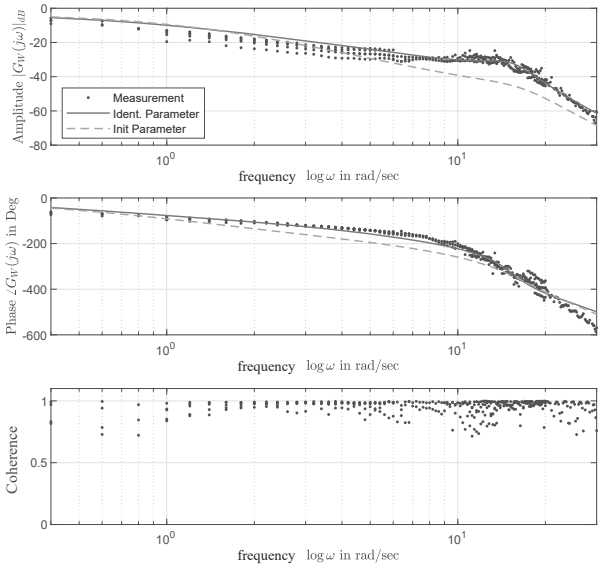

Figure 6: Identified transfer element for the command case.

6 Conclusions and Future Work

This paper discussed the identification and control of unstable, under-actuated systems with non-linear dynamic behaviour. The focus was on the development and validation of a new methodological procedure for system identification. Using the example of the S-Mobile, an innovative intralogistics system, it was successfully demonstrated how the system dynamics can be precisely identified and the system stabilised by applying the new approach.

For future work, further investigation of the approach is recommended in order to cover an even wider range of unstable, under-actuated systems. In particular, the integration of advanced machine learning methods and surrogate models [19] could further improve the accuracy and increase the adaptivity of the control systems. It would also be of great interest to investigate the transferability of the developed methods to other industrial applications to test their universal applicability.

Acknowledgement

This contribution was funded by the Lower Saxony Ministry of Science and Culture under grant number ZN3495 within the Lower Saxony "Vorab" of Volkswagen Foundation and supported by the Center for Digital Innovations (ZDIN).

Publication Remark

This contribution is the revised English version of the (German) conference version published in
Tagungsband Langbeiträge ASIM SST 2024,
ARGESIM Report AR 47,
ISBN ebook: 978-3-903347-65-6,
volume DOI 10.11128/arep.47,
article DOI 10.11128/arep.47.a4723, p 175-183.

References

[1] Schoukens J, Ljung L. Nonlinear System Identification: A User-Oriented Road Map. *IEEE Control Systems*. 2019;39(6):28–99.

[2] Liu-Henke X, Göllner M, Tao H. An intelligent control structure for highly dynamic driving of a spherical electrical drive. In: *2017 Twelfth International Conference on Ecological Vehicles and Renewable Energies (EVER)*. Piscataway, NJ: IEEE. 2017; pp. 1–10.

[3] Liu-Henke X, Jacobitz S, Göllner M, Scherler S, Yarom OA, Zhang J. A Holistic Methodology for Model-based Design of Mechatronic Systems in Digitized and Connected System Environments. In: *ICSOFT 2021*. [Setúbal, Portugal]: SCITEPRESS - Science and Technology Publications. 2021;.

[4] Gevers M. Identification for Control: From the Early Achievements to the Revival of Experiment Design*. *European Journal of Control*. 2005;11(4-5):335–352.

[5] Isermann R, Münchhof M. *Identification of Dynamic Systems*. Berlin, Heidelberg: Springer Berlin Heidelberg. 2011.

[6] Ljung L. Frequency Domain Versus Time Domain Methods in System Identification – Revisited. In: *Control of uncertain systems: modelling, approximation, and design*, edited by Francis BA, vol. 329 of *Lecture notes in control and information sciences*, pp. 277–291. Berlin and Heidelberg: Springer. 2006;.

[7] Pintelon R, Schoukens J. *System Identification: A Frequency Domain Approach*. Wiley. 2012.

[8] Nelles O. *Nonlinear System Identification: From Classical Approaches to Neural Networks, Fuzzy Models, and Gaussian Processes*. Cham: Springer International Publishing, 2nd ed. 2020.

[9] van den Hof P. Closed-loop issues in system identification. *Annual Reviews in Control*. 1998; 22:173–186.

[10] Xavier J, Patnaik SK, Panda RC. Process Modeling, Identification Methods, and Control Schemes for Nonlinear Physical Systems – A Comprehensive Review. *ChemBioEng Reviews*. 2021;8(4):392–412.

[11] Chawla I, Singla A. ANFIS based system identification of underactuated systems. *International Journal of Nonlinear Sciences and Numerical Simulation*. 2020;21(7-8):649–660.

[12] Chen R, Srivastava A, Yin M, Smith RS. Closed-Loop Identification of Stabilized Models Using Dual Input-Output Parameterization.

[13] González RA, Rojas CR, Pan S, Welsh JS. Refined instrumental variable methods for unstable continuous-time systems in closed-loop. *International Journal of Control*. 2023;96(10):2527–2541.

[14] Isermann R. *Mechatronische Systeme*. Berlin, Heidelberg: Springer Berlin Heidelberg. 2008.

[15] Göllner M, Liu-Henke X, Frerichs L. Analyse und Simulation des Kraftübertragungsverhaltens von Mecanum-Rädern. In: *Proceedings ASIM SST 2020*, edited by Deatcu C, Lückerath D, Ullrich O, Durak U, ASIM Mitteilung, pp. 89–98. Wien: ARGESIM Verlag. 2020;.

[16] Wittenburg J. *Dynamics of multibody systems*. Berlin and New York: Springer, 2nd ed. 2008.

[17] Seibt P. *Algorithmic Information Theory: Mathematics of Digital Information Processing*. Signals and communication technology. s.l.: Springer-Verlag, 1st ed. 2006.

[18] Karrenberg U. *Signale – Prozesse – Systeme*. Berlin, Heidelberg: Springer Berlin Heidelberg. 2017.

[19] Göllner M, Yarom OA, Fritz J, Liu-Henke X. Rechenzeitoptimierte Modellierung nicht-linearer physikalischer Prozesse mit Surrogate Modellen zur Anwendung in echtzeitfähigen Optimierungsverfahren. In: *Virtueller ASIM Workshop 2021*, edited by Liu-Henke X, Durak U, ASIM Mitteilung. Vienna: ARGESIM Verlag. 2021;.

EXCEL as Simulation Tool for ARGESIM Benchmark C21 'State Events and Structural Dynamic Systems', Case Study RLC with Diode

Clemens Karner, Michael Farthofer, Ludwig Fellinger, Gebhard Fellinger, Felix Breitenecker*

[1]Institute of Analysis and Scientific Computing, TU Wien, Wiedner Hauptstrasse 8-10, 1040 Vienna, Austria
felix.breitenecker@tuwien.ac.at

SNE 35(3), 2025, 159-170, DOI: 10.11128/sne.35.ebn21.10746
Received: 2023-11-23; Improved: 2024-08-15
Revised: 2025-06-01; Accepted: 2025-07-01
SNE - Simulation Notes Europe, ARGESIM Publisher Vienna
ISSN Print 2305-9974, Online 2306-0271, www.sne-journal.org

Abstract. Very often EXCEL is called the most-used simulator – but also for continuous ODE systems? Generally, EXCEL allows easy implementation of recursive formula, as for the EULER solver (there exist also ODE solver macros for EXCEL). This student project reports on experiences with a basic recursive EULER solver for ARGESIM Benchmark C21, case study 'RLC with Diode, and documents also the model set up for educational purposes.
For the event handling of diode switching, two previous steps of the solver had to be observed – with reasonable results. Some problems occurred with the numerical treatment of the formula, because of the big range of parameters, leading to numerical extinction errors, especially in case of the Shockley formula interpolation.
For the reasonable results, a very fine grid had to be used – an EXCEL table with 40.000 rows (and some for initialisation. The answer: EXCEL can also be used for continuous systems with events, but cannot be really recommended.

Introduction – Basic Modelling

ARGESIM Benchmark C21 ''State Events and Structural Dynamic Systems', Case Study RLC with Diode is based on the dynamics of a simple RLC circuit with a diode in parallel (Figure 1).

The RLC circuit is made up from idealized parts, with exception of the diode: an alternating voltage source U_0, two resistors R_1, R_1, an inductor L and a capacitor C, all with continuous description between voltage and current.

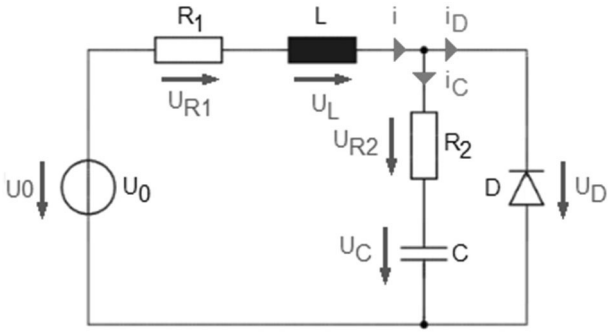

Figure 1: RLC Circuit with diode in parallel, counting direction for currents and voltages.

The basic dynamics are given by the active elements, by inductor L and a capacitor C:

$$\frac{di_L}{dt} = \frac{1}{L}u_L \qquad \frac{du_C}{dt} = \frac{1}{C}i_C$$

So generally, two coupled differential equations have to be solved. A basic solution approach is the Euler ODE solver with an appropriate stepsize $\Delta t = t_{n+1} - t_n$:

$$i_{L,n+1} = i_{L,n} + \Delta t \cdot \frac{1}{L}u_{L,n} = \Delta t \cdot f_n\left(i_{L,n}, u_{C,n}\right)$$

$$u_{C,n+1} = u_{C,n} + \Delta t \cdot \frac{1}{C}i_{c,n} = \Delta t \cdot g_n\left(i_{L,n}, u_{C,n}\right)$$

EXCEL allows to implement these recursive formulas easily step by step in consecutive rows (Table 1).

0	t_0	$i_{L,0}$	$u_{C,0}$
...	...	...	...
n-1	t_{n-1}	$i_{L,n-1} = \cdots$	$u_{C,n-1} = \cdots$
n	t_n	$i_{L,n} = i_{L,n-1} + \Delta t \cdot f_{n-1}$	$u_{C,n} = u_{C,n-1} + \Delta t \cdot g_{n-1}$
n+1	t_{n+1}	$i_{L,n+1} = i_{L,n} + \Delta t \cdot f_n(i_{L,n}, u_{C,n})$	$u_{C,n+1} = u_{C,n} + \Delta t \cdot g_n(i_{L,n}, u_{C,n})$
...	...	...	...

Table 1: Euler solver steps in EXCEL.

For the diode, the benchmark suggests three different model approaches: an ideal diode, a diode with Shockley dynamics, and a diode with interpolated/approximates Shockley dynamics. Generally, the diode action – conducting or locking changes the 'update'-equations f_n and g_n, requiring IF – THEN - ELSE constructs in the EXCEL implementation.

1 RLC Model – Ideal Diode

The characteristic behaviour of an ideal diode can be described by a discontinuous function consisting of two parts. One part is for the locking phase; the other is for the conducting phase of the diode.

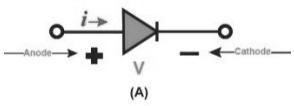

Figure 2: Electrical symbol of a diode (detailed)

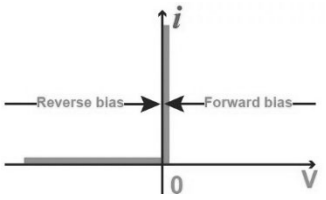

Figure 3: Characteristics of an ideal diode.

The mathematical description for the ideal diode is given by switching between locking phase $u_D > 0$ and conduction phase $u_D \leq 0$:

$$i(u_D) = \begin{cases} 0, u_D > 0 \\ i(t), u_D \leq 0 \end{cases}$$

1.1 RLC Circuit - ideal diode in locking phase

In locking phase, the ideal diode is reverse biased and therefore no current i_D can pass. Figure 4 shows the circuit with directions for current (green circles).

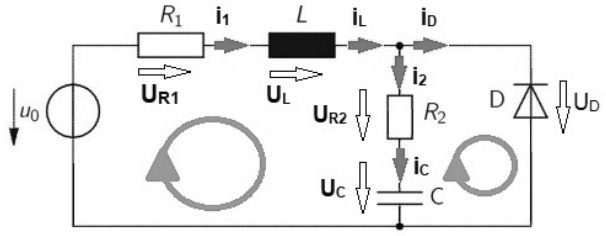

Figure 4: RLC circuit in locking phase.

Applying Kirchhoff's mesh rule (green circles) gives:

$$0 = -U_0 + u_{R1} + u_L + u_{R2} + u_C$$

$$0 = u_D - u_{R2} - u_C$$

Kirchhoff's junction rule in case of $i_D = 0$ ends up in the following identities:

$$i_1 = i_L = i_2 = i_C$$

Using now the dynamic equations for inductor L and capacitor C, and Ohm's law for the resistances R_1 and $R2$

$$\frac{di_L}{dt} = \frac{1}{L}u_L \qquad \frac{du_C}{dt} = \frac{1}{C}i_C$$

$$U_{R1} = i_1 \cdot R_1, \qquad U_{R2} = i_2 \cdot R_2$$

allows to rearrange the equations for the voltages

$$u_L = U_0 - u_{R1} - u_{R2} - u_C$$

$$u_L = U_0 - i_1 \cdot (R_1 - R_2) - u_C$$

and with substitution of U_L by u_1 to derive the full dynamic description of the system:

$$\frac{di_1}{dt} = \frac{1}{L} \cdot (U_0 - i_1 \cdot (R_1 - R_2) - u_C)$$

$$\frac{du_C}{dt} = \frac{1}{C}i_1$$

$$u_D = i_1 \cdot R_2 + u_C,\ u_D > 0$$

It is to be noted, that the diode voltage u_D does not appear in the state equations for i_1 and u_c, but the equation for u_D controls the locking phase $u_D > 0$

The Euler ODE solver can be applied now to the state equations for i_1 and u_c at an equidistant grid

$$t_0 < t_1 < t_2 \ldots < t_{n-1} < t_n < t_{n+1} \ldots < t_{end-1} < t_{end}$$

with stepsize $\Delta t = t_{n+1} - t_n$:

$$i_{1_{n+1}} = i_{1_n} + \Delta t \cdot \left(\frac{1}{L} \cdot (U_{0_n} - i_{1_n} \cdot (R_1 - R_2) - u_{C_n})\right)$$

$$u_{C_{n+1}} = u_{C_n} + \Delta t \cdot \left(\frac{1}{C} \cdot i_{1_n}\right)$$

$$u_{D_n} = i_{1_n} \cdot R_2 + u_{C_n},\ u_D > 0$$

$$u_{D_{n+1}} = i_{1_{n+1}} \cdot R_2 + u_{C_{n+1}},\ u_D > 0$$

This set of recursive equations is suitable for implementation in EXCEL. Additionally to the state update from t_n to t_{n+1}, the relation for u_{D_n}or $u_{D_{n+1}}$ resp., must be checked for positivity.

In case of negativity of $u_{D_{n+1}}$ to next step takes place in the conduction phase. The exact time instant t_{change} of phase change lies between t_n and t_{n+1} and is roughly approximated by the next update step.

1.2 Circuit - ideal diode in conducting phase

In conducting phase, the ideal diode is forward biased and therefore current i_D can pass. Due to this fact the ideal diode behaves like an ideal conductor in conducting phase and the voltage u_D will be zero.

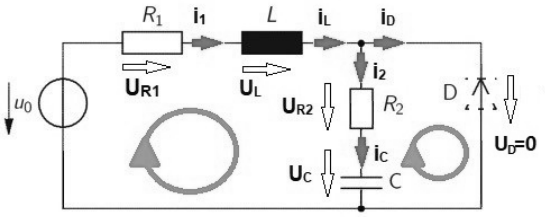

Figure 5: RLC circuit in conducting phase.

Applying Kirchhoff's mesh rule (green circles) again gives:

$$0 = -U_0 + u_{R1} + u_L + u_{R2} + u_C$$

$$0 = u_D - u_{R2} - u_C$$

But Kirchhoff's junction rule in conducting phase with $i_D \neq 0$ now gives:

$$0 = i_L - i_2 - i_D \quad 0 = i_1 - i_L \quad 0 = i_2 - i_C$$

Using now as before the dynamic equations for inductor L and capacitor *C*, and Ohm's law for the resistances R_1 and *R*2 allows to rearrange the equations for the voltages with different result:

$$u_L = U_0 - u_{R1} - u_{R2} - u_C$$

$$u_L = U_0 - i_1 \cdot R_1 - u_D$$

In the conducting phase the ideal diode is a perfect conductor and no voltage drop will appear

$$u_L = U_0 - i_1 \cdot R_1$$

so that with substitution of i_L by i_1 the full dynamic description in conducting phase becomes

$$\frac{di_1}{dt} = \frac{1}{L} \cdot (U_0 - i_1 \cdot R_1)$$

$$\frac{du_C}{dt} = -\frac{1}{C \cdot R_2} \cdot u_C$$

$$i_D = i_1 + \frac{1}{R_2} \cdot u_C$$

Nevertheless, U_D is zero in conduction phase we have to recognize phase changes by calculating U_D also in this phase:

$$u_D = (i_1 - i_D) \cdot R_2 + u_C$$

As before, the Euler ODE solver can be applied now to the state equations for i_1 and u_c at an equidistant grid

$$t_0 < t_1 < t_2 \ldots < t_{n-1} < t_n < t_{n+1} \ldots < t_{end-1} < t_{end}$$

with stepsize $\Delta t = t_{n+1} - t_n$:

$$i_{1_{n+1}} = i_{1_n} + \Delta t \cdot \left(\frac{1}{L} \cdot \left(U_{0_n} - i_{1_n} \cdot R_2\right)\right)$$

$$\mathrm{F}u_{C_{n+1}} = u_{C_n} + \Delta t \cdot \left(-\frac{1}{C \cdot R_2} \cdot u_{C_n}\right)$$

$$i_{D_n} = i_{1_n} + \frac{1}{R_2} \cdot u_{C_n}, i_{D_{n+1}} = i_{1_{n+1}} + \frac{1}{R_2} \cdot u_{C_{n+1}}$$

$$u_{D_n} = \left(i_{1_n} - i_{D_n}\right) \cdot R_2 + u_{C_n}$$

$$u_{D_{n+1}} = \left(i_{1_{n+1}} - i_{D_{n+1}}\right) \cdot R_2 + u_{C_{n+1}}$$

If the diode voltage becomes nonzero, $u_{D_{n+1}} \neq 0$, the next step takes place in the locking phase. The exact time instant t_{change} of phase change lies between t_n and t_{n+1} and is roughly approximated by the next update step.

1.3 Phase change Locking - Conducting

The diode voltage u_D is the decisive factor which implies whether the diode is in locking phase or conducting phase. The sign change or the change to zero of u_D are so-called state events, unknown in time, which decide that in each phase (locking or conducting) a different set of equations are used for the calculation of the voltage and current in the circuit.

To recognize the state event *start of the conducting phase* (SCP), the diode voltage u_D in the locking phase must be observed. When the diode voltage u_D in the locking phase sinks below zero and changes its sign, the state event *start of conducting phase* is triggered. From now on the diode is in conducting phase and different equations including the equation for calculating u_D itself must be used. This can be expressed by a so-called state event determination equation

$$\overset{!\,-}{u_D} = i_1 \cdot R_2 + u_C \qquad \text{SCP}$$

determining the time instant t_{SCP}, where SCP takes place, i.e. where the equation has a zero (from plus to minus):

$$U_D(t_{SCP}) = i_1(t_{SCP}) \cdot R_2 + u_C(t_{SCP}) = 0$$

Obviously, more SCP events occur, with event times $t_{SCP,k}$, alternatingly with SLP events at $t_{SLP,j}$.

And similarly, to recognize the state event *start of the locking phase* (SLP) the diode voltage u_D in the conducting phase must be observed. When the diode voltage u_D of the conducting phase changes its sign from negative to positive the state event *start of the locking phase* is triggered. From now on the set of equations for the locking phase must be used.

This can also be expressed by a state event determination equation

$$u_D = (i_1 - i_D) \cdot R_2 + u_C \quad \begin{matrix} ! + \\ \text{SLP} \end{matrix}$$

determining the time instant t_{SLP}, where SCP takes place, i.e. where the equation has a zero (from minus to plus):

$$u_D(t_{SCP}) = \big(i_1(t_{SlP}) - i_D(t_{SlP})\big) \cdot R_2 + u_C(t_{SlP}) = 0$$

And again obviously, more SLP events occur, with event times $t_{SLP,j}$, alternatingly with SCP events at $t_{SCP,k}$.

During time solution in the locking phase and in the conducting phase, the state events SCP and SLP must be found. They take place between neighbouring steps of the ODE solver,

$$t_i \le t_{SLP} \le t_{i+1}, \text{ or } t_m \le t_{SCP} \le t_{m+1} \text{ resp.}$$

Some simulation systems provide algorithms for finding these event times iteratively.

In EXCEL, we have fixed time steps, so one can simply approximate the event time with the next step time, where it is detected, i.e. the event SCP or SLP takes place between t_i and t_{i+1}, the event time is fixed with

$$t_{SLP} = t_{i+1} \text{ . or } t_{SCP} = t_{m+1}.$$

But unfortunately, using the sign change of the diode voltage u_D as an indicator of phase change works only in theory also here. In this case study, the sign change is more complex. Due to the fact that in conducting phase the ideal diode behaves like a perfect conductor the diode voltage u_D equals zero in conducting phase. So, the above mechanism for phase change can only be used from locking phase to conducting phase.

From conducting phase to locking phase, the classical mechanism fails. it's not possible to apply these definitions, because there is only a transition from u_D is zero to u_D is positive – one has to observe in this case not only one time step t_i and t_{i+1}, but two time steps t_{i-1}, t_i and t_{i+1}, to determine SLP with $t_{SLP} = t_{i+1}$ properly.

1.4 EXCEL implementation – ideal diode model

In the following, the overall structure of the developed spreadsheet and the ODE solve update with event detection is described.

At the top of the spreadsheet circuit parameters (electrical characteristics), initial conditions and simulation parameters (e.g. time step) are initialized (Table 2).

The benchmark definition and the characteristics of the input voltage U_0 (high frequency excitation) suggest a simulation horizon of $5 \cdot 10^{-4}$ sec, so we decided for a time step $\Delta t = 1.25 \cdot 10^{-8}$ sec, resulting in indeed 40000 EXCEL rows. This fine resolution would not be necessary for the Euler solver, but for approximating the phase change time instants it was appropriate. A finer resolution would make problems with numerics (extinction error).

	A	B	C	D	E
1					
2					
3	Parameter			Simulationsparameter	
4	R1 [ohm]	1000		Zeilenzahl [1]	40000
5	R2 [ohm]	20		Simulationsdauer [s]	0,0005
6	L [H]	2,52E-05		dt [s]	1,25E-08
7	C [F]	1,00E-07		t0 [s]	0
8	Is [A]	1,00E-08			
9	Ut [V]	0,026			
10	f [Hz]	142857			
11					
12					
13					
14	Initial Conditions				
15	i1_0 [A]	0			
16	Uc_0 [V]	0			
17					
18					
19					
20					
21					
22					
23	Start with Locking Phase				
24					
25	t	U0	i1	Uc	Ud	Id
26	0	0	0	0	0,00E+00	
27	1,25E-08	0,01121973	0,00E+00	0,00E+00	0,00E+00	
28	0,000000025	0,02243804	5,57E-06	0,00E+00	1,11E-04	
29	3,75E-08	0,03365353	1,39E-05	6,96E-07	2,78E-04	
30	0,00000005	0,04486479	2,36E-05	2,43E-06	4,73E-04	
31	6,25E-08	0,05607039	3,39E-05	5,37E-06	6,83E-04	

Table 2: Overall structure of EXCEL implementation for ideal diode circuit.

Below the parameter definitions of the spreadsheet, the columns for time t , the excitation voltage U_0 , the current through inductor i_1, the voltage in capacitor u_C, the voltage drop in diode u_D and the current through diode i_D start (Table 3). The EXCEL setup of the recursive equations for the EULER solver follows the principle given in Table 1.

	A	B	C	D	E	F
22						
23	Start with Locking Phase					
24						
25	t	U0	i1	Uc	Ud	Id
26	0	0	0	0	0,00E+00	0
27	1,25E-08	0,0112197	0,00E+00	0,00E+00	0,00E+00	0
28	0,000000025	0,022438	5,57E-06	0,00E+00	1,11E-04	0
29	3,75E-08	0,0336535	1,39E-05	6,96E-07	2,78E-04	0
30	0,00000005	0,0448648	2,36E-05	2,43E-06	4,73E-04	0
31	6,25E-08	0,0560704	3,39E-05	5,37E-06	6,83E-04	0
32	0,000000075	0,0672689	4,46E-05	9,61E-06	9,01E-04	0
33	8,75E-08	0,078459	5,54E-05	1,52E-05	1,12E-03	0
34	0,0000001	0,0896392	6,63E-05	2,21E-05	1,35E-03	0
35	1,125E-07	0,1008081	7,72E-05	3,04E-05	1,57E-03	0
36	0,000000125	0,1119644	8,81E-05	4,00E-05	1,80E-03	0
37	1,375E-07	0,1231065	9,91E-05	5,10E-05	2,03E-03	0
38	0,00000015	0,1342331	1,10E-04	6,34E-05	2,26E-03	0

Table 3: Start of spreadsheet simulation.

In the first ten rows of the EXCEL simulation we assumed to be in locking phase and used the equations of the locking phase. No case distinctions between the phases have been made in these rows. It can be compared with a booting up of the simulation. This approach is necessary because of the recursive case distinction which needs the data of the rows before.

So e.g. the state update in row 30 (i.e. at t_5) for $i_{1,5}$ and $u_{C,5}$ are in pseudo-EXCEL notation:

```
C30=C29+dt*(1/L*(B29-C29*(R1+R2)-D29))

D30=D29+dt*(1/C*C29)
```

After this 'booting' for the solver update in the cells for i_1, u_C , u_D and i_D – i.e. in columns C, D, E and F – it is necessary to make use of if-then-else formula for calculating the values in a cell.

To determine the values in these columns, the information from three timesteps is needed for update to t_k , from t_{k-2} and t_{k-1} for current and voltage and from t_k for time and voltage input.

In cell C37, the current through inductor at timestep t_k is calculated. To update the current i_1 either the recursive formula in locking phase or the recursive formula in conducting phase must be applied. For the distinction between these two formulas the occurrence of phase change must be checked.

This is done by observing the diode voltage U_D of two timesteps before (t_{k-2} and t_{k-1}). If both are greater than zero (AND condition $u_D(t_{k-2}) > 0$ & $u_D(t_{k-2})$), the value for i_1 is calculated with equation of the locking phase. Otherwise, the equation of the conducting phase is used (Table 4, upper part).

	A	B	C	D	E	F	G	H	I	J
25	t	U0	i1	Uc	Ud	Id				
35	1,125E-07	0,1008081	7,72E-05	3,04E-05	1,57E-03	0				
36	0,000000125	0,1119644	8,81E-05	4,00E-05	1,80E-03	0				
37	1,375E-07	0,1231065	=WENN(UND(E35>0;E36>0);C36+1/$B$6*(B36-C36*($B$4+$B$5)-D36)*$E$6;C36+1/$B$6*(B36-C36*$B$4)*$E$6)							
38	0,00000015	0,1342331	1,10E-04	6,34E-05	2,26E-03	0				
39	1,625E-07	0,1453429	1,21E-04	7,72E-05	2,49E-03	0				

	A	B	C	D	E	F	G	H	I
25	t	U0	i1	Uc	Ud	Id			
34	0,0000001	0,0896392	6,63E-05	2,21E-05	1,35E-03	0			
35	1,125E-07	0,1008081	7,72E-05	3,04E-05	1,57E-03	0			
36	0,000000125	0,1119644	8,81E-05	4,00E-05	1,80E-03	0			
37	1,375E-07	0,1231065	9,91E-05	=WENN(UND(E35>0;E36>0);D36+1/$B$7*C36*$E$6;D36+1/($B$7*$B$5)*(-D36)*$E$6)					
38	0,00000015	0,1342331	1,10E-04	WENN(Wahrheitstest; [Wert_wenn_wahr]; [Wert_wenn_falsch])		0			
39	1,625E-07	0,1453429	1,21E-04	7,72E-05	2,49E-03	0			

Table 4: Conditional computation of current and voltage depending on phase, ideal diode model.

The capacitor voltage u_C is calculated in cell D37. Similar to calculation of i_1 also here a case distinction between locking and conducting phase must be made. The case distinction is also based recursively on the values of $u_D(t_{k-2})$ and $u_D(t_{k-2})$, see Table 4, lower part.

In the general consideration wrt. phase change before, only one previous step was necessary. But here two steps must be used, because of determining the direction of change and taking into account that the diode voltage does not cross zero, it is positive or zero.

1.5 EXCEL simulation – results ideal diode model

The results for capacitor voltage u_C , diode voltage u_D and diode current i_D show the expected behaviour (Figure 6). It is obvious, that the 'ideal' diode is a simplified idealized diode. While the time course for capacitor voltage u_C seems reasonable, the time course for diode voltage u_D shows a jump (not possible reality), and the diode current i_D passes through in locking phase with a 'spike'.

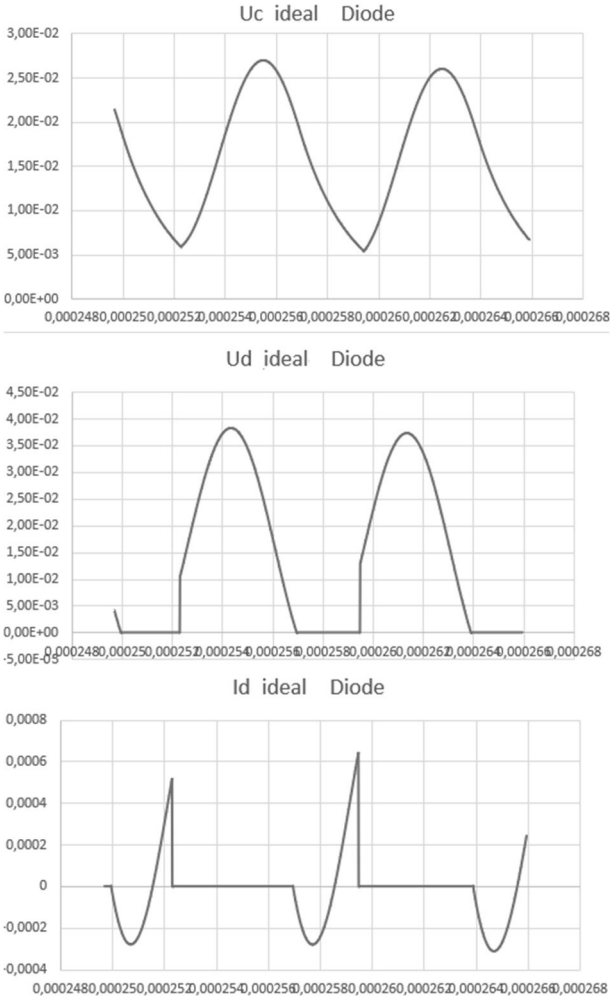

Figure 6: EXCEL simulation results for ideal diode model.

2 RLC Model – Interpolated Shockley Diode

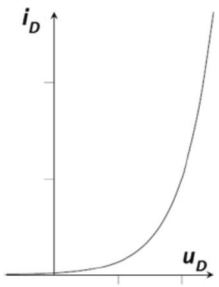

Figure 7: Shockley diode.

A Shockley diode acts similarly to an ideal diode, but smoothens the phase change, and is much nearer to reality. Basically, it is perfect insulator. When the applied voltage changes its sign and the Shockley diode is forward biased the behaviour is different to an ideal diode.

There is an exponential link between diode current and applied voltage (Figure 7).

The relation between current i_D and voltage u_D in a Shockley diode follows now a continuous function:

$$i(u_D) = \begin{cases} I_S * (e^{\frac{u_D}{U_T}} - 1), u_D \geq 0 \\ 0, u_D < 0 \end{cases}$$

In the conducting phase, there is an exponential-shaped (nonlinear) relation between diode voltage and diode current, which cannot be resolved directly. Generally, this relation adds an algebraic equation to the differential equations for capacity voltage and inductivity current, so that the system becomes a differential-algebraic equations – to be discussed in the next chapter.

2.1 Model with interpolated Shockley diode

The suggestion in this benchmark is, to approximate the nonlinear characteristics of the Shockley diode model by a table function, in this solution by three breakpoints, i.e.by two linear functions.

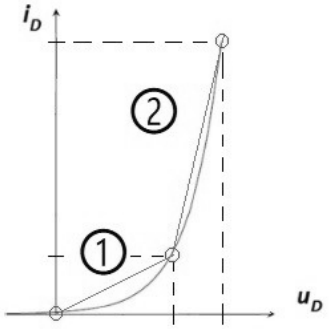

Figure 8: Shockley diode characteristics with approximation by linear functions.

In this approach the nonlinear current - voltage relation of the Shockley diode is approximated with linear functions. The diode voltage of the forward biased diode is split up in two parts. The first part ① extends between zero and 0,33 [V] and the second part ② extends between 0,33 [V] and 1 [V] (see Figure 8):

$$u_D = k_{low} \cdot I_d \qquad 0 \le u_D \le 0{,}33$$

$$u_D = k_{high} \cdot I_d + d \qquad 0{,}33 < u_D \le 1$$

The model description with interpolated Shockley diode for the locking phase is the same as the model description with the ideal diode.

For the conducting phase with the interpolated Shockley diode, now the equations change. Following again Figure 5 (RLC circuit with conducting phase of diode) we end up with the following differential equations for capacitor voltage u_C and inductor current i_1:

$$\frac{di_1}{dt} = \frac{1}{L} \cdot (U_0 - i_1 \cdot (R_1 + R_2) + i_D \cdot R_2 - u_C)$$

$$\frac{du_C}{dt} = \frac{1}{C} \cdot (i_1 - i_D)$$

In these equations now the diode current appears, which is to be expressed and substituted by other voltages or currents resp.

Kirchhoff's mesh rule or junction rule, resp. gives the relations

$$0 = -u_C - i_2 \cdot R_2 + u_D$$

$$0 = -u_C - (i_1 - i_D) \cdot R_2 + u_D$$

Now we can use the linear relations of the interpolated Shockley characteristics $u_D = k_{low} \cdot I_d$ (region ①) or $u_D = k_{high} \cdot I_d + d$ (region ②):

$$i_D = \frac{(u_C + i_1 \cdot R_2)}{(R_2 + k_{low})} \qquad 0 \le u_D \le 0{,}33$$

$$i_D = \frac{(u_C + i_1 \cdot R_2 - d)}{(R_2 + k_{high})} \qquad 0{,}33 < u_D \le 1$$

Inserting now the linear equations for the diode current i_D into the ODEs result for case ① in

$$\frac{di_1}{dt} = \frac{1}{L} \cdot (U_0 - i_1 \cdot (R_1 + R_2) + \frac{(u_C + i_1 \cdot R_2)}{(R_2 + k_{low})} \cdot R_2 - u_C)$$

$$\frac{du_C}{dt} = \frac{1}{C} \cdot (i_1 - \frac{(u_C + i_1 \cdot R_2)}{(R_2 + k_{low})})$$

and for case ② in:

$$\frac{di_1}{dt} = \frac{1}{L} \cdot (U_0 - i_1 \cdot (R_1 + R_2) + \frac{(u_C + i_1 \cdot R_2 - d)}{(R_2 + k_{high})} \cdot R_2 - u_C)$$

$$\frac{du_C}{dt} = \frac{1}{C} \cdot (i_1 - \frac{(u_C + i_1 \cdot R_2 - d)}{(R_2 + k_{high})})$$

Now the Euler solver has to be applied, which e.g. for the voltage equation in case ② gives

$$u_{C_{n+1}} = u_{C_n} + \frac{\Delta t}{C} \cdot \left[i_{1_n} - \left(\frac{(u_{C_n} + i_{1_n} * R_2 - d)}{(R_2 + b)} \right) \right]$$

2.2 Phase change Locking - Conducting

The event handling with the interpolated Shockley diode is similar to the event handling with the ideal diode. In the locking phase the diode voltage u_D corresponds to the state event condition function of the conduction phase. In analogy, the diode voltage u_D in conduction phase is the state event condition function for the locking phase.

The interpolated Shockley diode simplifies the state event recognition, because there is also a voltage drop along the diode when it is forward biased. But in the conducting phase, there are two different sets of equations for calculating i_1, u_C, i_D and u_D depending on the value of the u_D in the former timestep.

The start of conduction phase (SCP) is triggered by the value of u_D in the locking phase. A transition of the value of u_D from positive to a negative number indicates the conducting phase start:

$$u_D \overset{!-}{=} i_1 * R_2 + u_C$$

The start of the locking phase (SLP) is triggered by the value of u_D in the conducting phase. A transition of the value of u_D from negative to a positive number indicates the locking phase start:

$$U_D \overset{!+}{=} \begin{cases} k_{low} \cdot I_d & 0 \le u_D \le -0{,}33 \\ k_{high} \cdot I_d + d & 0{,}33 < u_D \le 1 \end{cases}$$

So, the change of the linear relation for the diode current is an additional event, which should be treated properly.

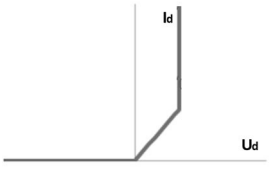

Figure 9: 'Real size' of diode characteristics.

It must be mentioned, that with the diode data given, the exponential function has a very big slope, as well as the linear functions (Figure 9). So also alternatives are possible, e.g. linearisation (see Section 2.5)

	A	B	C	D	E	F	G	H
25	t	U0	i1	Uc	Ud	Id		
35	1,125E-07	0,10080814	7,7192E-05	3,04E-05	1,57E-03	0		
36	0,000000125	0,11196436	8,8126E-05	4,00E-05	1,80E-03	0		
37	1,375E-07	0,1231065	=WENN(UND(E35>0;E36>0);C36+1/$B$6*(B36-C36*($B$4+$B$5)-D36)*$E$6;WENN(E36>=-0,					
38	0,00000015	0,13423313	333;C36+1/$B$6*(B36-$B$4*C36-$B$5*(C36-((D36+C36*$B$5)/($B$5+$B$17)))-D36)*$E$6;C36+					
39	1,625E-07	0,14534287	1/$B$6*(B36-$B$4*C36-$B$5*(C36-((D36+C36*$B$5-$B$19)/($B$5+$B$18)))-D36)*$E$6))					
40	0,000000175	0,15643431			2,73E-03	0,00E+00		

Table 5: Conditional computation of current and voltage depending on phase, interpolated Shockley diode model.

	A	B	C	D	E	F	G	H
25	t	U0	i1	Uc	Ud	Id		
35	1,125E-07	0,10080814	7,7192E-05	3,04E-05	1,57E-03	0		
36	0,000000125	0,11196436	8,8126E-05	4,00E-05	1,80E-03	0		
37	1,375E-07	0,1231065	9,9056E-05	5,10E-05	=WENN(UND(E35>0;E36>0);C37*$B$5+D37;WENN(E36>=-0,			
38	0,00000015	0,13423313	0,00010998	6,34E-05	333;$B$17*F37;$B$18*F37+$B$19))			
39	1,625E-07	0,14534287	0,00012089	7,72E-05				

	A	B	C	D	E	F	G	H
25	t	U0	i1	Uc	Ud	Id		
35	1,125E-07	0,10080814	7,7192E-05	3,04E-05	1,57E-03	0		
36	0,000000125	0,11196436	8,8126E-05	4,00E-05	1,80E-03	0		
37	1,375E-07	0,1231065	9,9056E-05	5,10E-05	2,03E-03	=WENN(UND(E35>0;E36>0);0;WENN(		
38	0,00000015	0,13423313	0,00010998	6,34E-05	2,26E-03	E36>=-0,333;(D37+C37*$B$5)/($B$5+		
39	1,625E-07	0,14534287	0,00012089	7,72E-05	2,49E-03	$B$17);(D37+C37*$B$5-$B$19)/($B$5+		
40	0,000000175	0,15643431	0,00013178	9,23E-05	2,73E-03	$B$18)))		
41	1,875E-07	0,16750606	0,00014266	1,09E-04	2,96E-03			

Table 6: Conditional computation of diode current and diode voltage depending on interpolation formula.

2.3 EXCEL Implementation – interpolated Shockley diode

The top of the spreadsheet for the model with the interpolated Shockley Diode is almost equivalent to the top of the model with ideal diode (Table 2). Only a few parameters for the linear interpolation for the diode voltage – current relation are added.

Also the simulation of the interpolated Shockley diode model starts in locking phase – for 10 rows without conditions for phase change

In Table 5, cell C37 shows the Euler solver update for the conductor current i_{1_k}, with conditions for phase changes and interpolation selection.

The first distinction is for determining locking or conducting phase, the second one is programmed inside the conducting phase and decides about the linear interpolation function of diode voltage u_{D_k} and diode current i_{D_k} (shown in Table 6, cell E37 and cell F37).

From cell E36 to cell E37 the code changes from **`E36=C36*$B$5+D36`** to

```
E37=WENN(UND(E35>0;E36>0);C37*$B$5+D37;
    WENN(E36>=-0,333;$B$17*F37;
    $B$18*F37+$B$19))
```

2.4 EXCEL simulation interpolated Shockley diode model - results

The smoothening dynamics of the (interpolated) Shockley diode model should eliminate the jumping characteristics of the ideal diode model. The results for capacitor voltage u_C, diode voltage u_D and diode current i_D show the expected smoothed behaviour.

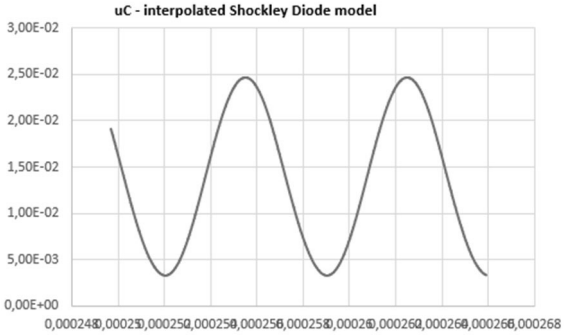

Figure 10: EXCEL simulation results for interpolated Shockley model – capacitor voltage.

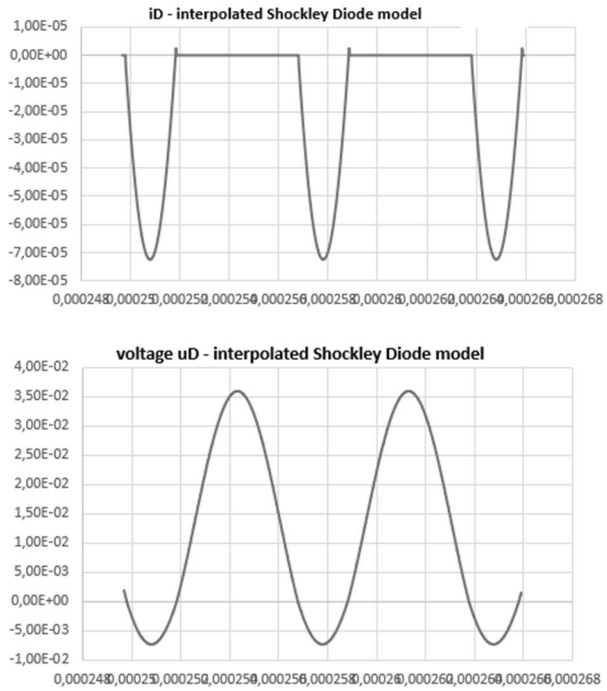

Figure 11: EXCEL simulation results for interpolated Shockley model – diode voltage and diode current.

Diode voltage u_D (Figure 11, below) shows now continuous behaviour, and diode current i_D shows almost no 'spikes', and the resulting capacitor voltage u_C looks now also continuous (Figure 10) – in comparison with results from ideal diode model (Figure 6).

2.5 Linearisation of Shockley formula

A classical approximation for the nonlinear Shockley formula is the linearisation of the exponential function, e.g. at linearisation point $u_{D_{lin}} = 0$,

$$e^{\frac{u_D}{U_T}} = \sum_0^\infty \left(\frac{u_D}{U_T}\right)^n \cdot \frac{1}{n!} = 1 + \frac{u_D}{U_T} + \left(\frac{u_D}{U_T}\right)^2 \cdot \frac{1}{2} + \left(\frac{u_D}{U_T}\right)^3 \cdot \frac{1}{6} + \cdots$$

so that i_D gets the linear approximation formula

$$i_D = I_S \cdot \left(e^{\frac{U_D}{U_T}} - 1\right) \sim I_s \cdot \left(1 + \frac{u_D}{U_T} - 1\right) = \frac{I_s}{U_T} \cdot u_D$$

$$i_D = \frac{I_s}{U_T} \cdot u_D = \frac{1}{k_{lin}} \cdot u_D$$

Now starting again with Kirchhoff's joint formula,

$$0 = -u_C - (i_1 - i_D) \cdot R_2 + u_D$$

we substitute i_D by the above linearised formulation

$$0 = -u_C - (i_1 - \frac{I_s}{U_T} \cdot u_D) \cdot R_2 + u_D$$

and get linear formulas for u_D and i_D:

$$u_D = U_T \cdot \frac{U_C + R_2 \cdot i_1}{I_s R_2 + U_T},\ i_D = I_s \cdot \frac{U_C + R_2 \cdot i_1}{I_s R_2 + U_T}$$

These relations are equivalent to the formula for the first region of the Shockley formula interpolation with $u_D = k_{low} \cdot i_d \sim k_{lin} \cdot i_d$:

$$i_D = \frac{1}{k_{lin}} \cdot\ u_D \ \rightarrow\ i_D = \frac{(u_C + i_1 \cdot R_2)}{(R_2 + k_{lin})}$$

Figure 12 shows the situation: instead of the linear function with slope k_{low} now the tangent with slope k_{lin} can be used – and interestingly, the simulations show almost the same results.

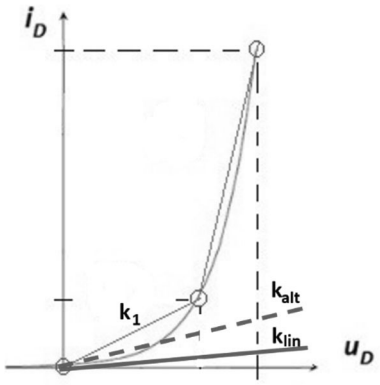

Figure 12: Shockley diode characteristics – interpolated, linearized and approximated around zero.

And interestingly, the indeed same results are produced with a slope k_{alt}, with $k_{lin} < k_{alt} < k_1$, as some experiments have shown. Reason is, that the current i_D is very low, so that approximation near to $u_D = 0$ is sufficient.

Generally, one could also use a linearisation around a proper linearisation point $u_{D_{lin}} \neq 0$:

$$e^{\frac{u_D}{U_T}} = \sum_0^\infty \left(\frac{(u_D - u_{D_{lin}})}{U_T}\right)^n \cdot \frac{1}{n!} \sim 1 + \frac{u_D - u_{D_{lin}}}{U_T}$$

so that u_D becomes

$$u_D = \frac{U_T \cdot (u_C - R_2 \cdot i_1) + R_2 \cdot I_s \cdot u_{D_{lin}}}{R_2 I_s + I_s}$$

There is a tricky algorithmic choice for the 'unknown' $u_{D_{lin}}$: if the formula is used in the course of the Euler solver, then $u_{D_{lin}}$ can be estimated with the previous value $u_{D_{n-1}}$ for the diode voltage:

$$u_{D_n} = \frac{U_T \cdot \left(u_{C_n} - R_2 \cdot i_{1_n}\right) + R_2 \cdot I_s \cdot u_{D_{n-1}}}{R_2 I_s + I_s}$$

3 RLC Model – Shockley Diode

The Schockley diode model constitutes an exponential link between diode current and applied voltage (Figure 7). The relation between current i_D and voltage u_D in a Shockley diode follows now a continuous function:

$$i(u_D) = \begin{cases} 0, u_D > 0 \\ I_S * (e^{\frac{u_D}{U_T}} - 1), u_D \le 0 \end{cases}$$

In the conducting phase, there is an exponential-shaped (nonlinear) relation between diode voltage and diode current, which cannot be resolved directly.

3.1 RLC Model with Shockley formula

RLC modelling for the conducting phase first yields

$$\frac{du_C}{dt} = \frac{1}{C} \cdot (i_1 - i_D)$$

$$\frac{di_1}{dt} = \frac{1}{L} * (U_0 - i_1 \cdot (R_1 + R_2) + i_D \cdot R_2 - U_C)$$

In both differential equations now i_D must be substitutes by the Shockley formula:

$$\frac{du_C}{dt} = \frac{1}{C} \cdot \left(i_1 - I_S \cdot \left(e^{\frac{U_D}{U_T}} - 1 \right) \right)$$

$$\frac{di_1}{dt} = \frac{1}{L} \cdot \left(U_0 - i_1 \cdot (R_1 + R_2) + I_S \cdot \left(e^{\frac{U_D}{U_T}} - 1 \right) \cdot R_2 - U_C \right)$$

Now also in Kirchhoff's junction formula

$$0 = -u_C - (i_1 - i_D) \cdot R_2 + u_D$$

i_D is substitutes by the Shockley formula:

$$u_D = u_c + \left(i_1 - I_S \cdot \left(e^{\frac{u_D}{U_T}} - 1 \right) \right) \cdot R_2$$

This nonlinear algebraic equation for u_D is added to the above differential equations for u_C and i_1, which would need u_D as further (algebraic) state variable. The result is a DAE system, a differential-algebraic system, which needs special solvers, combining ODE solving and nonlinear equation solving.

A proper alternative is now to derive a differential equation for the diode voltage u_D . Calculating the derivative of the algebraic equation for u_D results in

$$\dot{u}_D = \left(\dot{u}_C + \dot{i}_1 * R_2 \right) * \left(1 + \frac{I_S * \left(e^{\frac{u_D}{U_T}} \right) * R_2}{U_T} \right)^{-1}$$

Now the derivatives $\dot{u}_C$ and $\dot{i}_1$ are replaced by the differential equations:

$$\dot{u}_D = \left(i_1 - I_S * \left(e^{\frac{u_D}{U_T}} - 1 \right) \right) + \\ + R_2 \cdot \frac{1}{L} \cdot \left(U_0 - i_1 \cdot (R_1 + R_2) + I_S \cdot \left(e^{\frac{u_D}{U_T}} - 1 \right) \cdot R_2 - u_C \right) \cdot \\ \cdot \left(1 + \frac{I_S * \left(e^{\frac{U_D}{U_T}} \right) * R_2}{U_T} \right)^{-1}$$

Now the Euler solver is applied on these three differential equations, for state update, giving

$$i_{1_{n+1}} = i_{1_n} + \Delta t \cdot f(i_{1_n}, u_{C_n}, u_{D_n})$$

$$u_{C_{n+1}} = u_{C_n} + \Delta t \cdot g(i_{1_n}, u_{C_n}, u_{D_n})$$

$$u_{D_{n+1}} = u_{D_n} + \Delta t \cdot h(i_{1_n}, u_{C_n}, u_{D_n})$$

where the function *f*, *g* and *h* represent the right-hand side of the ODE formulas.

3.2 Phase change Locking - Conducting

In the simulation of the fully dynamic Shockley diode the state event recognition is again based on the diode voltage u_D. Finding the state event of locking phase start is facilitated because of negative voltage u_D in conducting phase. Another advantage is now that no further case distinction in conducting phase is needed for the computation of the diode voltage.

The state event condition function of the conducting phase is given by:

$$! - \\ U_D = i_1 * R_2 + U_C$$

whereby u_D is now solution of the differential equation for u_D in resolved form. completes the

3.3 EXCEL implementation – Shockley diode model

The top of the spreadsheet for the model with the interpolated Shockley Diode is almost equivalent to the top of the models before (Table 2). Only a few parameters for the characteristics of the Shockley equation are added, and an initial value for the ODE for the diode voltage.

Also the simulation of the dynamic Shockley diode model starts in locking phase – for 10 rows without conditions for phase change.

Additionally, now an Euler state update for u_{D_k} must be programmed. In Table 7, cell E37 shows the Euler solver update for the diode voltage u_{D_k}, with conditions for phase changes.

	A	B	C	D	E	F	G	H
25	t	U0	i1	Uc	Ud	Id		
32	0,000000075	0,06726894	4,45523E-05	9,61E-06	9,01E-04	0		
33	8,75E-08	0,07845902	5,53737E-05	1,52E-05	1,12E-03	0		
34	0,0000001	0,08963922	6,62679E-05	2,21E-05	1,35E-03	0		
35	1,125E-07	0,10080814	7,71924E-05	3,04E-05	1,57E-03	0		
36	0,000000125	0,11196436	8,81257E-05	4,00E-05	1,80E-03	0		
37	1,375E-07	0,1231065	9,90563E-05	5,10E-05	=WENN(UND(E35>0;E36>0);C37*$B$5+D37;E36+((			
38	0,00000015	0,13423313	0,000109978	6,34E-05	1/$B$7*(C37-$B$8*(EXP(E36/$B$9)-1))+$B$5*1/			
39	1,625E-07	0,14534287	0,000120887	7,72E-05	$B$6*(B37-C37*($B$4+$B$5)+$B$8*(EXP(E36/			
40	0,000000175	0,15643431	0,00013178	9,23E-05	$B$9)-1)*$B$5-D37))*(1+($B$8*EXP(E36/$B$9)*			
41	1,875E-07	0,16750606	0,000142656	1,09E-04	$B$5)/$B$9)^(-1))*$E$6)			
42	0,0000002	0,17855672	0,000153513	1,27E-04				

WENN(**Wahrheitstest**; [Wert_wenn_wahr]; [Wert_wenn_falsch])

Table 7: Conditional computation of diode voltage with Euler step update.

3.4 EXCEL simulation Shockley diode - results

The results for the dynamics Shockley diode model show generally the expected continuous behaviour (Figure 13), comparisons with results from ideal diode model and interpolated Shockley diode model see the next chapter.

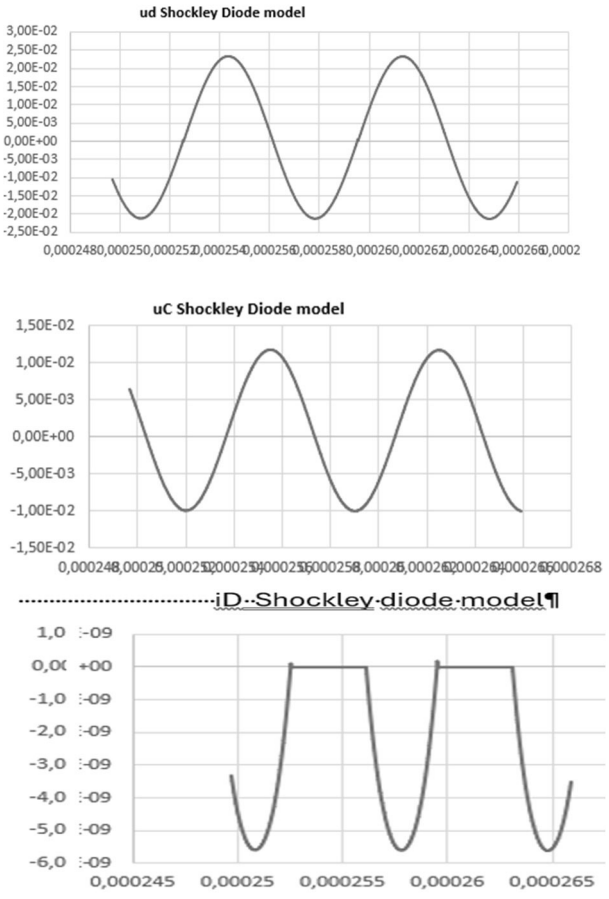

Figure 13: EXCEL simulation results for dynamic Shockley model.

4 Comparison of Results

A comparison of the results is to some extent difficult, as there were some problems with the numeri behaviour of the computation in EXCEL. So observed differences may also be caused by these numerical problems.

In the Figure 14 the diode current for the three different models are shown. The blue graph corresponds to the first case, the idealized diode. Its path through the locking phase is stable, as the diode voltage is at a relatively high level. As the conducting phase is entered, the current rises until its peak value is reached. In the second part of the conducting phase, the current decreases and reaches even positive values.

Per definition an ideal diode is conducting only if it is forward biased, so the computed peaks in positive direction are wrong. The reason therefore is the chosen case distinction which demands two positive values for U_D in a row for switching to the locking phase equation set. The simulation algorithm remains in the equation set for the conducting phase, although it should already have switched.

Analysing the graphs of the two other diode models (interpolated and fully dynamic Shockley diode), the above discussed artefacts do not appear. Case distinction works properly for switching between both phases, although the same conditions are applied. The reason therefore is, that there is a voltage drop along the diode also in conducting phase. This voltage drop is calculated with the diode current at timestep t_k. The voltage remains negative throughout the conducting phase and becomes positive with the current getting positive.

Due to this fact, two timesteps are calculated with the wrong set of equations before it is switched.

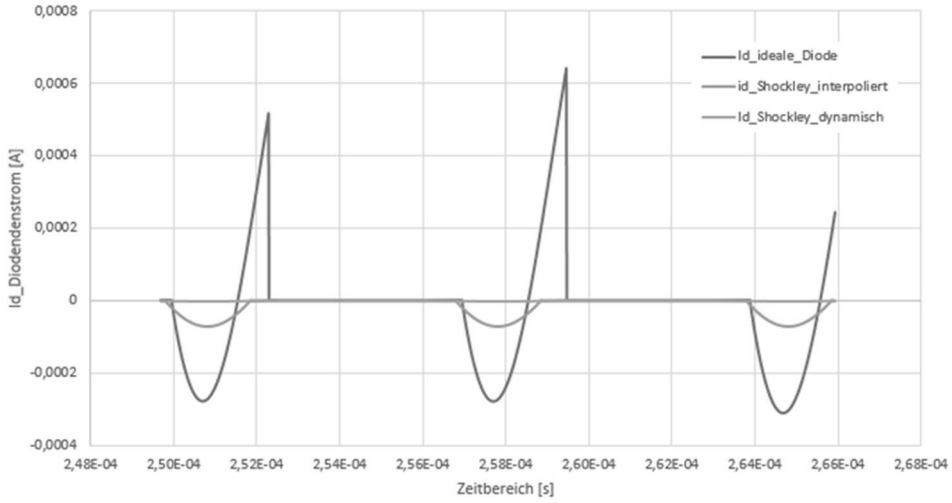

Figure 14: Comparison of simulation results for diode current – ideal diode, interpolated and dynamic Shockley diode.

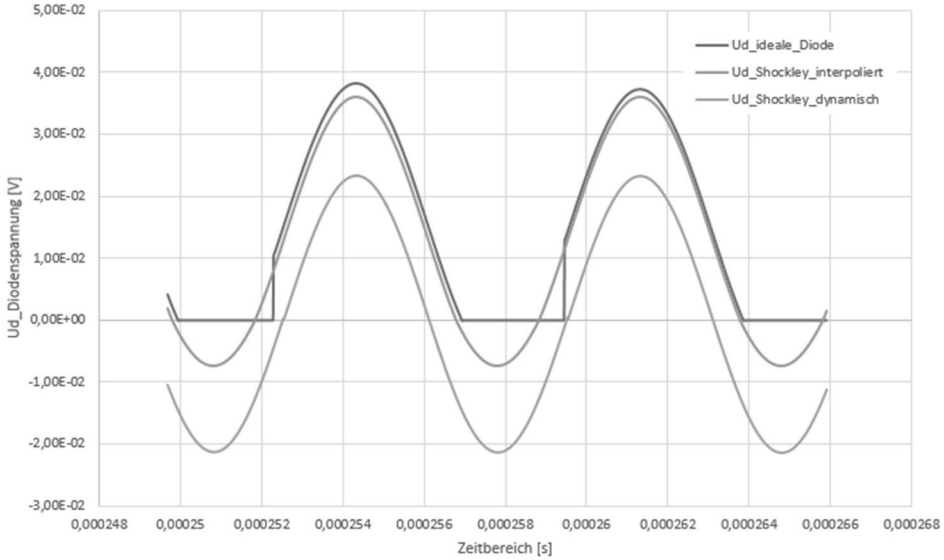

Figure 15: Comparison of simulation results for diode voltage – ideal diode, interpolated and dynamic Shockley diode.

In the ideal diode model at timestep t_k, the diode current is not needed for the computation of the diode voltage which causes the problems mentioned above.

In Figure 15 the diode voltage for the three different models is shown. In the graph, major differences between the three diode models can be observed. The blue line meets the definition of an ideal diode. No voltage drop appears in the conducting phase. Studying the orange graph corresponding to the interpolated Shockley diode, a negative voltage drop in conducting phase can be viewed. The fully dynamic Shockley model shows the same behaviour even more distinctive.

At a closer look on the diode voltage of the ideal model, the case switching problem mentioned above also is observable here. The switching from locking phase to conducting phase works properly, but not the following switch from conducting to locking phase. The equation for the locking phase delivers completely different values compared to the equation of the conducting phase in the timestep before. From one timestep to the following, the diode voltage increases by several orders of magnitude.

References

[1] Körner A, Breitenecker F. State Events and Structural-dynamic Systems: Definition of ARGESIM Benchmark C21. Simulation Notes Europe SNE 26(2), 2016, 117 – 122. DOI: 10.11128/sne.26.bn21.10339

EUROSIM Contact Information

EUROSIM – the **Federation of European Simulation Societies** was set up in 1989. The purpose of **EUROSIM** is to provide a European forum for simulation societies and groups to promote modelling and simulation in industry, research, and development – by publications and conferences.

EUROSIM members are national simulation societies and regional or international societies and groups dealing with modelling and simulation.

Full Members are ASIM, CEA-SMSG, CSSS, DBSS, KA-SIM, LIOPHANT, LSS, PTSK, NSSM, SIMS, SLOSIM, UKSIM. Observer Members are ALBSIM and ROMSIM. Former Members (societies in re-organisation) are: CROSSIM, FRANCOSIM, HSS, ISCS.

EUROSIM is governed by a Board consisting of one representative of each member society, president, past president, and **SNE** representative.

Each year a major **EUROSIM** event takes place, as the **EUROSIM CONGRESS** organised by a member society, **SIMS EUROSIM Conference**, and **MATHMOD Vienna Conference (ASIM)**.

At the **EUROSIM Congress 2023**, the 11th EUROSIM Congress in Amsterdam, July, 2023, a new **EUROSIM** president has been elected: Agostino Bruzzone. His society **LIOPHANT** will organize the next EUROSIM Congress in 2026 in Italy.

Furthermore, **EUROSIM Societies** organize local conferences, and **EUROSIM** co-operates with the organizers of **I3M Conference** and **WinterSim Conference Series.**

Contact Information

www.eurosim.info

President:
Agostino Bruzzone (LIOPHANT)
agostino@itim.unige.it

SNE – Simulation Notes Europe is EUROSIM's membership journal with peer-reviewed scientific contributions about all areas of modelling and simulation, including new trends as big data, cyber-physical systems, etc. The EUROSIM societies distribute **e-SNE** in full version to their members as official membership journal.

The basic version of **e-SNE** is available with open access (Creative Commons license CC BY). Publishers are **ASIM, ARGESIM** and **EUROSIM.**

www.sne-journal.org

SNE-Editor:
Felix Breitenecker (ASIM)
eic@sne-journal.org

EUROSIM Member Societies

ASIM - German Simulation Society
Arbeitsgemeinschaft Simulation

ASIM is the association for simulation in the German speaking area, servicing mainly Germany, Switzerland and Austria.

President
Felix Breitenecker, *felix.breitenecker@tuwien.ac.at*

Contact Information

www.asim-gi.org

info@asim-gi.org, admin@asim-gi.org

ASIM – Office Germany, Univ. Bundeswehr Munich, Inst. für Technische Informatik, Tobias Uhlig, Werner-Heisenberg Weg 39, 85577 Neubiberg, Germany

ASIM – Office Austria, dwh Simulation Services, F. Breitenecker, N. Popper, Neustiftgasse 57-59, 1070, Wien, Austria

CEA-SMSG – Spanish Modelling and Simulation Group

CEA is the Spanish Society on Automation and Control. The association is divided into national thematic groups, one of which is centered on Modeling, Simulation and Optimization (**CEA-SMSG**).

President
José L. Pitarch, *jlpitarch@isa.upv.es*

Contact Information

www.ceautomatica.es/grupos/

simulacion@cea-ifac.es

CSSS – Czech and Slovak Simulation Society

CSSS is the Simulation Society with members from the two countries: Czech Republic and Slovakia.

President
Michal Štepanovský
michal.stepanovsky@fit.cvut.cz

Contact Information

cssim.cz

michal.stepanovsky@fit.cvut.cz

CSSS – Český a Slovenský spolek pro simulaci systémů, Novotného lávka 200/5,
11000 Praha 1, Česká republika

DBSS – Dutch Benelux Simulation Society

DBSS was founded in July 1986 in order to create an organisation of simulation professionals within the Dutch language area.

President
M. Mujica Mota, *m.mujica.mota@hva.nl*

Contact Information

www.DutchBSS.org

a.w.heemink@its.tudelft.nl

DBSS / A. W. Heemink, Delft University of Technology,
ITS twi, Mekelweg 4, 2628 CD Delft, The Netherlands

KA-SIM Kosovo Simulation Society

The Kosova Association for Modeling and Simulation (**KA-SIM**) is closely connected to the University for Business and Technology (UBT) in Kosovo.

President
Edmond Hajrizi, *ehajrizi@ubt-uni.net*

Contact Information

www.ubt-uni.net

ehajrizi@ubt-uni.net

Dr. Edmond Hajrizi, Univ. for Business and Technology (UBT), Lagjja Kalabria p.n., 10000 Prishtina, Kosovo

LIOPHANT Simulation

is a non-profit association born in order to be a trait-d'union among simulation developers and users.

LIOPHANT is devoted to promote and diffuse the simulation techniques and methodologies; the Association promotes exchange of students, sabbatical years, organization of International Conferences, courses and internships focused on M&S applications.

President
A.G. Bruzzone, *agostino@itim.unige.it*

Contact Information

www.liophant.org

info@liophant.org

LIOPHANT Simulation, c/o Agostino G. Bruzzone,
DIME, University of Genoa, Savona Campus,
via Molinero 1, 17100 Savona (SV), Italy

LSS – Latvian Simulation Society

LSS has been founded in 1990 as the first professional simulation organisation in the field of Modelling and simulation in the post-Soviet area.

President
Artis Teilans, *Artis.Teilans@rta.lv*

Contact Information

www.itl.rtu.lv/imb/

Artis.Teilans@rta.lv, Egils.Ginters@rtu.lv

LSS, Dept. of Modelling and Simulation, Riga Technical University, Kalku street 1, Riga, LV-1658, Latvia

NSSM – National Society for Simulation Modelling (Russia)

NSSM (Национальное Общество Имитационного Моделирования – НОИМ) was officially registered in Russia in 2011.

President
R. M. Yusupov, *yusupov@iias.spb.su*

Contact Information

www.simulation.su

yusupov@iias.spb.su

NSSM / R. M. Yusupov, St. Petersburg Institute of Informatics and Automation RAS,
199178, St. Petersburg, Russia

PTSK – Polish Society for Computer Simulation

PTSK is a scientific, non-profit association of members from universities, research institutes and industry in Poland with common interests in variety of methods of computer simulations and its applications.

President
Tadeusz Nowicki,
Tadeusz.Nowicki@wat.edu.pl

Contact Information

www.ptsk.pl

leon@ibib.waw.pl

PSCS, ul. Gen. Witolda Urbanowicza 2, pok. 222,
00-908 Warszawa 49, Poland

SIMS – Scandinavian Simulation Society

SIMS is the Scandinavian Simulation Society with members from the five Nordic countries Denmark, Finland, Norway, Sweden and Iceland.

President
Tiina Komulainen,
tiina.komulainen@oslomet.no

Contact Information

www.scansims.org

vadime@wolfram.com

Vadim Engelson, Wolfram MathCore AB,Teknikringen 1E, 58330, Linköping, Sweden

SLOSIM – Slovenian Society for Simulation and Modelling

The Slovenian Society for Simulation and Modelling was established in 1994. It promotes modelling and simulation approaches to problem solving in industrial and in academic environments by establishing communication and cooperation among corresponding teams.

President
Goran Andonovski,
goran.andonovski@fe.uni-lj.si

Contact Information

www.slosim.si

slosim@fe.uni-lj.si, vito.logar@fe.uni-lj.si

SLOSIM, Fakulteta za elektrotehniko, Tržaška 25,
1000, Ljubljana, Slovenija

UKSIM - United Kingdom Simulation Society

The UK Modelling & Simulation Society (**UKSim**) is the national UK society for all aspects of modelling and simulation, including continuous, discrete event, software and hardware.

President
David Al-Dabass,
david.al-dabass@ntu.ac.uk

Contact Information

uksim.info

david.al-dabass@ntu.ac.uk

UKSIM / Prof. David Al-Dabass, Computing & Informatics,
Nottingham Trent University, Clifton lane,
Nottingham, NG11 8NS, United Kingdom

Observer Members

ROMSIM – Romanian Modelling and Simulation Society

Contact Information

florin_h2004@yahoo.com
ROMSIM / Florin Hartescu, National Institute for Research in Informatics, Averescu Av. 8 – 10,
011455 Bucharest, Romania

ALBSIM – Albanian Simulation Society

Contact Information

kozeta.sevrani@unitir.edu.al

Albanian Simulation Goup, attn. Kozeta Sevrani, University of Tirana, Faculty of Economy ,
rr. Elbasanit, Tirana 355, Albania

ASIM Books – ASIM Book Series – ASIM Buchreihen

Monographs

Simulation-based Optimization: Industrial Practice in Production and Logistics
Lothar März, Markus Rabe, Oliver Rose (Eds.); to appear; ASIM Mitteilung 191

Energy-related Material Flow Simulation in Production and Logistics.
S. Wenzel, M. Rabe, S. Strassburger, C. von Viebahn (Eds.); Springer Cham 2023, print ISBN 978-3-031-34217-2, eISBN 978-3-031-34218-9, DOI 10.1007/978-3-031-34218-9, ASIM Mitteilung 182

Kostensimulation - Grundlagen, Forschungsansätze, Anwendungsbeispiele
T. Claus, F. Herrmann, E. Teich; Springer Gabler, Wiesbaden, 2019; Print ISBN 978-3-658-25167-3; Online ISBN 978-3-658-25168-0; DOI 10.1007/978-3-658-25168-0; ASIM Mitteilung 169

Proceedings*

Tagungsband ASIM Workshop 2025 - GMMS/STS - ASIM Fachgruppenworkshop 2025, DLR Oberpfaffenhofen
W. Commerell, U. Durak, D. Zimmer (Hrgs.), ARGESIM Report 48; ASIM Mitteilung AM 193
ISBN ebook 978-3-903347-66-3, DOI 10.11128/arep.48, ARGESIM Verlag Wien, 2025

Tagungsband Kurzbeiträge ASIM SST 2024 -27. ASIM Symposium Simulationstechnik, Univ. Bundeswehr München,
München/Neubiberg, Sept. 2024, O. Rose, T. Uhlig (Hrgs.), ARGESIM Report 46; ASIM Mitteilung AM 189
ISBN ebook 978-3-903347-64-9, DOI 10.11128/arep.46, ARGESIM Verlag Wien, 2024

Tagungsband Langbeiträge ASIM SST 2024 -27. ASIM Symposium Simulationstechnik, Univ. Bundeswehr München
München/Neubiberg, Sept. 2024,O. Rose, T. Uhlig (Hrgs.), ARGESIM Report 47; ASIM Mitteilung AM 190
ISBN ebook 978-3-903347-65-6, DOI 10.11128/arep.47, ARGESIM Verlag Wien, 2024

Simulation in Production and Logistics 2023 – 20. ASIM Fachtagung Simulation in Produktion und Logistik
TU Ilmenau, September 2023; S. Bergmann, N. Feldkamp, R. Souren, S. Straßburger (Hrsg.);
ASIM Mitteilung 187; ISBN ebook 978-3-86360-276-5, DOI: 10.22032/dbt.57476, Universitätsverlag Ilmenau, 2023

Proceedings Langbeiträge ASIM Workshop 2023 - STS/GMMS/EDU - ASIM Fachgruppenworkshop 2023
Univ. Magdeburg, März 2023; C. Krull; W. Commerell, U. Durak, A. Körner, T. Pawletta (Hrsg.)
ARGESIM Report 21; ASIM Mitteilung 185; ISBN ebook 978-3-903347-61-8, DOI 10.11128/arep.21, ARGESIM Verlag, Wien, 2023

Kurzbeiträge & Abstract-Beiträge ASIM Workshop 2023 STS/GMMS/EDU - ASIM Fachgruppenworkshop 2023
Univ. Magdeburg, März 2023; C. Krull; W. Commerell, U. Durak, A. Körner, T. Pawletta (Hrsg.)
ARGESIM Report 22; ASIM Mitteilung 186; ISBN ebook 978-3-903347-62-5, DOI 10.11128/arep.22, ARGESIM Verlag, Wien, 2023

Proceedings Langbeiträge ASIM SST 2022 -26. ASIM Symposium Simulationstechnik, TU Wien, Juli 2022
F. Breitenecker, C. Deatcu, U. Durak, A. Körner, T. Pawletta (Hrsg.), ARGESIM Report 20; ASIM Mitteilung AM 180
ISBN ebook 978-3-901608-97-1, DOI 10.11128/arep.20, ARGESIM Verlag Wien, 2022

Proceedings Kurzbeiträge ASIM SST 2022 -26. ASIM Symposium Simulationstechnik, TU Wien, Juli 2022
F. Breitenecker, C. Deatcu, U. Durak, A. Körner, T. Pawletta (Hrsg.), ARGESIM Report 19; ASIM Mitteilung AM 179
ISBN ebook 978-3-901608-96-4, DOI 10.11128/arep.19, ISBN print 978-3-901608-73-5, ARGESIM Verlag Wien, 2022

Book Series Fortschrittsberichte Simulation – Advances in Simulation *

An Architecture for Model Behavior Generation for Multiple Simulators. H. Folkerts, FBS 42
ISBN ebook 978-3-903347-42-7, DOI 10.11128/fbs.32, ARGESIM Publ. Vienna,2024

Das Verhalten von Transuranelementen in Erdböden - Theorie, Beprobung und radiochemische Analysen. K. Breitenecker, FBS 41; ISBN ebook 978-3-903347-41-0, DOI 10.11128/fbs.41, 2024; ISBN print 978-3-901608-99-5, 2010/2024; ARGESIM Publ. Vienna

Aufgabenorientierte Multi-Robotersteuerungen auf Basis des SBC-Frameworks und DEVS. B. Freymann, FBS 40
ISBN ebook2020_978-3-903347-40-3, DOI 10.11128/fbs.40, ARGESIM Publ. Vienna, 2022

Cooperative and Multirate Simulation: Analysis, Classification and New Hierarchical Approaches. I. Hafner, FBS 39
ISBN ebook978-3-903347-39-7, DOI 10.11128/fbs.39, ARGESIM Publ. Vienna,2022

Die Bedeutung der Risikoanalyse für den Rechtsschutz bei automatisierten Verwaltungsstrafverfahren. T. Preiß, FBS 38
ISBN ebook 978-3-903347-38-0, DOI 10.11128/fbs.38, ARGESIM Publ. Vienna,2020

Methods for Hybrid Modeling and Simulation-Based Optimization in Energy-Aware Production Planning. B. Heinzl, FBS 37
ISBN ebook 978-3-903347-37-3, DOI 10.11128/fbs.37, ARGESIM Publ. Vienna,2020;

Konforme Abbildungen zur Simulation von Modellen mit verteilten Parametern. Martin Holzinger, FBS 36
ISBN ebook 978-3-903347-36-6, DOI 10.11128/fbs.36, ARGESIM Publ. Vienna, 2020

Fractional Diffusion by Random Walks on Hierarchical and Fractal Topological Structures. G. Schneckenreither, FBS 35
ISBN ebook 978-3-903347-35-9, DOI 10.11128/fbs.35, ARGESIM Publ. Vienna, 2024

A Framework Including Artificial Neural Networks in Modelling Hybrid Dynamical Systems. Stefanie Winkler, FBS 34
ISBN ebook 978-3-903347-34-2, DOI 10.11128/fbs.34, ARGESIM Publ. Vienna, 2020

Modelling Synthesis of Lattice Gas Cellular Automata and Random Walk and Application to Gluing of Bulk Material. C. Rößler, FBS 33
ISBN ebook 978-3-903347-33-5, DOI 10.11128/fbs.33, ARGESIM Publ. Vienna, 2021

Combined Models of Pulse Wave and ECG Analysis for Risk Prediction in End-stage Renal Desease Patients. S. Hagmair, FBS 32
ISBN ebook 978-3-903347-32-8, DOI 10.11128/fbs.32, ARGESIM Publ. Vienna, 2024

Mathematical Models for Pulse Wave Analysis Considering Ventriculo-arterial Coupling in Systolic Heart Failure. S. Parragh, FBS 31
ISBN ebook 978-3-903347-31-1, DOI 10.11128/fbs.31, ARGESIM Publ. Vienna, 2024

Variantenmanagement in der Modellbildung und Simulation unter Verwendung des SES/MB Frameworks. A. Schmidt, FBS 30; ISBN ebook 978-3-903347-30-4, DOI 10.11128/fbs.30, ARGESIM Verlag, Wien 2019

Classification of Microscopic Models with Respect to Aggregated System Behaviour. Martin Bicher, FBS 29
ISBN ebook 978-3-903347-29-8, DOI 10.11128/fbs.29, ARGESIM Publ. Vienna, 2020

*** Download** via ASIM **www.asim-gi.org** Open Access - Basic Version Member Access - Enhanced Version

Association Simulation News

ARGESIM is a non-profit association generally aiming for dissemination of information on system simulation – from research via development to applications of system simulation. **ARGESIM** is closely co-operating with **EUROSIM**, the Federation of European Simulation Societies, and with **ASIM**, the German Simulation Society.
ARGESIM is an 'outsourced' activity from the *Mathematical Modelling and Simulation Group* of TU Wien, there is also close co-operation with **TU Wien** (organisationally and personally).

→ **www.argesim.org**

→ *office@argesim.org*

→ ARGESIM/Math. Modelling & Simulation Group,
Inst. of Analysis and Scientific Computing, TU Wien
Wiedner Hauptstrasse 8-10, 1040 Vienna, Austria
Attn. Prof. Dr. Felix Breitenecker

ARGESIM is following its aims and scope by the following activities and projects:

- Publication of the scientific journal **SNE** – *Simulation Notes Europe* (membership journal of **EUROSIM**, the *Federation of European Simulation Societies*) – *www.sne-journal.org*
- Organisation and Publication of the **ARGESIM Benchmarks** for *Modelling Approaches and Simulation Implementations*
- Publication of the series **ARGESIM Reports** for monographs in system simulation, and proceedings of simulation conferences and workshops
- Publication of the special series **FBS Simulation** – Advances in Simulation / Fortschrittsberichte Simulation - monographs in co-operation with ASIM, the German Simulation Society
- Support of the Conference Series **MATHMOD Vienna** (triennial, in co-operation with **EUROSIM**, **ASIM**, and **TU Wien**) – www.mathmod.at
- Administration of **ASIM** (German Simulation Society) and administrative support for **EUROSIM** *www.eurosim.info*
- Simulation activities for TU Wien

ARGESIM is a registered non-profit association and a registered publisher: **ARGESIM Publisher Vienna**, root ISBN 978-3-901608-xx-y and 978-3-903347-xx-y, root DOI 10.11128/z…zz.zz. Publication is open for **ASIM** and for **EUROSIM Member Societies**.

SNE – Simulation Notes Europe

The scientific journal **SNE – Simulation Notes Europe** provides an international, high-quality forum for presentation of new ideas and approaches in simulation – from modelling to experiment analysis, from implementation to verification, from validation to identification, from numerics to visualisation – in context of the simulation process. **SNE** puts special emphasis on the overall view in simulation, and on comparative investigations.
Furthermore, **SNE** welcomes contributions on education in/for/with simulation.

SNE is also the forum for the **ARGESIM Benchmarks** on *Modelling Approaches and Simulation Implementations* publishing benchmarks definitions, solutions, reports and studies – including model sources via web.

SNE Editorial Office /ARGESIM

→**www.sne-journal.org**

office@sne-journal.org, eic@sne-journal.org

Felix Breitenecker EiC (Organisation, Authors)
Irmgard Husinsky (Web, Electronic Publishing))

ARGESIM/Math. Modelling & Simulation Group,
Inst. of Analysis and Scientific Computing, TU Wien
Wiedner Hauptstrasse 8-10, 1040 Vienna, Austria

SNE, primarily an electronic journal, follows an open access strategy, with free download in a basic version (B/W, low resolution graphics). This basic version is is licensed under CC BY 4.0 by ARGESIM Vienna -ASIM/ GI - EUROSIM

SNE is the official membership journal of **EUROSIM**, the *Federation of European Simulation Societies*. Members of (most) **EUROSIM Societies** are entitled to download the full version of e-**SNE** (colour, high-resolution graphics), and to access additional sources of benchmark publications, etc. (group login for the 'publication-active' societies; please contact your society).

Furthermore, **SNE** offers **EUROSIM Societies** a publication forum for post-conference publication of the society's international conferences, and the possibility to compile thematic or event-based **SNE Special Issues**.

Simulationists are invited to submit contributions of any type – *Technical Note*, *Short Note*, *Project Note*, *Educational Note*, *Benchmark Note*, etc. via **SNE**'s website:

→ **www.sne-journal.org**

Schlüsselrolle Simulation: Wandel gestalten.
Herausforderungen meistern.

ASIM Fachtagung

24. bis 26. Sept.

2025

„Haus der Kirche“

Dresden

21. ASIM Fachtagung „Simulation in Produktion und Logistik“

Als größte europäische Tagung zum Thema Simulation im Bereich Produktion und Logistik gibt die ASIM Fachtagung alle zwei Jahre einen Überblick der zukunftsweisenden Trends, aktuellen Entwicklungen und erfolgreichen Projekte. Präsentiert und diskutiert werden wissenschaftliche Arbeiten sowie interessante Anwendungen aus der Industrie.

Themen der Tagung

Supply Chain Simulation & Logistik
- Produktionsnetzwerke & -logistik
- Intralogistik; Lieferketten
- Transport & Verkehr
- Innovative Materialflusstechnik
- Produktionsplanung & -steuerung
- Systemresilienz, (Cyber-)Sicherheit

Simulationsanwendungen in Industrie und Dienstleistung
- Automobilindustrie
- Maschinen - & Anlagenbau
- Halbleiterindustrie
- Simulation as a Service
- Energieeffizienz, Nachhaltigkeit

Methoden
- Virtuelle Inbetriebnahme; Digitaler Schatten
- Simulationsbasierte Optimierung
- Verifikation & Validierung
- Data Science; Visual Analytics; Virtual Reality; Augmented Reality
- Künstliche Intelligenz; Maschinelles Lernen
- Ereignisdiskrete Simulation; Agentenbasierte Simulation
- Interoperabilität; verteilte Simulation; Cloud -basierte Simulation

Wir haben ein vielfältiges Programm erstellt. Besuchen Sie unsere Website für mehr Informationen.

Teilnahme

Ausstellung

Die begleitende Ausstellung zeigt den aktuellen Stand von Simulationswerkzeugen, verwandter Software und Dienstleistungen im Simulationsumfeld. Falls Sie sich als Aussteller auf der Fachtagung präsentieren möchten, kontaktieren Sie uns bitte.

Teilnahmegebühr (pro Person, inkl. Mehrwertsteuer)

Im Preis enthalten sind die Teilnahme an Vorträgen, der Ausstellung, Mittagessen, Erfrischungsgetränke mit Pausensnack, ein Get -Together sowie eine Abendveranstaltung. Ein gedruckter Tagungsband kann gegen einen Aufpreis von 50,00 € optional erworben werden.

Grundpreis		1190,00 €
Mitglieder von ASIM, GI, EUROSIM	abzgl.	140,00 €
Einreichung Beitrag (1 x pro Beitrag und Autor)	abzgl.	170,00 €
ab dem 2. Teilnehmer einer Institution	abzgl.	140,00 €

Hochschulangehörige erhalten 40 % Nachlass auf den Endpreis.

Tagungsleitung

Prof. Dr.-Ing. habil.
Thorsten Schmidt

Professur für
Technische Logistik
Fak. Maschinenwesen
TU Dresden

Tagungsort

„Haus der Kirche“
Hauptstraße 23
01097 Dresden

Anmeldung

Alle Informationen zur Anmeldung finden Sie auf unserer Website:

[https://asim -gi.org/spl2025]

ASIM Fachtagung

Institut für Technische Logistik und Arbeitssysteme

TECHNISCHE UNIVERSITÄT DRESDEN

www.sne-journal.org
www.argesim.org